

A Thesis for the Degree of Ph.D. in Engineering

Construction of Organ-scale Vascular Networks  
Using a Decellularized Liver  
by Regulating Mechanical and Chemical Factors

February 2020

Graduate School of Science and Technology

Keio University

Masafumi Watanabe

## **Thesis abstract**

There is a great deal of demand for construction of transplantable bioartificial liver grafts for patients with end-stage liver diseases due to a shortage of organ donors. Recent advances in tissue engineering enabled *in vitro* construction of whole-organ liver tissues using decellularized livers. However, it is still challenging to construct transplantable liver tissues, because these tissues are limited to short-term transplantation due to the lack of intact vascular networks. Therefore, the construction of functional vascular networks continuing from large vasculatures to microvessels is critical for development of transplantable liver tissues. Nevertheless, little is known about formation of microvessels in a decellularized liver. This thesis focuses on the construction of whole-organ vascular networks including microvessels by regulating mechanical and chemical factors.

Chapter 1 summarizes the background and objectives of this thesis.

Chapter 2 describes a construction of microvessels in a decellularized liver. Experiments were performed based on the hypothesis that fluid shear stress and surface coating with fibronectin can induce formation of hierarchical vascular networks including microvessels. The results demonstrated that a combination of perfusion culture and fibronectin coating significantly enhanced formation of microvessels, which were not observed in static culture. These results suggested that mechanical and chemical factors played important roles in the formation of *in vitro* microvessels.

Chapter 3 describes investigation of microvascular formation including anastomoses using a microfluidic chip because vascular anastomosis formation is an important step in construction of arterio-venous networks. It was found that coculture of human umbilical vein endothelial cells (HUVECs) and human mesenchymal stem cells (MSCs) effectively induced formation of microvascular networks including vascular anastomoses in a gel region. The results indicated that a HUVEC:MSC ratio, and corresponding gradient of biochemical factors were critical for the efficient formation of microvascular networks including anastomoses.

Chapter 4 describes construction of functional vascular networks by regulating mechanical and chemical factors using a decellularized liver and validates the antithrombotic function of the constructed vascular networks. This chapter indicated that improvement of endothelial cell coverage in a decellularized liver reduced platelet deposition. This result indicated that constructed vascular networks in a decellularized liver showed antithrombotic functions. The methods described in this study will provide useful insights for construction of transplantable livers.

Chapter 5 summarizes the results of this thesis and describes future prospects.

## 論文要旨

《和文題目》

脱細胞化肝臓を用いた機械的・化学的因子の調節による  
臓器スケール血管網の構築

ドナー肝臓の不足により、末期の肝疾患患者への移植を目的としたバイオ人工肝臓の構築が期待されている。近年の組織工学における発展では、臓器から細胞のみを除去する脱細胞化技術を利用することで生体外において肝臓全体の組織を構築することが可能になってきた。しかし、脱細胞化肝臓骨格を用いて構築した組織は、内部の血管網の構築が不完全であるため移植後の長期的な維持が困難であり、機能的な肝臓の構築は依然として実現されていない。したがって、大血管から毛細血管に至るまでの機能的な血管網を構築することは、移植可能な肝臓を構築する上で極めて重要である。脱細胞化肝臓内における毛細血管の構築手法は確立されていない。そこで本論文では、機械的・化学的因子を調節することにより、毛細血管を有する臓器スケールの血管網を構築することを目的とした。

第1章では、本論文の研究背景および目的について述べた。

第2章では、脱細胞化肝臓内における毛細血管の構築について記述した。本章では、生体外培養系の従来研究を参考にして、血流を模したせん断応力とフィブロネクチンによるコーティングが、毛細血管を有する階層的な血管網の形成を誘導すると仮説を立てて実験を行った。その結果、還流培養およびフィブロネクチンのコーティングの組み合わせが、毛細血管の形成を顕著に促進されることを見出した。このことから、機械的・化学的因子の調節によって脱細胞化肝臓内における毛細血管の形成が誘導されることが分かった。

第3章では、マイクロ流体チップを用いて毛細血管網の吻合条件を検討した。血管吻合を形成することは、動静脈網を構築する上で重要である。そこで、ヒト臍帯静脈血管内皮細胞とヒト間葉系幹細胞の共培養を行うことにより、生体外のゲル内部において血管吻合を有する毛細血管網の形成を誘導した。特に、異なる細胞の比率、および生化学的因子の濃度勾配が、血管吻合を有する血管網の形成を効率的に促進させることを示した。

第4章では、機械的・化学的因子の調節により、機能的な血管網の構築を図り、構築した血管網による抗血栓性の機能評価を行った。その結果、脱細胞化肝臓における血管内皮細胞の被覆率を向上させることにより、血小板の沈着が抑制されることが示された。以上の結果から、本研究で示した組織工学的手法が移植可能な肝臓の構築に向けて有用な知見を提供することができるものと期待される。

第5章では、本論文の研究結果を要約し、今後の展望について述べた。

## Contents

<b>Chapter 1 General introduction</b>	<b>1</b>
1-1 A major issue in organ transplantation	1
1-2 Function and anatomy of the liver	1
1-2-1 Liver function	1
1-2-2 Liver anatomy	4
1-3 Tissue engineering	8
1-4 Alternative approaches to liver transplantation	9
1-4-1 Hepatocyte transplantation	9
1-4-2 Cell sheet technology for liver cell transplantation	10
1-4-3 Fabrication of liver buds	11
1-5 Decellularization techniques	12
1-5-1 Various approaches for tissue decellularization	13
1-5-2 Whole-organ decellularization	15
1-5-3 Reconstruction of hepatic tissues using decellularized livers	16
1-6 Importance of vascularization in tissue engineering	19
1-6-1 Functions of <i>in vivo</i> endothelium	19
1-6-2 Functions of <i>in vitro</i> blood vessels	20
1-7 Microfabrication techniques	21
1-7-1 Microfluidic chip	21
1-7-2 <i>In vitro</i> vascular models in microfluidic chips	22
1-8 Regulatory factors of vascular morphology	23
1-8-1 Mechanical factor	23
1-8-2 Chemical factor	24
1-8-3 Regulation of <i>in vivo</i> vascular formation	25
1-9 Objectives	25

## Contents

<b>Chapter 2 Construction of microvessels in a decellularized liver</b>	<b>27</b>
2-1 Introduction	27
2-2 Experimental design	30
2-3 Materials and methods	32
2-3-1 Animal experiment and liver harvest	32
2-3-2 Decellularization of rat livers	32
2-3-3 Recellularization of rat livers	33
2-3-4 Perfusion culture of recellularized livers	36
2-3-5 Fibronectin coating of a decellularized liver	40
2-3-6 Immunofluorescence staining and imaging of livers	40
2-3-7 Evaluation of endothelial cell alignment in perfusion culture	40
2-3-8 Computational fluid dynamics analysis in a decellularized liver	41
2-3-9 Statistical analysis	43
2-4 Results	44
2-4-1 Whole-liver decellularization	44
2-4-2 Reendothelialization of decellularized liver scaffolds using GFP-HUVECs	46
2-4-3 Mechanical stress promoted formation of sinusoid-scale microvessels	48
2-4-4 Chemical modification enhanced the formation of microvessels	54
2-4-5 Alignment of GFP-HUVECs in perfusion culture	56
2-5 Discussion	60
2-5-1 Liver tissue engineering using decellularized livers	60
2-5-2 Disruption of extracellular microarchitectures in a decellularized liver	60
2-5-3 Recellularization of a decellularized liver	61
2-5-4 Mechanical stress induced formation of microvessels	61
2-5-5 Chemical factor promoted formation of microvessels	64
2-5-6 Limitations and forthcoming challenges	64
2-6 Summary	66
<b>Chapter 3 Investigation of microvascular formation using a microfluidic chip</b>	<b>68</b>
3-1 Introduction	68
3-2 Experimental design	71

## Contents

3-3 Materials and methods	73
3-3-1 Fabrication of microfluidic chips	73
3-3-2 Cell preparation and <i>in vitro</i> formation of vascular anastomoses	73
3-3-3 Immunofluorescent staining and imaging of vasculatures	78
3-3-4 Quantitative analysis of vascular networks	78
3-3-5 Diffusion simulation of VEGF in HUVEC-MSC coculture	79
3-3-6 Live-cell imaging of <i>in vitro</i> vascular anastomosis formation	79
3-3-7 Observation of the detailed structure of <i>in vitro</i> vascular anastomoses	79
3-3-8 Statistical analysis	80
3-4 Results	81
3-4-1 Vascular formation was inhibited in HUVEC-HUVEC monoculture	81
3-4-2 HUVEC-MSC coculture promoted formation of <i>in vitro</i> vascular anastomoses	86
3-4-3 Live-imaging of <i>in vitro</i> vascular anastomosis formation	91
3-4-4 Investigation of the detailed structure of <i>in vitro</i> vascular anastomosis	93
3-4-5 Pro-angiogenic effects of VEGF gradient in HUVEC-HUVEC monoculture	95
3-5 Discussion	97
3-5-1 Inhibition of vascular sprouting in HUVEC-HUVEC monoculture	97
3-5-2 Establishment of an <i>in vitro</i> vascular anastomosis model in HUVEC-MSC coculture	97
3-5-3 Comparison of <i>in vitro</i> and <i>in vivo</i> anastomosis formation	99
3-6 Summary	100
<b>Chapter 4 Construction of functional vascular networks in a decellularized liver</b>	<b>102</b>
4-1 Introduction	102
4-2 Experimental design	105
4-3 Materials and methods	107
4-3-1 Animal experiment and liver harvest	107
4-3-2 Decellularization of rat livers	107
4-3-3 Recellularization of rat livers	107
4-3-4 Fibronectin coating of a decellularized liver	108
4-3-5 <i>Ex vivo</i> blood perfusion	109
4-3-6 Statistical analysis	109

## Contents

4-4 Results	110
4-4-1 HUVEC-MSC coculture in a decellularized liver	110
4-4-2 Maintenance of EC networks in perfusion culture with fibronectin coating	114
4-4-3 <i>Ex vivo</i> blood perfusion test of a recellularized liver	117
4-4-4 Comparison of a cell seeding route in a decellularized liver	121
4-5 Discussion	126
4-5-1 HUVEC-MSC coculture in a decellularized liver	126
4-5-2 Antithrombotic functions of constructed EC networks	126
4-5-3 Maintenance of sinusoid-scale microvessels in a decellularized liver	128
4-5-4 Optimization of the cell seeding route for recellularization	128
4-6 Summary	130
<b>Chapter 5 Concluding remarks</b>	<b>131</b>
5-1 Summary and conclusions	131
5-2 Future prospects	136
<b>References</b>	<b>139</b>
<b>Achievements</b>	<b>153</b>
Publications	153
International conferences	153
Domestic conferences	155
Awards	155
<b>Acknowledgements</b>	<b>156</b>

## List of abbreviations

2D: two-dimensional

3D: three-dimensional

ABC: ATP-binding cassette

ATP: adenosine triphosphate

BD: bile duct

bFGF: basic fibroblast growth factor

BM: basement membrane

CFD: computational fluid dynamics

CV: central vein

CYP: cytochrome P450

DAPI: 4',6-diamidino-2-phenylindole

DMEM: Dulbecco's modified Eagle's medium

EC: endothelial cell

ECM: extracellular matrix

EGM-2: endothelial growth medium-2

EGTA: ethylene glycol tetraacetic acid

FBS: fetal bovine serum

FITC: fluorescein isothiocyanate

FSS: fluid shear stress

GFP: green fluorescent protein

HA: hepatic artery

HSC: hepatic stellate cell

HUVEC: human umbilical vein endothelial cell

HV: hepatic vein

iPSC: induced pluripotent stem cell

IVC: inferior vena cava

## Abbreviations

LB: liver bud  
LML: left median lobe  
LSEC: liver sinusoidal endothelial cell  
MARS: molecular adsorbent recirculation system  
MMP: matrix metalloproteinase  
MSC: mesenchymal stem cell  
NO: nitric oxide  
PBS: phosphate-buffered saline  
PDMS: polydimethylsiloxane  
PFA: paraformaldehyde  
PGI<sub>2</sub>: prostacyclin  
PHx: partial hepatectomy  
PV: portal vein  
RML: right median lobe  
S1P: sphingosine-1-phosphate  
SD: standard deviation  
SE: standard error  
SLC: solute carrier  
SMA: smooth muscle actin  
SMC: smooth muscle cell  
SRL: superior right lobe  
TGF- $\beta$ 1: transforming growth factor- $\beta$ 1  
VEGF: vascular endothelial growth factor

## **Chapter 1 General introduction**

### 1-1 A major issue in organ transplantation

Over 40,000 people pass away in the United States annually due to chronic liver diseases and cirrhosis (Xu *et al.*, 2018). However, orthotopic liver transplantation is the only fundamental treatment for patients with end-stage liver diseases, which cannot be replaced by any other therapeutic modalities or artificial devices. As a result, a lot of patients pass away globally while waiting for vital livers for the lack of sufficient number of gifted vital livers from donors (Japan OrganTransplant Network, 2019). To overcome this problem, alternative therapeutic strategies to liver transplantation are needed for patients with end-stage liver diseases.

### 1-2 Function and anatomy of the liver

The liver provides functions required to maintain homeostasis in the organism. To achieve this, the liver synthesizes numerous essential molecules of diverse sort: extracts and metabolizes a plethora of nutrients and xenobiotics brought into the body through alimentary tract; stores, exports, and/or excretes the metabolic products; and neutralizes numerous foreign antigens and microbes from the gut. These various functions take place in a structurally complex, multicellular tissue with a unique angioarchitecture.

#### 1-2-1 Liver function

The liver is the largest solid organ in the human body and performs more than 500 essential biochemical reactions, including detoxification, protein synthesis, and the production of digestive chemicals. The major functions of the liver are as follows:

##### 1) Bile production

The major function of bile acid is to sustain nutrition for the growing organism by

## Chapter 1 General introduction

solubilizing dietary lipids (Hofmann, 1988). Bile is a complex fluid containing water, bile acid, cholesterol, phospholipids, bilirubin, and electrolytes that flows through the biliary tract into the small intestine. Especially, bile acid is critical for digestion and absorption of fats and fat-soluble vitamins in the small intestine.

### 2) Glucose metabolism

The human liver possesses the remarkable ability to produce glucose that is released to the systemic circulation and used by other tissues or organ, particularly during periods of fasting. Hepatic glucose production derives from glycogen breakdown (glycogenolysis) and from *de novo* synthesis of glucose (gluconeogenesis) (Adeva-Andany *et al.*, 2016).

### 3) Drug metabolism

Metabolism is a biotransformation process, where endogenous and exogenous compounds are converted to more polar products to facilitate their elimination from the body (Almazroo *et al.*, 2017). The process of metabolism is divided into 3 phases. The most common phase I drug-metabolizing enzymes are represented by cytochrome P450 (CYP450) superfamily. CYP450s are the major group of enzymes that chemically modify drugs into their water-soluble products to facilitate the excretion by kidney and/or liver. During phase II drug metabolism, the drugs or metabolites from phase I pathways are enzymatically conjugated with a hydrophilic endogenous compound with the help of transferase enzymes. Phase III pathway is classified into 2 main superfamily: ATP-binding cassette (ABC) and solute carrier (SLC) transporters. ABC transporters are dependent on the ATP consumption to actively uptake or efflux the drug from one side of the cell membrane to another, whereas SLCs facilitate the passage of certain solutes (e.g., sugars and amino acids) across the membrane and actively transport other solutes against their electrochemical gradients by coupling the process with other solute or ion.

### 4) Alcohol metabolism

Alcohol metabolism occurs largely in the liver. The bulk of ethanol oxidation occurs in the liver via alcohol dehydrogenase, which is predominantly expressed in hepatocytes. The second major pathway for ethanol elimination is the microsomal ethanol oxidizing system catalyzed by CYP2E1. CYP2E1 activity pathway is elevated in chronic alcoholics and induction of this pathway contributes to the metabolic tolerance to ethanol observed in alcoholics (Lieber, 2000).

### 5) Liver regeneration

Liver regeneration is popularly associated with the legend of Prometheus in ancient Greece. The ancient Greeks recognized liver regeneration in the myth of Prometheus. Having stolen the secret of fire from the gods of Olympus, Prometheus was condemned to having a portion of his liver eaten daily by an eagle. His liver regenerated overnight, thus providing the eagle with eternal food and Prometheus with eternal torture. In modern times, the best experimental model for the study of liver regeneration is that introduced by Higgins and Anderson (Higgins and Anderson, 1931): partial hepatectomy (PHx) in which two-thirds of the liver of a rat is removed. The residual lobes enlarge to make up for the mass of the removed lobes, though the resected lobes never grow back. The whole process lasts 5 to 7 days (Michalopoulos and DeFrances, 1997). For example, in rodents, the first wave of hepatocyte proliferation after PHx produces clusters of 10–14 cells, without the formation of sinusoids and additional extracellular matrix (ECM). Penetration of these clusters by stellate and sinusoidal cells occurs 2–4 days later, and is associated with laminin deposition (Martinez-Hernandez and Amenda, 1995), but it is not clear whether there is formation of new lobules. In both rats and mice, regeneration is mostly completed by 10–14 days after PHx. Human livers also have a great proliferative capacity. After right lobe resection, the donor liver representing 45–50% of the original organ

grows to 70–79% at 1 month and 80–90% at 6 months after transplantation (Pomfret *et al.*, 2003; Haga *et al.*, 2008).

### 1-2-2 Liver anatomy

#### 1) Hepatic structure

The liver of adult humans weighs from 1,300 to 1,700 g, depending on sex and body size. It is a continuous sponge-like parenchymal mass penetrated by tunnels that contain interdigitating networks of afferent (supplying) and efferent (draining) vessels (Elias, 1949). Major features of liver structure are a functional tissue (parenchyma) composed of at least seven distinct types of cells (Fig. 1-1). Cells in the liver are categorized as parenchymal cells and non-parenchymal cells. The parenchymal cells occupy almost 60% of the total number and 80% of the total volume of the liver, while the non-parenchymal cells occupy almost 40% of the total number and 6.5% of the total volume of the liver. For example, hepatocytes are categorized as parenchymal cells, while cholangiocytes, liver sinusoidal endothelial cells (LSECs), Kupffer cells, lymphocytes, dendritic cells, and hepatic stellate cells (HSCs) are categorized as non-parenchymal cells. Especially, it is known that hepatocytes perform the majority of numerous liver functions and consume oxygen at a > 5–10 times higher rate than most of the other cells (Kmiec, 2001). These cells conjointly possess capacities to synthesize, metabolize and eliminate a wide range of complex molecules and to carry out immune functions, all arranged in a matrix that facilitates their corporative interactions.

## Hepatic lobule

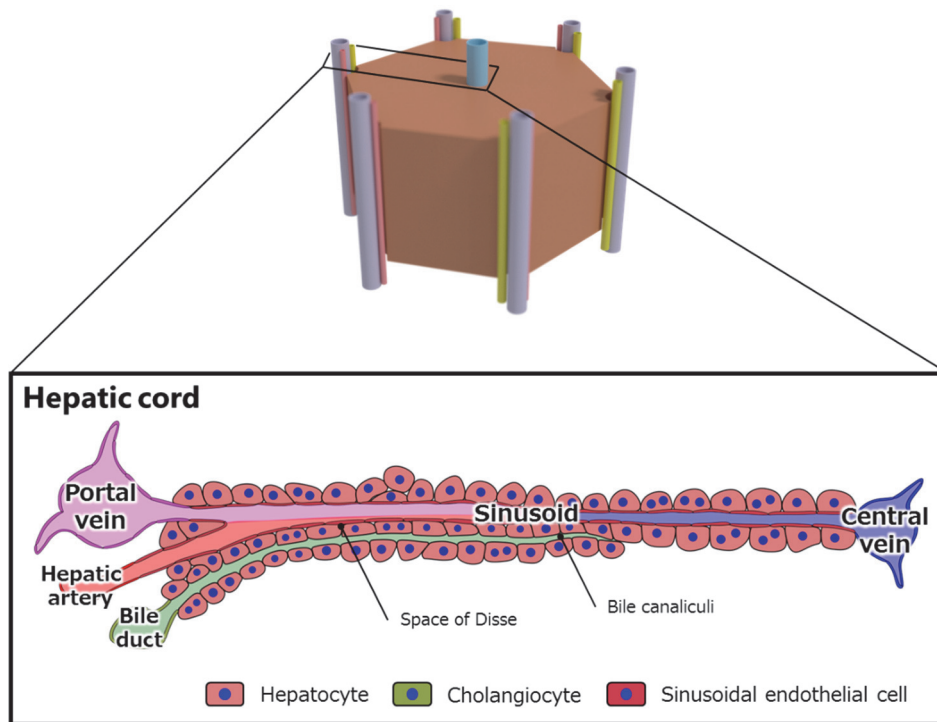


**Fig. 1-1** Schematic illustrations of a hepatic lobule. Blood enters into hepatic lobules via the hepatic artery (HA) and portal vein (PV), which then form hepatic sinusoids that drain into the central vein (CV) in the centrilobular region of the liver. Bile canaliculi are located between the two cords of hepatocytes on the contralateral side of the sinusoids, which drain into bile duct (BD). In the space of Disse, which is the space between hepatocytes and LSECs. Image modified from Gordillo *et al.* (2015).

### 2) Portal vein, hepatic artery, hepatic vein

The blood vessel and their investments of connective tissue provide the soft, spongy, liver with its major structural support. Larger afferent vessels such as PV, and HA are contained in connective tissues called “the portal tracts”, which are continuous with the mesenchymal components of the liver’s mesothelium-covered surface capsule (Glisson’s capsule). Portal tracts also contain BDs, lymphatic vessels, and nerves.

Vasculatures in the liver are mainly composed of three large blood vessels, HA, PV, and hepatic vein (HV) (Fig. 1-2). The HA carries blood at systemic levels of oxygen, pressure, and composition from the aorta to the liver, whereas the PV carries blood containing the digested nutrients from the entire gastrointestinal tract, and also from the spleen and pancreas to the liver. These blood vessels subdivide into smallest capillary-size vessels, which are known as “sinusoids”, then lead to a lobule. On the other hand, HV carries blood from the liver to the heart.

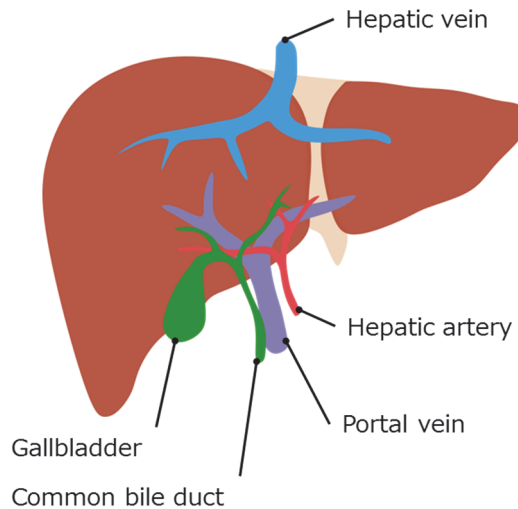


**Fig. 1-2 Schematic illustrations of hepatic vasculatures.** Hepatic vasculatures are composed of the PV, HA and HV. BD transports bile from liver to gallbladder.

### 3) Sinusoid

Sinusoids (approximately 10–20  $\mu\text{m}$  in diameter) are interposed between afferent terminal PVs and efferent HVs, which collect sinusoidal blood and merge to form larger HVs. Terminal PVs supply blood to sinusoids. LSECs form the wall of the liver sinusoids and represent approximately 15–20% of liver cells but only 3% of the total liver volume

(Maslak *et al.*, 2015). LSECs are highly specialized endothelial cells among mammalian endothelial cells (Poisson *et al.*, 2017). Normal endothelium of microcirculation can be categorized as continuous or discontinuous subtypes and, LSEC is categorized as both fenestrated and discontinuous subtypes, which has gaps within the cells and or between adjacent cells. Fenestrated endothelial cells (ECs) have pores that are either closed by a diaphragm or are fully open (Fig. 1-3). The LSEC cytoplasm, open fenestrae, and lack of an organized basement membranes (BMs) reduce the distance from sinusoid to the hepatocyte and thereby optimize oxygen deliver.

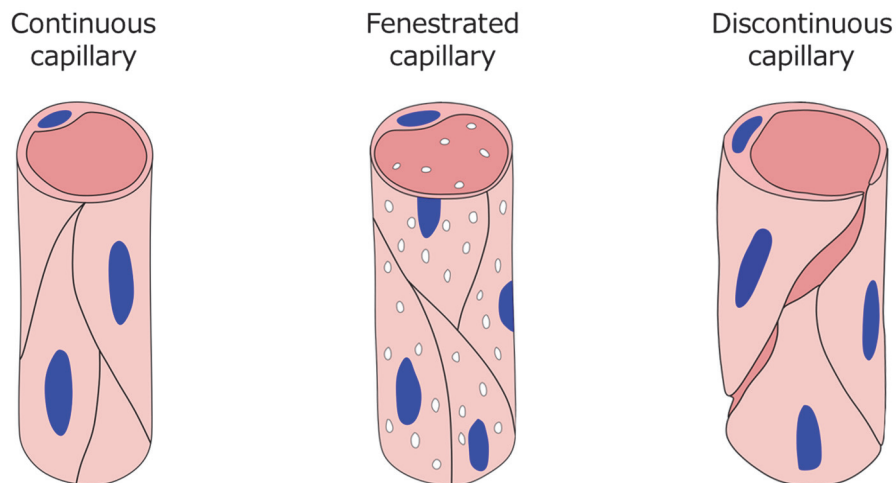


**Fig. 1-3 Schematic illustrations of continuous and discontinuous endothelium.** The endothelium is generally categorized as three subtypes such as continuous, fenestrated, and discontinuous.

#### 4) Bile duct

Intrahepatic BDs, a complex three-dimensional (3D) network of conduits within the liver, provide delivery of bile to the gall bladder and the intestine, which are composed

of biliary epithelial cells (i.e., cholangiocytes). Cholangiocytes represent approximately 3–5% of liver cells. Their major physiological function is ductal bile formation, which occurs via a series of secretory and adsorptive processes contributing to the final composition of bile (Boyer, 1996).

### 1-3 Tissue engineering

The concept of tissue engineering was defined approximately 25 years ago by Langer and Vacanti in 1993 as an interdisciplinary field of research that applies both the principles of engineering and the life sciences toward the development of biological substitutes that restore, maintain, or improve tissue function (Langer and Vacanti, 1993). Three general strategies have been adopted for the creation of new tissues (Fig. 1-4):

#### 1) Isolated cells or cell substitutes

This approach avoids the complications of surgery, allows replacement of only those cells that supply the needed function, and permits manipulation of cells before infusion. Its potential limitations include failure of the infused cells to maintain their function in the recipient, and immunological rejection.

#### 2) Tissue-including substances

The success of this approach depends on the purification and large-scale production of appropriate signal molecules, such as growth factors, and, in many cases, the development of methods to deliver these molecules to their targets.

#### 3) Cells placed on or within matrices

In closed systems, the cells are isolated from the body by a membrane that allows permeation of nutrients and wastes but prevents large entities such as antibodies or immune cells from destroying the transplant. These systems can be implanted or used as

an extracorporeal device.

Various strategies have been developed over past decades to fabricate tissue-engineered hepatic constructs *in vitro* (Damanian *et al.*, 2014). Although regenerated liver constructs had normal structures and hepatic functions to some extent, further refinement and optimization are necessary before real application in clinical settings.

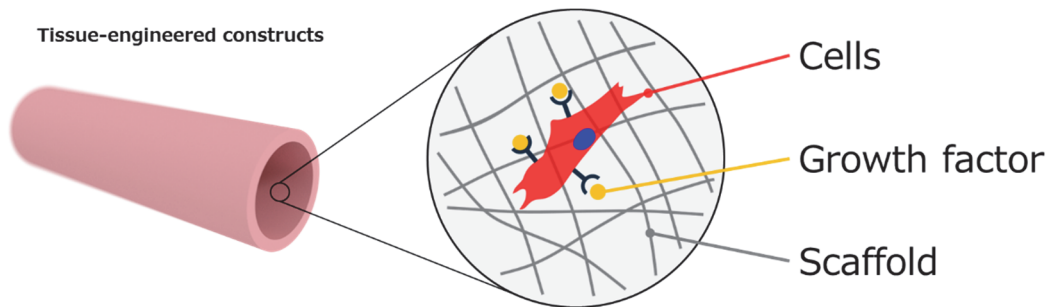


**Fig. 1-4 Three general strategies for tissue engineering.** Three main factors in tissue engineering: cells, growth factors, and scaffolds.

## 1-4 Alternative approaches to liver transplantation

### 1-4-1 Hepatocyte transplantation

A potential alternative to liver transplantation is hepatocyte transplantation, in which transplanted cells provide the impaired hepatic function once engrafted into recipient's liver. For example, it has been demonstrated that transplantation of hepatocytes isolated from human liver through PV of a recipient (Fig. 1-5), which results in the poor engraftment rate of hepatocytes (< 30%) (Fox *et al.*, 1998; Palakkan *et al.*, 2013). These results indicated that hepatocyte transplantation is not suitable for clinical use.

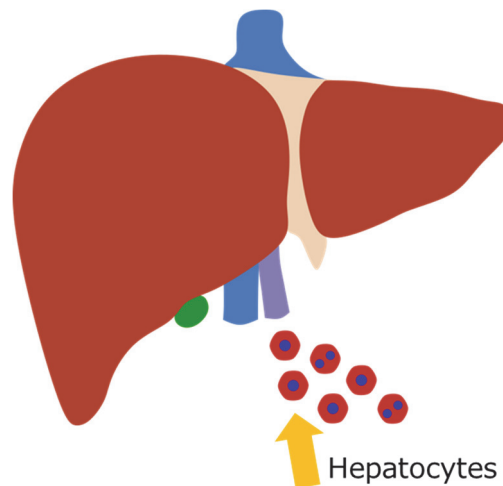


**Fig. 1-5 Schematic illustrations of hepatocyte transplantation.** Hepatocytes are infused through PV and engrafted in the liver.

#### 1-4-2 Cell sheet technology for liver cell transplantation

To construct functional liver tissue *in vitro*, Sakai *et al.* (2015) engineered cellular sheets consisting of human primary hepatocytes adhered onto a fibroblast layer (Fig. 1-6). The engineered hepatocyte/fibroblast sheets were transplanted to the subcutaneous space of mice and showed superior expression levels of vascularization-associated growth factors such as vascular endothelial growth factor (VEGF), transforming growth factor- $\beta$ 1 (TGF- $\beta$ 1), and hepatocyte growth factor *in vitro*. Moreover, this engineered cell sheet developed into vascularized subcutaneous human liver tissues contained glycogen stores, synthesized coagulation factor IX, and showed significantly higher synthesis rates of liver-specific proteins such as albumin and alpha 1 anti-trypsin *in vivo* than tissues from hepatocyte-only sheets after transplantation. Other groups also showed promising potential of cell sheet technology in regenerative medicine (Tatsumi and Okano, 2017). Although these approaches have potential for establishing novel cell therapies for liver diseases, the size of the reconstructed liver tissue was still limited due to the lack of adequate tissue oxygenation via blood vessels.

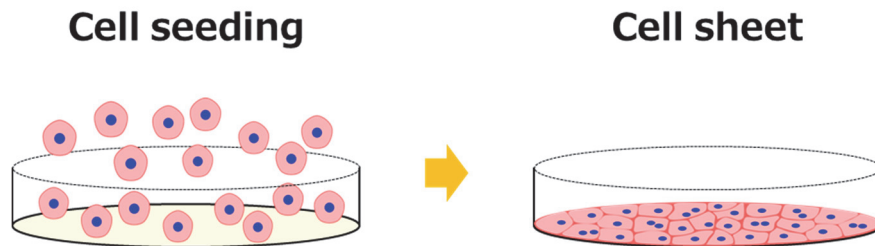


**Fig. 1-6 Schematic diagrams of hepatocyte sheets.** Hepatocytes were inoculated onto a cell culture dish coated with thermo-responsive polymers. After several days of culture, the dish was incubated at 20°C to induce the formation of a detached cell sheet.

#### 1-4-3 Fabrication of liver buds

Recently *in vitro* liver buds (LBs) has attracted a lot of attention in tissue engineering and regenerative medicine. Takebe *et al.* (2013) developed vascularized and functional human tissue-engineered liver constructs from human induced pluripotent stem cells (iPSCs) by transplantation of iPSC-LBs (Fig. 1-7). iPSC-derived hepatic cells self-organized into 3D iPSC-LBs by recapitulating organogenetic interactions between endothelial cells and mesenchymal cells. Immunostaining and gene-expression analyses revealed resemblance between *in vitro* iPSC-LBs and *in vivo* LBs. Moreover, human vasculatures in iPSC-LB transplants became functional by connecting to the host vessels within 48 hours.

In recent years, to overcome limitations of reproducibility and scalability, Takebe *et al.* (2017) effectively generated LBs in a highly reproducible manner using hepatic endoderm, endothelium, and septum mesenchyme. Furthermore, they achieved human scalability by developing an omni-well-array culture platform for mass producing homogeneous and miniaturized LBs on a clinically relevant large scale ( $> 10^8$  cells). Furthermore, Koike *et al.* (2019) developed an integral multi-organ structures

including hepatic, biliary and pancreatic structures by mimicking anteroposterior interactions *in vivo*. However, continued scaling efforts and appropriate cell scaffolds would be anticipated for clinical use and transplantation.

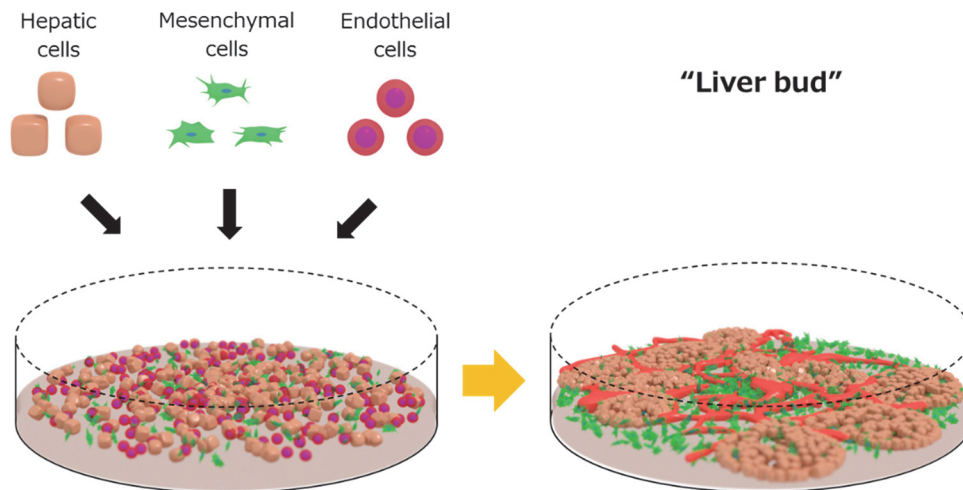


**Fig. 1-7 Schematic diagrams of generation of LBs.** iPSC derived hepatic cells, mesenchymal cells, and endothelial cells are seeded onto Matrigel and they form LBs resembling *in vivo* LBs.

### 1-5 Decellularization techniques

To achieve adequate size of tissue-engineered organ constructs *in vitro*, organ-scale platforms for cell engraftment is needed. One of the most promising techniques for tissue and organ engineering is decellularization of native tissues, in which ECM is isolated from its native tissues and genetic material in order to produce a natural scaffold. The ECM retains its inherent structural, biochemical, and biomechanical cues, which allows us to fabricate functional tissues or organs.

### 1-5-1 Various approaches for tissue decellularization

The ECM represents the secreted products of resident cells of each tissue and organ, is in a state of dynamic reciprocity with these cells in response to changes in microenvironment, and has been shown to provide cues that affect cell migration, proliferation, and differentiation (Zhou *et al.*, 2015). Preservation of the native ultrastructure and composition of ECM during the process of tissue decellularization is desirable for cell survival and engraftment. Clinical products such as surgical mesh materials composed of ECM are harvested from a variety of allogeneic or xenogeneic tissue sources, including dermis, urinary bladder, small intestine, mesothelium, pericardium, and heart valves have been used for clinical application. The term decellularization has not been defined by quantitative metrics. Based on the findings of studies in which an *in vivo* constructive remodeling response has been observed and adverse cell and host responses have been avoided, the following minimal criteria is needed to satisfy the intent of decellularization (Crapo *et al.*, 2011):

- 1) < 50 ng dsDNA per mg ECM dry weight.
- 2) < 200 bp DNA fragment length.
- 3) Lack of visible nuclear material in tissue sections stained with 4',6-diamidino-2-phenylindole (DAPI) or hematoxylin and eosin.

The most effective agents for decellularization depend on many factors, including the tissue's cellularity, density, lipid content, and thickness. In the decellularization process, 1A) chemical and 2) enzymatic, and 3) physical, or combinative approaches are commonly utilized to remove cells and DNA from the tissue while preserving its structural and regulatory proteins (Gilpin and Yang, 2017).

### 1) Chemical approach

Acids and bases cause or catalyze hydrolytic degradation of biomolecules. Peracetic acid is a common disinfection agent that doubles as a decellularization agent by removing residual nucleic acids with minimal effect on the ECM composition and structure (Hodde *et al.*, 2007; Gilbert *et al.*, 2008). Ionic, non-ionic, and zwitterionic detergents solubilize cell membranes and dissociate DNA from proteins, and they are therefore effective in removing cellular material from tissue (Cox and Emili, 2006). However, these agents also disrupt and dissociate proteins in the ECM. Especially, ionic detergents such as SDS are known to disrupt the native tissue structure, and result in reduced concentrations of GAG and loss of collagen integrity (Woods and Gratzner, 2005; Lin *et al.*, 2014).

### 2) Enzymatic approach

Enzymes reported in tissue decellularization protocols include nucleases, trypsin, collagenase, lipase, dispase, thermolysin, and  $\alpha$ -galactosidase. Enzymes can provide high specificity for removal of cell residues or undesirable ECM constituents. However, complete cell removal by enzymatic treatment alone has not been achieved and combination with detergent seems to be necessary for decellularization.

### 3) Physical approach

Freeze-thaw processing effectively lyses cells within tissues and organs, but the resulting membranous and intracellular contents remain unless removed by subsequent processing. A single freeze-thaw cycle can reduce adverse immune responses such as leukocyte infiltration in vascular ECM scaffolds (Lehr *et al.*, 2011). On the other hand, mechanical loads inducing a pressure gradient across tissue during decellularization can also be used to supplement enzyme treatment, which prevented the disruption of dermal ultrastructure (Prasertsung *et al.*, 2007). However, in previous studies, decellularized tissues were limited to relatively thin or avascular samples due to the diffusion limitation

of chemical reagents.

### 1-5-2 Whole-organ decellularization

To fabricate organ-scale complex decellularized tissues, perfusion has been employed as a technique for decellularization of organs while largely preserving the 3D architecture of the organ from which the ECM has been isolated. Vascular networks exist within organs that minimize the diffusion distance for oxygen in blood to cells. For this reason, perfusion through the vasculature is a particularly efficient method to deliver decellularizing agents to cells (Crapo *et al.*, 2011). As a result, recent advances in decellularization techniques allowed us to perform successful decellularization of complex organs such as the heart, lungs, and kidneys (Guyette *et al.*, 2014; Caralt *et al.*, 2015). Furthermore, Uygun *et al.* reported whole-liver decellularization in 2010 (Uygun *et al.*, 2010) (Fig. 1-8).

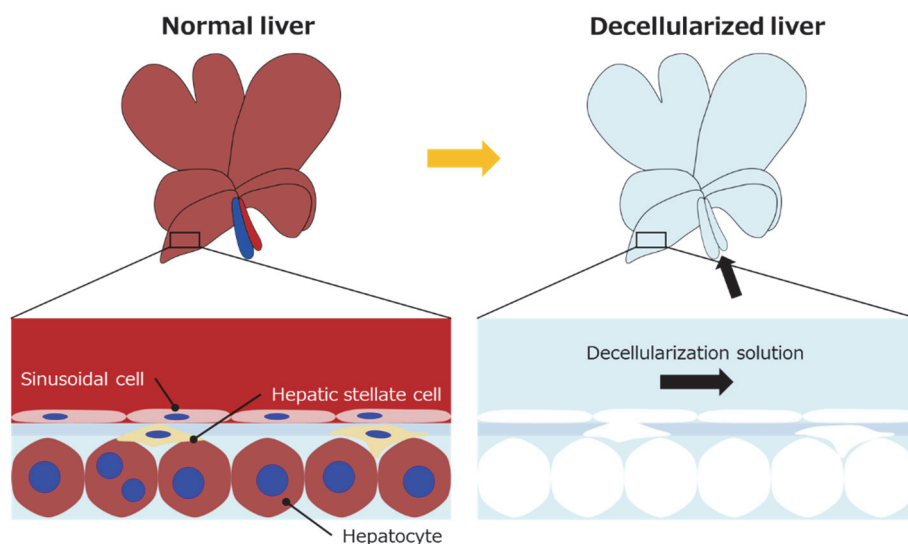


**Fig. 1-8 Schematic diagrams of liver decellularization.** Livers are perfused with decellularization solutions, which enables fabrication of acellular liver scaffolds.

### 1-5-3 Reconstruction of hepatic tissues using decellularized livers

Recently, some groups have performed reconstruction of a whole liver using decellularized liver matrices. For example, Uygun *et al.* (2010) demonstrated rat liver decellularization and the results showed that the decellularization process preserves the structural and functional characteristics of the native vascular networks, which allowed efficient recellularization of the liver matrix with mature hepatocytes. The recellularized graft supports liver-specific function *in vitro* including albumin secretion, urea synthesis and gene expression of CYPs at comparable levels to normal liver.

For example, Baptista *et al.* (2016) developed a perfusion bioreactor system and ferret decellularized livers seeded with HepG2 cells and MS1 endothelial cells were cultured in this reactor. In this system, MS1 cells were mostly localized at the vascular channels of the liver ECM scaffold, while HepG2 cells formed large cell clusters in the parenchyma, which indicated MS1 cells and HepG2 cells recapitulate hepatic structures. Moreover, Ji *et al.* (2012) reported that rat decellularized livers stimulated mesenchymal stem cells (MSCs) to express endodermal and hepatocyte-specific genes and proteins associated with improved hepatic functions, and the cells exhibited the ultrastructural characteristics of mature hepatocytes. Kadota *et al.* (2014) demonstrated enhanced hepatic function was achieved by co-cultivating bone marrow-derived MSCs with primary hepatocytes in decellularized livers. In addition, Soto-Gutierrez *et al.* (2011) demonstrated that decellularized livers reseeded with the multistep infusion of hepatocytes generated 90% of cell engraftment and supported liver-specific function including albumin production, urea synthesis, and CYP induction. According to these results, decellularized livers can recapitulate hepatic structures and functions *in vitro*.

Furthermore, decellularization technology was applied to a large animal model for human-scale whole-organ bioengineering, while liver decellularization was limited to small animal models such as rats, mice, and ferrets in previous studies. In recent years, Yagi *et al.* notably performed whole-organ decellularization using pig livers and

constructed hepatic tissues (Yagi *et al.*, 2013; Shimoda *et al.*, 2019).

Although recent advances enabled organ-scale bioengineering, there remain fundamental problems in terms of hemocompatibility. For example, long term maintenance of reconstructed liver tissues in animals is challenging due to clot formation inside these tissues (Meng *et al.*, 2019). Recent studies proposed several approaches to address this problem of clot formation in decellularized livers. Bruinsma *et al.* (2015) performed deposition of heparin, which is widely used as an anticoagulant, in decellularized liver scaffolds and the results demonstrated reduced thrombus formation in comparison to recellularized unmodified scaffolds. Furthermore, other groups performed reendothelialization of decellularized livers, which successfully resulted in reduced platelet adhesion and clot formation in the presence of ECs compared to unmodified decellularized livers (Ko *et al.*, 2015; Hussein *et al.*, 2016; Kojima *et al.*, 2018) (Fig. 1-9). However, complete prevention of clot formation has not been achieved and there is still room for improvements and fabrication of transplantable livers has not been achieved.

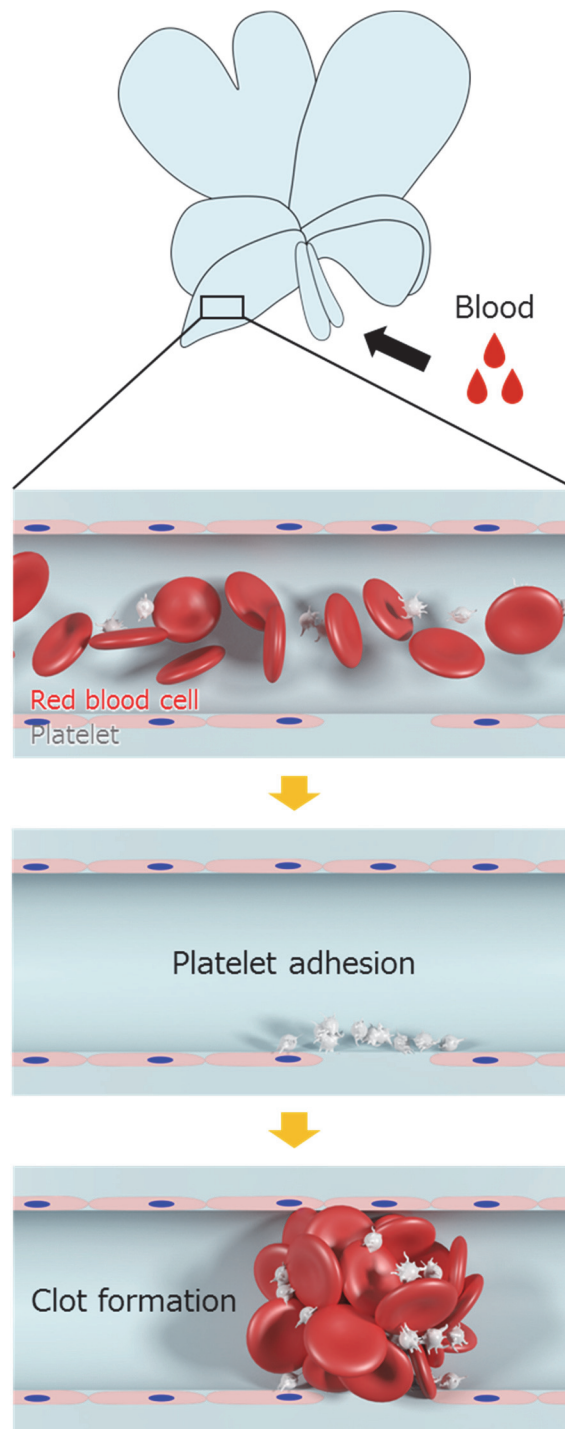


**Fig. 1-9 Schematic illustrations of clot formation in a decellularized liver.** After blood perfusion, platelets adhere to bare surface of a decellularized liver, which results in clot formation in vasculatures of the decellularized liver.

### 1-6 Importance of vascularization in tissue engineering

As mentioned in the previous section, endothelialization of tissue-engineered constructs including decellularized livers is essential to fabricate functional organs. *In vivo* endothelium of blood vessels is composed of ECs and they have various functions.

#### 1-6-1 Functions of *in vivo* endothelium

Endothelium is known to respond to physical and chemical signals by production of a wide range of factors that regulate 1) barrier function, 2) vascular tone, and 3) antithrombogenicity (Deanfield *et al.*, 2007; Rodrigues and Granger, 2015).

##### 1) Barrier function

The barrier properties of ECs are critical for the maintenance of water and protein balance between the intravascular and extravascular compartments. This barrier is formed by a layer of ECs that are joined laterally by cell–cell junctions, while the basolateral aspect of this layer is attached to a BM composed of collagen, fibronectin, laminin, and glycosaminoglycans (Rodrigues and Granger, 2015; Han *et al.*, 2015).

##### 2) Vascular tonus

Vasomotion plays a direct role in the balance of tissue oxygen supply and metabolic demand by regulation of vascular tone and diameter and is also involved in the remodeling of vascular structure (Deanfield *et al.*, 2007). This is achieved by production and release of several vasoactive molecules such as nitric oxide (NO), endothelium-derived hyperpolarizing factor, prostacyclin (PGI<sub>2</sub>), C-type natriuretic peptide, and endothelin 1 that relax or constrict the vessel. These molecules diffuse to the vascular smooth muscle cells (SMC) and activates guanylate cyclase, which leads to cyclic guanosine monophosphate (cGMP)-mediated vasodilatation or vasoconstriction.

### 3) Antithrombotic function

The surface of healthy endothelium is both anticoagulant and antithrombotic. ECs secrete a variety of molecules important for the regulation of blood coagulation and platelet functions. The major antiplatelet agents secreted by ECs are NO and PGI<sub>2</sub> and both of them synergistically increase cAMP content in platelets, which resulted in preventing platelet aggregation (Cines *et al.*, 1998). In the quiescent state, ECs maintain blood fluidity by promoting the activity of numerous anticoagulant pathways. Complex formation between thrombin and thrombomodulin also prevents thrombin from being able to clot fibrinogen or to activate platelets (Esmon, 1995). Moreover, the EC surface is rich in heparin-like GAGs, providing the main site for inactivation of active thrombin by providing a rich source of antithrombin, which is bound to these GAGs.

### 1-6-2 Functions of *in vitro* blood vessels

#### 1) Barrier function

Several groups have developed microfluidic models of vascular networks and their barrier function was assessed in previous reports. For example, Kim *et al.* (2013) constructed microvessels in a microfluidic chip and exhibited clear retention of polystyrene beads (7 µm in diameter) or fluorescein isothiocyanate (FITC)-dextran (70 kDa) inside the vessels without leakage into extravascular space. Moreover, Uwamori *et al.* (2019) assessed the barrier function of engineered microvascular networks using fluorescence dextran in a microfluidic chip, which indicated the permeability coefficient of engineered microvessels was comparable to that of *in vivo* microvessels.

#### 2) Vascular tonus

To the best of my knowledge, an *in vitro* model of blood vessels that can regulate vascular tonus such as vasoconstriction and vasodilation has not been published.

### 3) Antithrombotic function

Mannino *et al.* (2015) developed an *in vitro* vasculature model using PDMS microchannels and demonstrated that healthy ECs expressed antithrombotic functions, while platelets aggregated in a “bare” non-endothelialized microchannel. Moreover, Jain *et al.* (2016) and Barrile *et al.* (2018) developed microfluidic chip models with human endothelium perfused with human whole blood. These models enabled to evaluate key parameters in thrombosis, such as endothelial activation, platelet adhesion, platelet aggregation, and fibrin clot formation. The results demonstrated that human endothelium treated with inflammatory cytokines such as tumor necrosis factor- $\alpha$  led to the formation of larger aggregates of platelets. These results suggested that healthy vessels in tissue-engineered constructs can restore antithrombotic functions and reduce the risk of thrombosis.

### 1-7 Microfabrication techniques

Cellular morphogenesis such as vascular formation and EC migration is regulated by complex interactions that occurs in response to external factors. However, previous *in vitro* platforms such as a cell culture flask and Boyden chamber limited cellular migration in a two-dimensional (2D) plane (Even-Ram and Yamada, 2005). As mentioned in section 1-6-2, recent advances in microfabrication allowed us to manipulate cells in microenvironment mimicking *in vivo* (Rouwkema and Khademhosseini, 2016). Notably, Chung *et al.* (2009) developed a new microfluidic platform that has the capability to control the biochemical and biomechanical forces within a 3D scaffold coupled with accessible image acquisition, which is commonly referred as “microfluidic chip”.

#### 1-7-1 Microfluidic chip

Microfluidic chips are powerful tools for an integration of biophysical and biochemical factors, essential in mimicking physiological conditions. This platform

enabled time-dependent manipulation of flow and concentration gradients as well as real-time imaging for observing spatial-temporal single-cell behavior, cell–cell communication, cell–matrix interactions and cell population dynamics (Shin *et al.*, 2012). For example, Sudo *et al.* (2009) established conditions for 3D cultures of hepatocytes in a microfluidic chip and successfully constructed 3D hepatic tissue-like structures. Furthermore, they created a coculture model of hepatocytes and ECs, which resulted in formation of a 3D hepatic tissue and capillary-like structures in a microfluidic chip. In the future, “organ on a chip” with integrating multi-organ functions using this platform would be proposed, which may replace animal models in drug discovery and development.

### 1-7-2 *In vitro* vascular models in microfluidic chips

A microfluidic platform has been widely used for *in vitro* vascular models with vascular functions such as barrier function and thrombogenicity (Wang *et al.*, 2018). For example, Jeon *et al.* (2014) investigated effects of biochemical factors on vascular networks with small vessel diameters in a microfluidic chip, which demonstrated that the addition of TGF- $\beta$ 1 generated a non-interconnected microvasculature while angiopoietin-1 promoted functional network formation. On the other hand, Hsu *et al.* (2013) and Wang *et al.* (2016) investigated effects of biophysical factors on vascular networks such as shear stress and interstitial flow. They established an intact and perfusable microvascular system with capillary networks tightly interconnected without appreciable leakage that can control shear and interstitial flow, respectively. Moreover, they also established an *in vitro* pathological model such as a vascularized tumor platform to study tumor–vasculature interactions, tumor metabolism, and response of tumor cells and vasculatures to anti-cancer drugs (Sobrino *et al.*, 2016). In other groups, Yeon *et al.* (2012) and Kim *et al.* (2013) constructed perfusable and functional vascular networks in a microfluidic device. Moreover, they performed the perfusion of 40 or 70 kDa FITC dextran through

vascular networks, which showed clear retention of fluorescent dextran in vasculatures. More recently, Yamamoto *et al.* (2019, 2013) constructed stable capillary networks covered by pericyte-like perivascular cells, which maintained the lumen of small diameter, for at least 21 days using HUVECs and MSCs in a microfluidic chip. Immunofluorescence images of the constructed microvessels confirmed that the BM proteins such as laminin and collagen type IV deposited around microvessels covered by MSC-derived pericytes, which was in good agreement with *in vivo* capillary structures.

These studies indicated that *in vitro* vascular networks constructed in microfluidic chips recapitulated in terms of vascular morphologies and some functions. This platform will provide valuable insights to regulate vascular morphology *in vitro*.

### 1-8 Regulatory factors of vascular morphology

Morphology of vascular networks is known to be regulated by mechanical factors such as fluid shear stress (FSS), substrate stiffness, and topography (Yamamura *et al.*, 2007; Bernabeu *et al.*, 2014; Bogorad *et al.*, 2015; Baeyens *et al.*, 2015; Gray and Stroka, 2017), and biochemical molecules such as chemical gradients of angiogenic factors (Gerhardt, 2008; Shamloo *et al.*, 2012; van Duinen *et al.*, 2019).

#### 1-8-1 Mechanical factor

It has been suggested that vascular morphology is associated with blood flow, because growing evidence has been reported in previous studies (Herity *et al.*, 1999; Sigovan *et al.*, 2013; Korshunov *et al.*, 2007; Davis *et al.*, 2015). For example, Ueda *et al.* (2006, 2004) demonstrated that FSS promoted formation of microvascular networks in a parallel-plate flow chamber. Moreover, Galie *et al.* (2014) demonstrated that FSS exerted by both transmural and luminal fluid flow induced vascular sprouting in a microfluidic chip. In this model, fluid flow of  $> 10 \text{ dyn/cm}^2$  triggered ECs to sprout and invade into the underlying matrix. Interstitial flow is also shown to regulate formation of

vascular networks (Hsu *et al.*, 2013; Abe *et al.*, 2019).

Stiffness of ECM is also one of the most important factors to regulate vascular morphology. Yamamura *et al.* (2007) investigated the effect of substrate mechanical properties on the formation of microvascular networks, which revealed that ECs formed dense and thin networks in flexible gel, whereas thicker and deeper networks were formed in the rigid gel.

### 1-8-2 Chemical factor

Chemical factors also regulate vascular morphology in both physiological and pathological conditions (Gerhardt, 2008). Among them, VEGF stimulation especially promotes the division, survival, and migration of ECs, and is necessary for the formation of blood vessels (Hasso and Chan, 2011). Shamloo *et al.* (2012) utilized a microfluidic platform to study the EC behaviors induced by VEGF gradients during sprouting. In this study, time-lapse analysis of endothelial sprouting demonstrated that the ability of VEGF to regulate sprout orientation during vascular sprouting. Moreover, angiogenic effects of biochemical gradients on vascular formation were investigated in microfluidic chips. Song and Munn (2011) showed that VEGF gradient induced initiation of vascular sprouting. van Duinen *et al.* (2019) demonstrated that biochemical gradients by the combination of VEGF, phorbol myristate acetate, and sphingosine-1-phosphate (S1P) significantly promoted vascular sprouting and formation. In addition, ECM proteins also play important roles in vascular morphology and barrier behavior such as angiogenesis. Nicosia *et al.* (1993) demonstrated that elongation of microvessels was induced by fibronectin treatment in an aortic explant model. On the other hand, Han *et al.* (2015) found demonstrated that a synthetic ECM coating mimicking native BM matrix remarkably enhanced barrier function of EC monolayer.

### 1-8-3 Regulation of *in vivo* vascular formation

Vasculogenesis and angiogenesis are also known to be regulated by complex interactions *in vivo*. Ghaffari *et al.* (2015) developed a technique to simultaneously analyze flow dynamics and vascular remodeling by time-lapse microscopy in the capillary plexus of avian embryos. The results showed that vascular sprouts form from a vessel at lower pressure towards a vessel at higher pressure *in vivo*. *In vivo* vascular formation is also coordinated by anastomosis formation during embryo development. Herwig *et al.* (2011) and Lenard *et al.* (2013) described that multistep process is involved in vascular anastomosis, including EC migration, vascular contact, and luminal formation during development of zebrafish embryo. However, this process is still incompletely understood.

### 1-9 Objectives

The purpose of this study is to construct whole-organ vascular networks *in vitro* for the development of a transplantable liver. This can provide useful information to overcome current problems of organ donor shortage. In the past few decades, a lot of *in vitro* functional liver tissue grafts have been developed using biomaterials including cells, scaffolds, and growth factors. However, these tissue grafts are not suitable for clinical use as alternative to conventional liver transplantation due to insufficient tissue size.

Recent advances in tissue engineering allowed us to construct organ-scale tissues using a decellularized organ. Organ decellularization is a technique of removing all the cellular components from an organ while retaining the native composition and structure of the organ including acellular vascular networks. Moreover, in recent years, whole-liver decellularization has been established, which is a promising approach to produce organ-scale liver tissues. Previous studies demonstrated that decellularized livers filled with hepatocytes through the hepatic vasculature improved liver functions, such as albumin synthesis, urea secretion, and CYP expression at comparable levels to normal liver *in*

## Chapter 1 General introduction

*vitro*. However, it is still challenging to construct transplantable whole-organ liver tissues due the lack of intact vascular networks, which resulted in clot formation in a decellularized liver and subsequently impaired liver function.

To achieve transplantable liver tissues, several groups focused on endothelialization of a decellularized liver, because normal endothelium has antithrombotic functions *in vivo*. These studies demonstrated construction of large vessels in a decellularized liver, while microvessels were not observed. In addition, although antithrombotic functions of large vasculatures were confirmed, platelet deposition was still observed in a decellularized liver. To overcome this problem, construction of vascular networks including microvessels is important for liver tissue engineering.

Recent evidence has suggested that mechanical factors (e.g., fluid force) and chemical factors (e.g., surface coating and chemical gradient) can induce *in vitro* formation of microvessels. However, little is known about microvessel formation in a decellularized liver. Therefore, it is important to investigate whether exogenous factors, such as mechanical and chemical factors, can induce the formation of microvessels in a decellularized liver.

In this thesis, effects of mechanical and chemical factors on vascular formation were examined to construct hierarchical vascular networks continuing from large vasculatures to microvessels in a decellularized liver in chapter 2, which corresponded to *in vivo* sinusoidal microvessels. Then, a microfluidic system was employed to obtain useful insights for *in vitro* construction of microcirculation including vascular anastomoses in chapter 3. Next, the validity of constructed vascular networks was determined and optimization of a cell seeding route was performed in a decellularized liver in chapter 4. Finally, conclusions of this thesis were described in chapter 5.

## **Chapter 2 Construction of microvessels in a decellularized liver**

### 2-1 Introduction

Orthotopic liver transplantation is the only treatment for end-stage liver diseases, such as liver cirrhosis (Jadlowiec *et al.*, 2016). However, liver transplantation is limited due to a shortage of organ donors and significant numbers of patients are waiting for vital liver transplants (Caplan, 2016; Murphy *et al.*, 2015). Therefore, it is necessary to investigate alternative therapies to compensate for damaged livers. Previous studies have demonstrated cell transplantation by infusing human hepatocytes via the hepatic vasculature of the recipient (Fox *et al.*, 1998; Fisher and Strom, 2006; Strom and Fisher, 2003). In addition, *in vivo* studies have shown that engineered hepatic tissues (e.g., liver buds and hepatocyte spheroids) and artificial liver support systems, such as the molecular adsorbent recirculation system (MARS), enhance liver function after transplantation (Takebe *et al.*, 2013; Stevens *et al.*, 2017; Sauer *et al.*, 2004). However, liver functions in these studies still remained in the preclinical stage due to technical problems, such as an insufficient number of engrafted hepatocytes. Therefore, construction of a large-scale tissue-engineered liver is needed for liver transplantation.

Whole-organ decellularization is a promising strategy to obtain a large-scale tissue-engineered liver graft. Several studies reported the use of decellularized tissues obtained from animal livers as biomaterials, and demonstrated that decellularized liver scaffolds provided an appropriate environment for hepatic cells (e.g., hepatocytes) as a 3D ECM scaffold (Zhou *et al.*, 2015; Lin *et al.*, 2014; Crapo *et al.*, 2011). For example, decellularized liver scaffolds retain the gross shape of the native liver. In particular, vascular networks, such as the PV, HA, and HV, are preserved in decellularized liver scaffolds, thus enabling surgical anastomosis to host vessels during transplantation. Moreover, liver decellularization can eliminate adverse immune responses because of the removal of cellular components. A previous study demonstrated that decellularized liver

scaffolds filled with hepatocytes through the hepatic vasculature improved liver functions, such as albumin synthesis and urea secretion (Uygun *et al.*, 2010; Yagi *et al.*, 2013; Kadota *et al.*, 2014). In addition, decellularized liver scaffolds promoted the formation of large clusters of HepG2 cells in the parenchyma after 7 days of perfusion culture (Baptista *et al.*, 2016). These findings indicated that recellularized liver grafts successfully mimicked the native liver in terms of structure and function. Thus, transplant experiments are needed to evaluate the potential of tissue-engineered liver grafts for transplantation.

*Ex vivo* blood perfusion using recellularized rat or porcine liver grafts was demonstrated over short periods, such as 24 hours, in previous studies (Uygun *et al.*, 2010; Hussein *et al.*, 2016). However, blood clots developed after long-term transplantation due to the lack of intact endothelium in recellularized liver grafts (Bruinsma *et al.*, 2015). Reendothelialization of decellularized liver scaffolds is an essential step in the preparation of liver grafts because vascular networks in the liver play crucial roles in maintaining physiological conditions *in vivo*, including transport of metabolites and homeostasis (Poisson *et al.*, 2017). In particular, it is important to construct intact vascular networks, which have hierarchical structures ranging from sinusoids to large vasculatures, for the construction of functional tissue-engineered liver grafts. Several studies focused on reconstruction of vasculature in decellularized liver scaffolds (Ko *et al.*, 2015; Hussein *et al.*, 2016). Although large vessels ( $> 50 \mu\text{m}$  in diameter) were constructed in these studies, little is known about the construction of sinusoids ( $< 15 \mu\text{m}$ ).

To construct microvessels *in vitro*, previous studies indicated that both mechanical and chemical factors promoted microvascular formation via angiogenesis. In terms of mechanical factors, several studies demonstrated that FSS induced angiogenesis and promoted the formation of microvascular networks *in vitro*. For example, 0.3 Pa and 0.53 Pa FSS applied to the surfaces of ECs in a parallel-plate flow chamber promoted the formation of capillary networks *in vitro* (Ueda *et al.*, 2004; Kang *et al.*, 2008). Similarly,

1.0 Pa FSS allowed ECs to form capillary sprouts and invade into the surrounding matrix in a microfluidic chip (Galie *et al.*, 2014). On the other hand, in terms of chemical factors, ECM components have been shown to promote capillary formation. In particular, fibronectin enhanced the formation of capillary networks through activation of EC migration and proliferation (Nicosia *et al.*, 1993). Based on these findings, it was hypothesized that the combination of appropriate levels of FSS and fibronectin coating may promote the construction of sinusoid-scale microvessels in decellularized liver scaffolds.

The present study was performed to construct intact vascular networks using decellularized liver scaffolds, focusing on the construction of sinusoid-scale microvessels. First, immunofluorescence staining of decellularized liver scaffolds revealed that ECM networks corresponding to sinusoid structures were not well retained after decellularization. Next, perfusion culture of decellularized livers with ECs promoted the formation of sinusoid-scale microvessels, while sinusoid-scale microvessels were not observed in static culture. Moreover, well-aligned ECs were observed in perfusion culture, while no alignment of ECs was observed in static culture. Finally, it was found that fibronectin coating enhanced the formation of sinusoid-scale microvessels in perfusion culture. These findings are critical for the construction of intact vascular networks, which is an essential step toward the construction of functional tissue-engineered liver grafts using decellularized liver scaffolds.

## 2-2 Experimental design

### Aim

This chapter was designed to construct hierarchical vascular networks including sinusoid-scale microvessels, which may improve antithrombotic functions of a decellularized liver, since formation of microvessels within decellularized livers were not reported in previous studies (Ko *et al.*, 2015; Hussein *et al.*, 2016; Meng *et al.*, 2019).

### Approaches

There is growing evidence that EC morphogenesis can be regulated by cellular microenvironment. In previous studies, the cellular microenvironment has been intentionally manipulated to promote vascular formation *in vitro*. For example, mechanical factors (e.g., FSS and matrix stiffness) and chemical factors (e.g., surface coating and chemical gradient) were reported to regulate *in vitro* formation of microvessels (Ueda *et al.*, 2004; Kang *et al.*, 2008; Galie *et al.*, 2014; Yamamura *et al.*, 2007; Nicosia *et al.*, 1993; Shamloo *et al.*, 2012). Especially, FSS and coating with fibronectin were employed in this decellularized liver model, because they were reported to promote formation of microvessels in previous studies. Therefore, experiments were performed based on the hypothesis that FSS and surface coating with fibronectin can induce formation of hierarchical vascular networks including microvessels (Fig. 2-1).

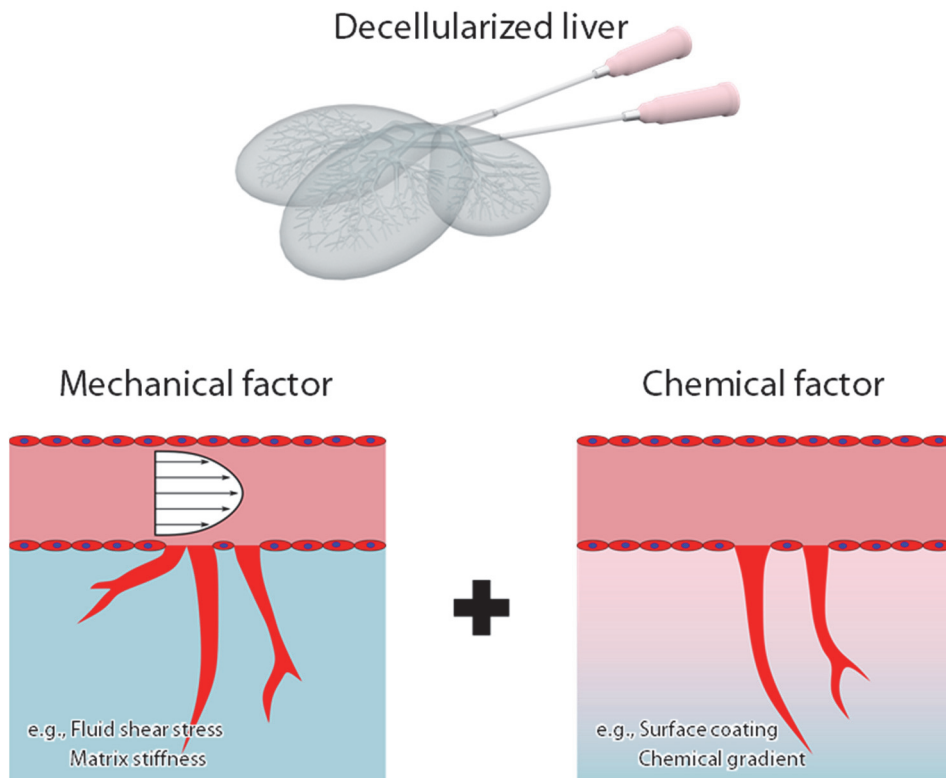


**Fig. 2-1 Experimental design for construction of microvessels in a decellularized liver.** Mechanical factors (e.g., fluid shear stress and matrix stiffness) and chemical factors (e.g., surface coating and chemical gradient) were employed to induce microvessel formation, since they are reported to regulate vascular morphogenesis such as angiogenesis *in vitro*.

### 2-3 Materials and methods

#### 2-3-1 Animal experiment and liver harvest

Male Sprague-Dawley rats (200–250 g; Sankyo Labo Service Corporation, Tokyo, Japan) were used for liver isolation and whole-organ decellularization. All animal experiments were performed in accordance with the Institutional Guidelines on Animal Experimentation at Keio University and approved by the Keio University Institutional Animal Care and Use Committee.

Surgical anesthesia was induced and maintained using inhalation of 2–4% isoflurane. An abdominal incision was made by scissors and 400 U heparin was injected through cardiac puncture to prevent thrombus formation. The PV and inferior vena cava (IVC) were cannulated with 20 G cannulas and ligated with 4-0 silk sutures. Then, 10 ml of phosphate-buffered saline (PBS) containing heparin (5 U/ml) was injected into the rat liver to wash out blood components. The liver was then harvested from the rat and frozen at  $-80^{\circ}\text{C}$  for  $> 24$  hours until use.

#### 2-3-2 Decellularization of rat livers

The protocol to obtain a decellularized liver scaffold was based on a previous report with some modifications (Uygun *et al.*, 2010; Soto-Gutierrez *et al.*, 2011). To remove cellular components in the liver, the following reagents were used during decellularization procedures: (i) ethylene glycol tetraacetic acid (EGTA; Tokyo Chemical Industry Co., Tokyo, Japan), (ii) trypsin (Gibco, Waltham, MA), and (iii) Triton X-100 (Sigma, St. Louis, MO, USA). Harvested livers were thawed in a water bath at  $37^{\circ}\text{C}$  and placed in a perfusion-based decellularization system. The cannula inserted in the PV was connected to a peristaltic pump (Cole-Palmer Instrument Co., Vernon Hills, IL, USA) and perfused with PBS for 1 hour at a rate of approximately 6 ml/min. Subsequently, the liver was perfused with pre-warmed 0.05% trypsin-0.05% EGTA solution for 2 hours to chelate adhesion proteins involved in cell–cell and cell–matrix interactions. Thereafter, 0.5%

Triton X-100-0.05% EGTA solution was perfused through the PV for 3–12 hours to disrupt the lipid membrane of cells and remove cell residues (Fig. 2-2A, B). The liver was then perfused with PBS again for 1 hour to wash out the decellularization solution. After the decellularization procedure, the left lateral lobe, inferior right lobe, anterior caudate lobe, and posterior caudate lobe were removed from the decellularized liver scaffold. Finally, the right median lobe (RML), left median lobe (LML), and superior right lobe (SRL) were used for recellularization experiments. The fabricated decellularized liver scaffold was stored in a refrigerator at 4°C until use.

### 2-3-3 Recellularization of rat livers

In recellularization experiments, green fluorescent protein (GFP)-expressing HUVECs were used for recellularization of vascular networks in decellularized livers. GFP-HUVECs (Angio-Proteomie, Boston, MA) were cultured in Dulbecco's modified Eagle's medium (DMEM) with low glucose (Gibco) supplemented with 10% fetal bovine serum (FBS), 1 mM ascorbic acid 2-phosphate, 10 ng/ml basic fibroblast growth factor (bFGF; PeproTech, Rocky Hill, NJ, USA), and 1% antibiotic-antimycotic solution (Gibco) in a 5% CO<sub>2</sub> incubator at 37°C. The GFP-HUVECs were expanded in collagen-coated culture dishes and cells at passages 5–7 were used for the experiments.

To perform recellularization experiments, GFP-HUVECs were dissociated from culture flasks using Trypsin-EDTA (Gibco) and suspended in culture medium. Cell suspensions of  $1.0 \times 10^7$  GFP-HUVECs were seeded into decellularized liver scaffolds through the PV, divided into two injections (Fig. 2-2C). The number of cells used for recellularization was determined based on previous studies (Baptista *et al.*, 2011, 2016; Kojima *et al.*, 2018). Although a whole rat liver was used in the previous studies, a partial liver, which was approximately 1/2 of the whole liver (Debbaut *et al.*, 2012), was used in this study. In addition, only PV (approximately 1/2 of the total vasculatures) was used for recellularization. Taken together, it was assumed that number of cells needed for

recellularization in this study can be decreased to 1/4 compared to the recellularization of a whole liver. Based on these calculations,  $1.0 \times 10^7$  of GFP-HUVECs were used for recellularization experiments. After 2 hours of incubation for cell attachment, the culture medium was replenished with fresh medium, and the medium was replenished every other day. Fluorescence images of constructed EC networks were observed using a fluorescence microscope (Axio Observer Z1; Carl Zeiss, Oberkochen, Germany) on days 0, 2, 4, and 6. Constructed EC networks in the  $2.5 \text{ mm} \times 2.5 \text{ mm}$  region of interest (ROI) were analyzed using ImageJ (National Institutes of Health, Bethesda, MD, USA). The diameter and length of constructed vessels in decellularized livers were measured and histograms of vessel diameter were produced.

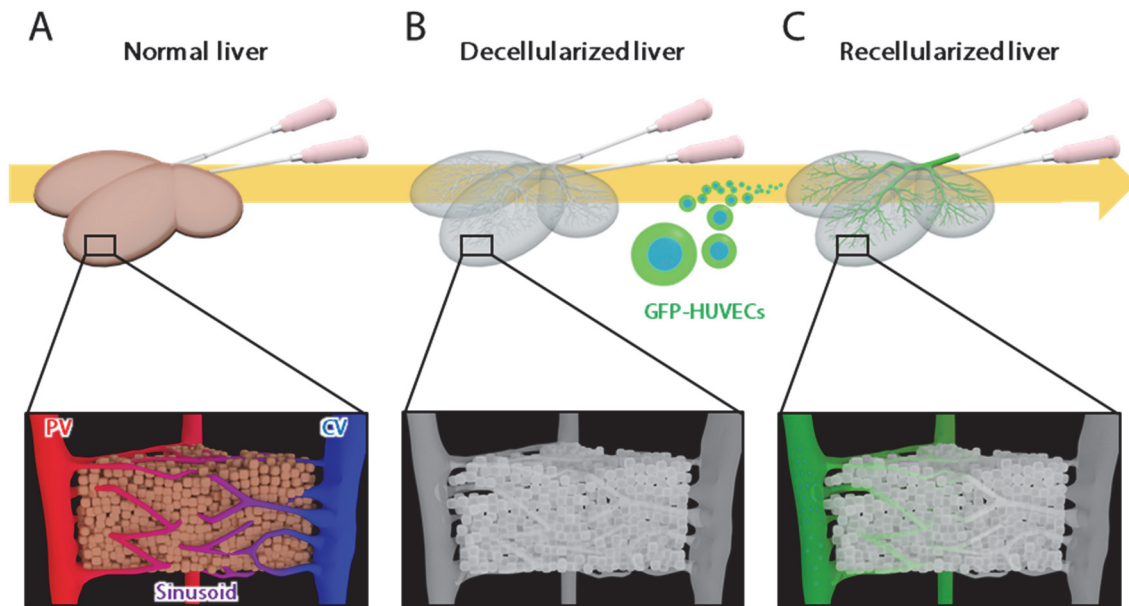


**Fig. 2-2 Schematic illustrations of the experimental configuration for liver decellularization and recellularization.** (A) A hepatic lobule is composed of hepatocytes and vasculatures in normal livers. Branches of the PV travel into sinusoidal capillaries toward the central vein (CV). (B) Whole liver decellularized scaffolds were obtained by perfusing decellularization solutions. (C) Schematic representations of recellularization. GFP-HUVECs (human umbilical vein endothelial cells) were perfused through the PV.

#### 2-3-4 Perfusion culture of recellularized livers

2 hours after cell injection, the recellularized liver was placed in a perfusion chamber and the cannula inserted into the PV of the liver was connected to a peristaltic pump to promote the formation of sinusoid-scale microvessels from these vessels by the flow-induced mechanical stress (Fig. 2-3A). The recellularized liver was then perfused for 2 days. The perfusion rates were determined to apply desired FSS in  $\phi 50 \mu\text{m}$  vessels, which was a mode diameter of constructed vascular networks in a decellularized liver 2 hours after cell seeding. Calculation of flow characteristics was based on previous studies (Debbaut *et al.*, 2012; Moran *et al.*, 2012; Nishii *et al.*, 2016) with some modifications.

To estimate FSS values loaded on different-size vessels in a recellularized liver, PV and HV networks in RML, LML, and SRL were modeled as an electrical model (Fig. 2-3B). All blood vessels of every lobe-specific vascular tree (PV and HV) were modeled using a vascular resistance  $R_s$ , which can be represented as

$$R_s = \frac{8\mu l}{n\pi r^4} [\text{Ns/m}^5] \quad (1)$$

where  $\mu$  is the dynamic viscosity of perfusion fluid [Pa s],  $l$  is the mean blood vessel length [m] for a given generation,  $n$  is the number of blood vessels of the generation, and  $r$  is the mean blood vessel radius [m] of each generation (Debbaut *et al.*, 2012). Moreover, values of  $r$ ,  $l$ , and  $n$  can be estimated by functions of generation number  $j$ . These relational expressions are shown as

$$r = a_r e^{b_r \cdot j} \quad (2)$$

$$l = a_l e^{b_l \cdot j} \quad (3)$$

$$n = a_n e^{b_n \cdot j} \quad (4)$$

where  $a$  and  $b$  are fixed numerical values, which were determined by Debbaut *et al.* (2012) using a lobe-specific fitting algorithm (Table 2-1).

Finally, in the present study, the FSS in recellularized livers was calculated based on Newton's law of viscosity using the viscosity coefficient ( $7.8 \times 10^{-4}$  Pa·s) and density ( $1,000 \text{ kg/m}^3$ ) of culture medium by applying findings reported in previous studies (Debbaut *et al.*, 2012; Nishii *et al.*, 2016). In this perfusion culture, the recellularized liver scaffolds were perfused at flow rates of 2.4, 4.7, or 9.4 ml/min through the PV, corresponding to 0.3, 0.5, and 1.0 Pa FSS on the luminal surface of  $\phi 50 \text{ }\mu\text{m}$  vessels, respectively (Table 2-2).

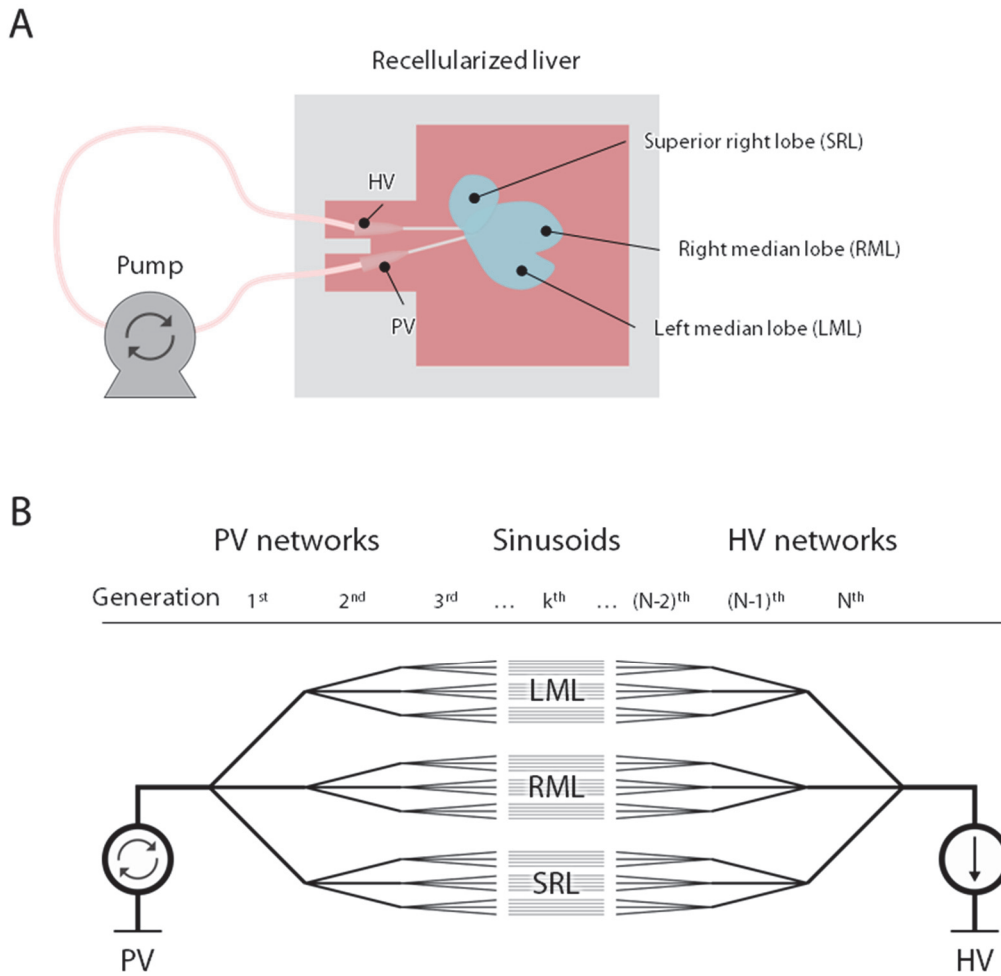


**Fig. 2-3 Mathematical modeling of flow through vascular networks in a recellularized liver.** (A) A schematic illustration of a perfusion system for a decellularized liver seeded with ECs. (B) Multiscale modeling of organ-scale vascular networks (i.e., PV networks, sinusoids, and HV networks) in SRL, RML, and LML of a decellularized liver. Branching blood vessels are categorized as  $j^{\text{th}}$  generation ( $j = 1, 2, \dots, N$ ), and the  $k^{\text{th}}$  generation corresponds to sinusoids in this configuration.

**Table 2-1 Lobe-specific  $a$  and  $b$  values of the exponential trend lines (Debbaut *et al.*, 2012).**

Parameter		$a$			$b$
		SRL	RML	LML	
PV	$r$	1.4	1.4	1.4	-0.34
	$l$	14	12	16	-0.31
	$n$	0.16	0.12	0.11	0.86
HV	$r$	1.9	2.8	2.1	-0.49
	$l$	23	28	31	-0.51
	$n$	0.11	0.12	0.04	1.2

**Table 2-2 Relationship between the inflow (ml/min) through the PV and the estimated FSS (Pa) applied to the luminal surface of  $\phi$  50  $\mu$ m vessels.**

Perfusion culture condition	Static	Low	Middle	High
Inflow through the PV	0 ml/min	2.4 ml/min	4.7 ml/min	9.4 ml/min
FSS applied to the luminal surface of $\phi$ 50 $\mu$ m vessels	0 Pa	0.3 Pa	0.5 Pa	1.0 Pa

### 2-3-5 Fibronectin coating of a decellularized liver

To improve cell adhesion properties in cell–matrix interactions, decellularized liver scaffolds were immersed in 50 µg/ml fibronectin solution (Sigma) overnight before liver recellularization. This concentration of fibronectin was selected because this concentration have been widely used for the improvement of EC attachment in previous studies (Budd *et al.*, 1990; Lee *et al.*, 2009).

### 2-3-6 Immunofluorescence staining and imaging of livers

Paraffin tissue sections from normal and decellularized rat livers were prepared. The samples were treated with 0.1% Triton X-100 for 5 minutes. After rinsing with PBS, the samples were incubated with Block Ace (Dainippon Pharma, Tokyo, Japan) at room temperature for 30 minutes. The samples were then incubated with primary antibodies at 1:200 dilution for 2 hours: rabbit anti-type I collagen (LSL, Tokyo, Japan), rabbit anti-type III collagen (LSL), rabbit anti-type IV collagen (LSL), and rabbit anti-fibronectin (LSL). After three rinses with PBS, the samples were incubated with Alexa Fluor 594-conjugated anti-rabbit IgG antibody (1:200 dilution; Thermo Fisher Scientific) for 2 hours. Finally, cell nuclei were counterstained with DAPI (Sigma). Fluorescence images were obtained using a confocal laser-scanning microscope (LSM700; Carl Zeiss).

### 2-3-7 Evaluation of endothelial cell alignment in perfusion culture

Recellularized livers were fixed with 4% paraformaldehyde (PFA) at 4°C overnight and then permeabilized with 0.1% Triton X-100 overnight. After rinsing with PBS, samples were treated with Block Ace overnight to inhibit nonspecific staining. Samples were then incubated with Alexa Fluor 594-conjugated phalloidin (1:100 dilution; Thermo Fisher Scientific) and Hoechst 33342 (1:500 dilution; Thermo Fisher Scientific) to stain actin filaments and cell nuclei, respectively. Finally, samples were rinsed with PBS.

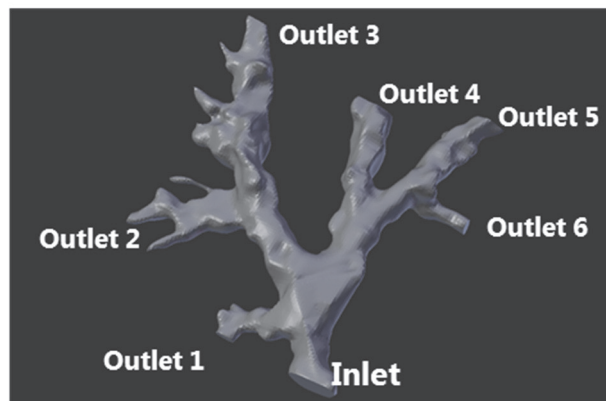
To obtain fluorescence images, samples were placed under an inverted glass-

bottomed dish (No. 1; Iwaki, Shizuoka, Japan). Images were obtained using a two-photon excitation microscope (A1R MP<sup>+</sup>; Nikon, Tokyo, Japan) with a water-immersion lens (Apo LWD 25×/1.10W; Nikon) and ultrafast laser at 950 nm (Insight DeepSee; Spectra-Physics, Santa Clara, CA, USA). Emission signals were split by dichroic mirrors (495- and 560-nm beam splitter) and detected via the GaAsP-type non-descanned detector (GaAsP-NDD; Nikon). An image was acquired with an area of  $506.9 \times 506.9 \mu\text{m}$  ( $512 \times 512$  pixels,  $0.99 \mu\text{m}/\text{pixel}$ ). Image stacks of optical sections were acquired at  $1\text{-}\mu\text{m}$  z-steps. All images were displayed using ImageJ. To evaluate the orientation of GFP-HUVECs exposed to FSS, alignment of actin filaments was analyzed using the ImageJ plugin OrientationJ. The orientation of actin filaments was calculated for each pixel, which was based on the evaluation of the gradient structure tensor in a local pixel neighborhood (Rezakhaniha *et al.*, 2012). A visual color map and histogram of the orientation were obtained.

### 2-3-8 Computational fluid dynamics analysis in a decellularized liver

3D images of peripheral blood vessels constructed on day 0 were obtained by CELL3IMAGER ESTER (SCREEN Holdings, Kyoto, Japan). Volume reconstruction for computational simulation was performed based on 3D images of constructed vessels using the image segmentation software packages Mimics and 3-matic (Materialise, Leuven, Belgium). The 3D mesh data for CFD analysis were generated using ANSYS ICEM CFD 16.2 (ANSYS, Canonsburg, PA) according to the ICEM CFD octree algorithm. Finally, the distribution of FSS applied to the luminal surface of constructed vessels was calculated using ANSYS Fluent 16.2 (ANSYS) based on incompressible Navier-Stokes equations. The boundary conditions at an inlet and outlets were determined by the estimated fluid pressure depending on vascular diameter, since relationship between fluid pressure and vascular diameter was obtained from theoretical calculation described in section 2-3-4. Estimated boundary conditions are as follows (Fig. 2-4).

A



B

Parameter	Diameter [ $\mu\text{m}$ ]	2.4 ml/min	4.7 ml/min	9.4 ml/min
Inlet	110	165 Pa	301 Pa	574 Pa
Outlet 1	53	154 Pa	282 Pa	538 Pa
Outlet 2	31	147 Pa	269 Pa	512 Pa
Outlet 3	51	154 Pa	281 Pa	537 Pa
Outlet 4	91	162 Pa	296 Pa	565 Pa
Outlet 5	51	154 Pa	281 Pa	537 Pa
Outlet 6	46	152 Pa	278 Pa	531 Pa

**Fig. 2-4 Setups for FSS simulation.** (A) A 3D model of blood vessels with an inlet and outlets. (B) The boundary conditions at an inlet and outlets under different flow conditions (2.4, 4.7, 9.4 ml/min). Boundary conditions were calculated from the results of Fig. 2-7D–F. Simulation results are shown in section 2-4-5.

### 2-3-9 Statistical analysis

Experiments were repeated several times to confirm repeatability of the results. Data are presented as means  $\pm$  standard error (SE). Student's t test was used to test for differences between 2 groups and Tukey's multiple comparison test was also used to test for differences among  $> 3$  groups, which were considered statistically significant at  $P < 0.05$ . Statistical analyses were performed using SPSS (IBM, Armonk, NY, USA).

## 2-4 Results

### 2-4-1 Whole-liver decellularization

Decellularization of whole livers was performed by perfusing decellularization solutions, such as trypsin and Triton X-100, through the PV of rat livers. First, the harvested livers were frozen at  $-80^{\circ}\text{C}$  for  $> 24$  hours and thawed for cellular lysis. Each liver was then perfused with trypsin-EGTA through the PV to digest the adhesion proteins involved in cell–cell and cell–matrix interactions. After perfusion with Triton X-100-EGTA, a transparent liver was obtained by solubilizing the cell membranes, which indicated the removal of cellular components from the liver (Fig. 2-5A). Immunofluorescence staining of decellularized liver scaffolds confirmed the absence of cell nuclei (Fig. 2-5B). Histological characterization of the liver ECM showed that ECM proteins, such as type I, III, and IV collagens and fibronectin, were preserved in decellularized liver scaffolds. However, the microarchitectures of type I and III collagens and fibronectin, corresponding to the sinusoid networks in normal livers, were not well retained in decellularized liver scaffolds. These results suggested that decellularized liver scaffolds maintained several liver-specific ECM proteins, while the localization of ECM networks was not well maintained at sinusoid-scale microvessels.

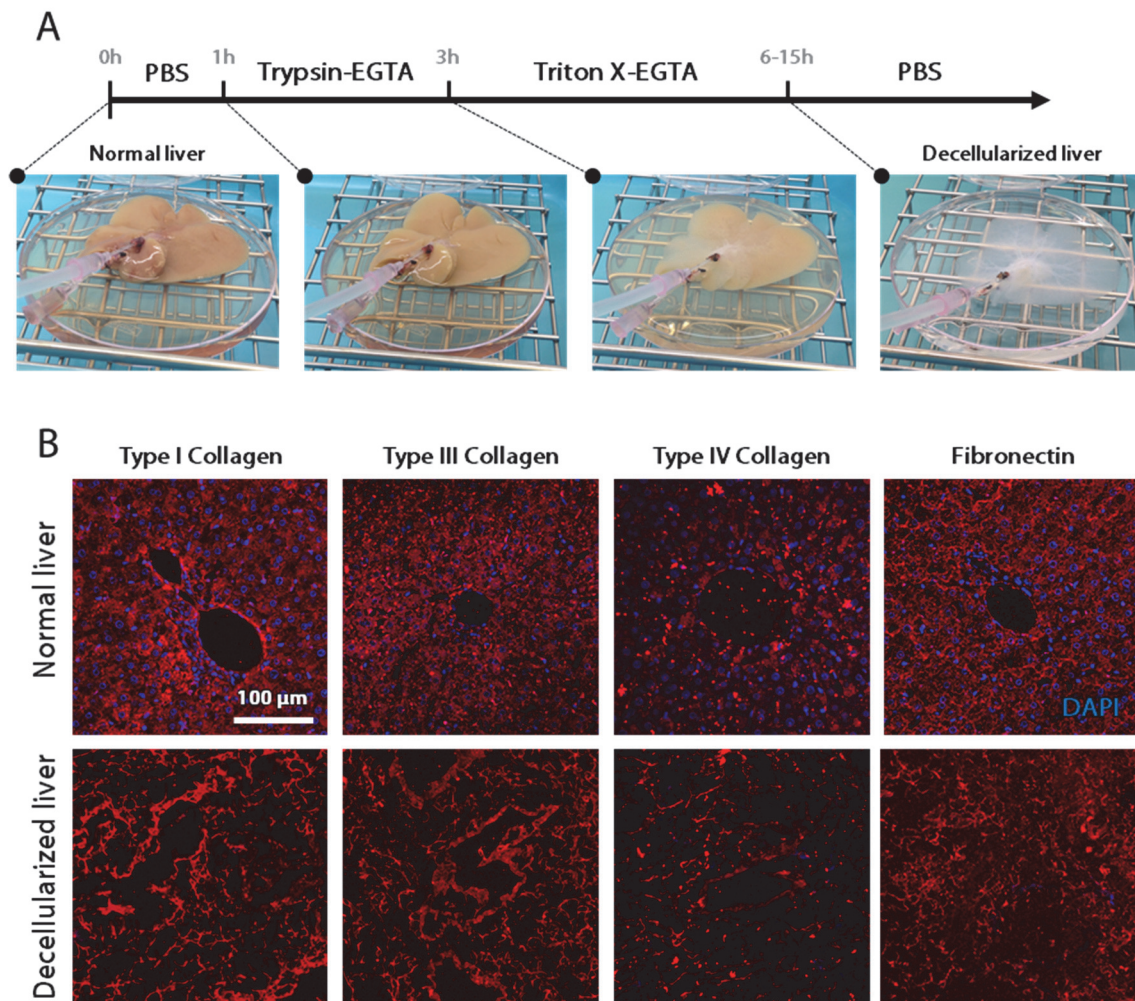


**Fig. 2-5 The process of liver decellularization and immunohistochemistry for ECM components in normal and decellularized liver scaffolds.** (A) Decellularized liver scaffolds were obtained by perfusion with a series of detergent-based decellularization solutions through the PV. The liver became transparent during decellularization process. (B) Immunofluorescence images of the normal liver and the decellularized liver scaffold. These images showed expression of ECM proteins (red), such as type I, III, and IV collagens and fibronectin, and cell nuclei (blue). Scale bar, 100  $\mu\text{m}$ .

### 2-4-2 Reendothelialization of decellularized liver scaffolds using GFP-HUVECs

To reconstruct vascular networks, GFP-HUVECs were injected into a decellularized liver scaffold through the PV. Fluorescence microscopy indicated that GFP-HUVECs were distributed throughout the vascular networks in the decellularized liver scaffold after cell injection (Fig. 2-6A, day 0). Corresponding EC networks were observed on days 0, 2, and 4, and revealed no significant changes in their geometry (e.g., EC sprouting, branching) in static culture (Fig. 2-6A, days 2–4). Quantitative analysis of EC networks showed that hierarchical EC networks ranging 20–140  $\mu\text{m}$  in diameter were constructed in decellularized liver scaffolds (Fig. 2-6B). The modes of the histogram on days 0 and 4 were 50 and 90, respectively, suggesting that the size of the reconstructed vasculature increased over time. In addition, sinusoid-scale microvessels were not observed in static culture (Fig. 2-6B, #).

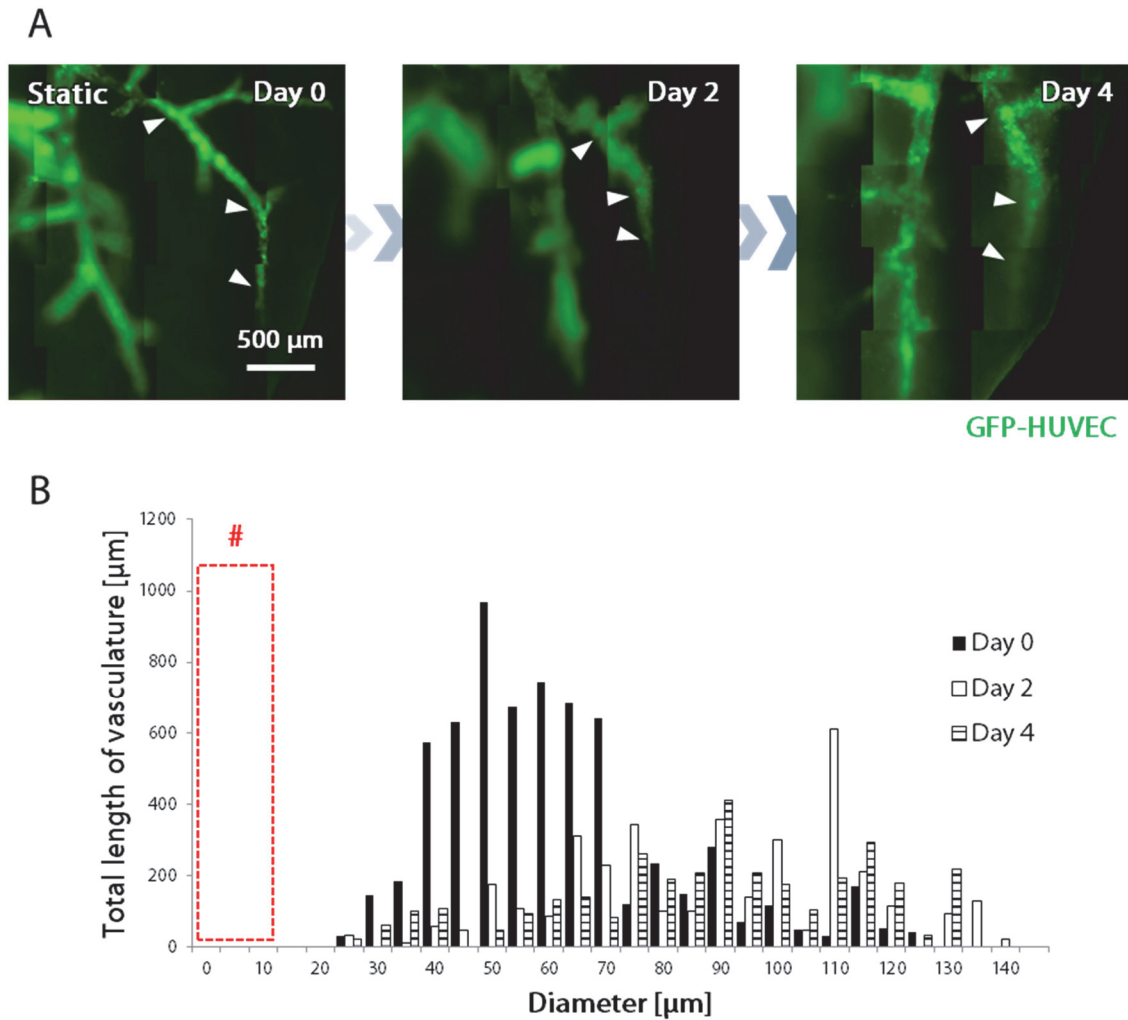


**Fig. 2-6 Observation of constructed EC networks in static culture of decellularized liver scaffolds.** (A) GFP-HUVECs attached to the inner surface of the vascular structure on day 0 and then formed vessel-like networks in decellularized liver scaffolds on day 2 and 4. Arrowheads indicate corresponding vasculature. (B) Histograms of vessel diameter in recellularized liver scaffolds. Sinusoid-scale microvessels (5–15  $\mu\text{m}$ ) were not detected in static culture (#). Data are shown as mean ( $N = 3$ ,  $n = 9$ ). Scale bar, 500  $\mu\text{m}$ .

### 2-4-3 Mechanical stress promoted formation of sinusoid-scale microvessels

Prior to perfusion culture of a decellularized liver, FSS in vascular networks in the liver was modeled and estimated using the Hagen-Poiseuille law. Detailed methods were described in section 2-3-4. The results showed that vascular diameter and length decreased depending on the generation number, while number of blood vessels increased depending on the generation number (Fig. 2-7A–C). Under these perfusion culture conditions (2.4, 4.7, or 9.4 ml/min through the PV), the luminal surface of  $\phi 50 \mu\text{m}$  vessels were exposed to approximately 0.3, 0.5, and 1.0 Pa FSS, respectively (Fig. 2-7D–F).

To examine whether perfusion culture promotes the formation of sinusoid-scale microvessels via angiogenesis in decellularized liver scaffolds, a whole-liver perfusion system using a peristaltic pump was developed (Fig. 2-8A), which provided fluid mechanical stress to GFP-HUVECs attached to the luminal surface of the vasculature (Fig. 2-8B). After 2 days of perfusion culture, EC networks were constructed in decellularized liver scaffolds under different flow rate conditions, of 0, 2.4, 4.7, and 9.4 ml/min (Fig. 2-8C–F). Under all perfusion culture conditions, GFP-HUVECs formed sinusoid-scale microvessels in decellularized liver scaffolds (Fig. 2-8D–F, arrowheads). In most cases, sinusoid-scale microvessels sprouted from  $\phi 50\text{--}60 \mu\text{m}$  vessels.

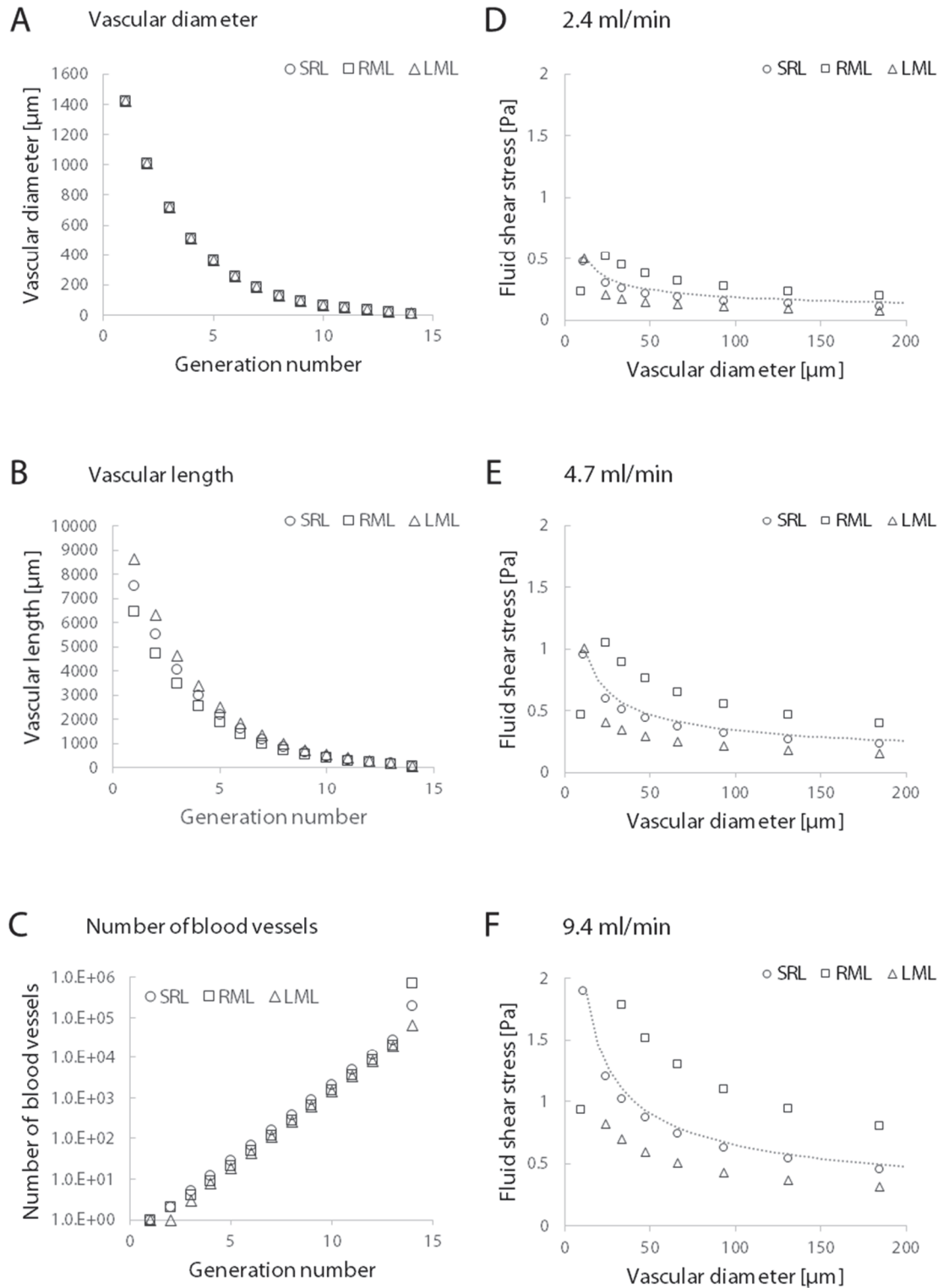


**Fig. 2-7 Topological and fluid properties of vascular networks in a decellularized liver under different perfusion conditions. (A–C) Estimated vascular diameter, length,**

and number of blood vessels in each generation of vascular networks. (D–F) Estimation of fluid shear stress profile in small blood vessels ( $< 200 \mu\text{m}$ ) of SRL, RML, and LML under different flow rate conditions (2.4, 4.7, and 9.4 ml/min).

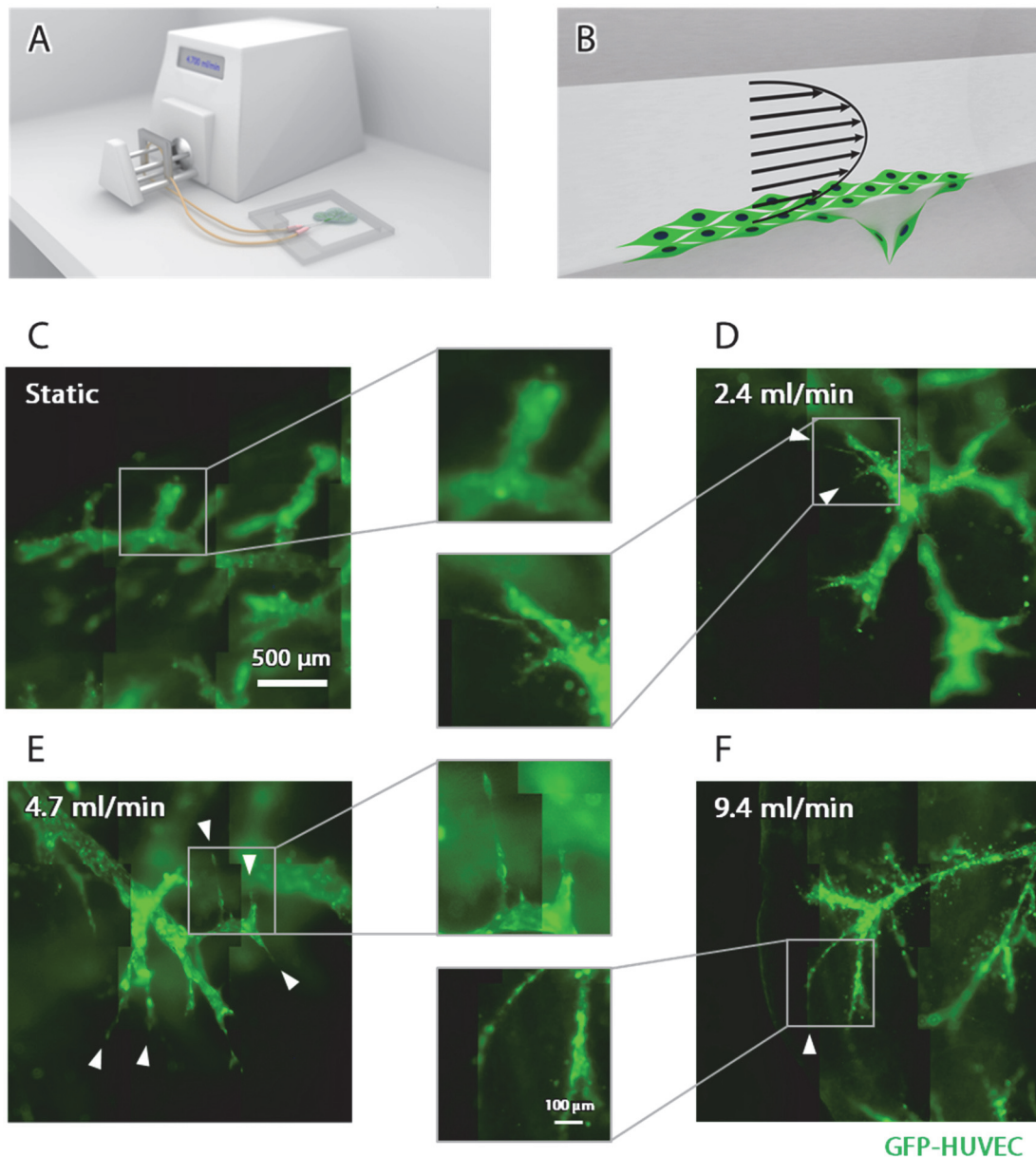


**Fig. 2-8 Fluorescence images of constructed EC networks under different flow rate conditions on day 2.** (A) A schematic illustration of a perfusion culture system. The recellularized liver was placed in a perfusion chamber and connected to a peristaltic pump. (B) A schematic illustration of the cells in a decellularized liver scaffold. (C) Fluorescence images of GFP-HUVECs in static culture on day 2. (D–F) Fluorescence images showed that GFP-HUVECs formed EC sprouts (arrowheads) in perfusion culture (D: 2.4 ml/min; E: 4.7 ml/min; F: 9.4 ml/min) on day 2. Scale bars, 500, 100 μm.

Quantitative analysis of constructed EC networks in decellularized liver scaffolds showed that perfusion culture conditions promoted the formation of sinusoid-scale microvessels, while no sinusoid-scale microvessels were observed in static culture (Fig. 2-9A, #). In addition, the middle perfusion rate (4.7 ml/min) resulted in the formation of a greater number of sinusoid-scale microvessels compared to the other perfusion rates (low: 2.4 ml/min; high: 9.4 ml/min) (Fig. 2-9B). On the other hand, there was no significant difference in the length of sinusoid-scale microvessels among the perfusion rates (Fig. 2-9C). These results indicated that perfusion culture was important for the reconstruction of sinusoid-scale microvessels in decellularized liver scaffolds.

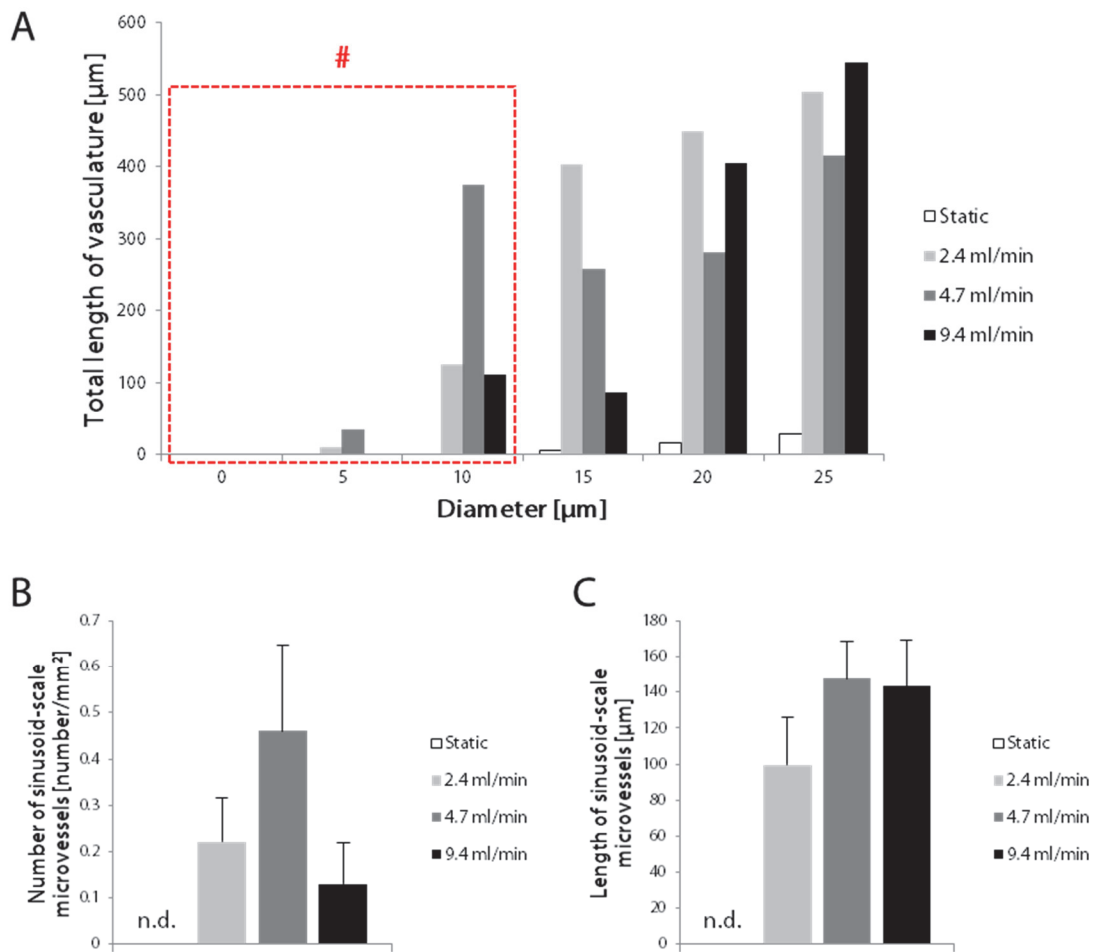


**Fig. 2-9 Quantitative analysis of EC diameter and sinusoid-scale microvessels on day 2.** (A) Histograms of vessel diameter in static and perfusion culture conditions on day 2. The low, middle, and high perfusion rates (2.4, 4.7, and 9.4 ml/min, respectively) promoted the formation of sinusoid-scale microvessels (#). (B) Quantitative analysis of the number of constructed sinusoid-scale microvessels ( $< 15 \mu\text{m}$ ) in recellularized liver scaffolds. “n.d.” means “not detected”. (C) Quantitative analysis of the average length of sinusoid-scale microvessels. Data are shown as mean  $\pm$  SE ( $N = 3, n = 9$ ).

### 2-4-4 Chemical modification enhanced the formation of microvessels

To examine whether enhanced cell–matrix adhesion promotes the formation of sinusoid-scale microvessels, the inner surface of decellularized liver scaffolds was coated with fibronectin before recellularization. Fluorescence images showed that fibronectin coating of decellularized liver scaffolds promoted the formation of sinusoid-scale microvessels after 2 days of perfusion culture at 4.7 ml/min (Fig. 2-10A–B). These observations indicated that sinusoid-scale microvessels were effectively constructed using a combination of fibronectin coating of decellularized liver scaffolds and perfusion culture at 4.7 ml/min. Quantitative analysis showed that the formation of EC networks, including sinusoid-scale microvessels, was enhanced in fibronectin-coated scaffolds (Fig. 2-10C). Moreover, the number of sinusoid-scale microvessels was significantly increased by fibronectin coating (Fig. 2-10D). These results suggested that, in addition to perfusion culture, improvement of the adhesion properties of scaffolds was also important for the reconstruction of sinusoid-scale microvessels in decellularized liver scaffolds.

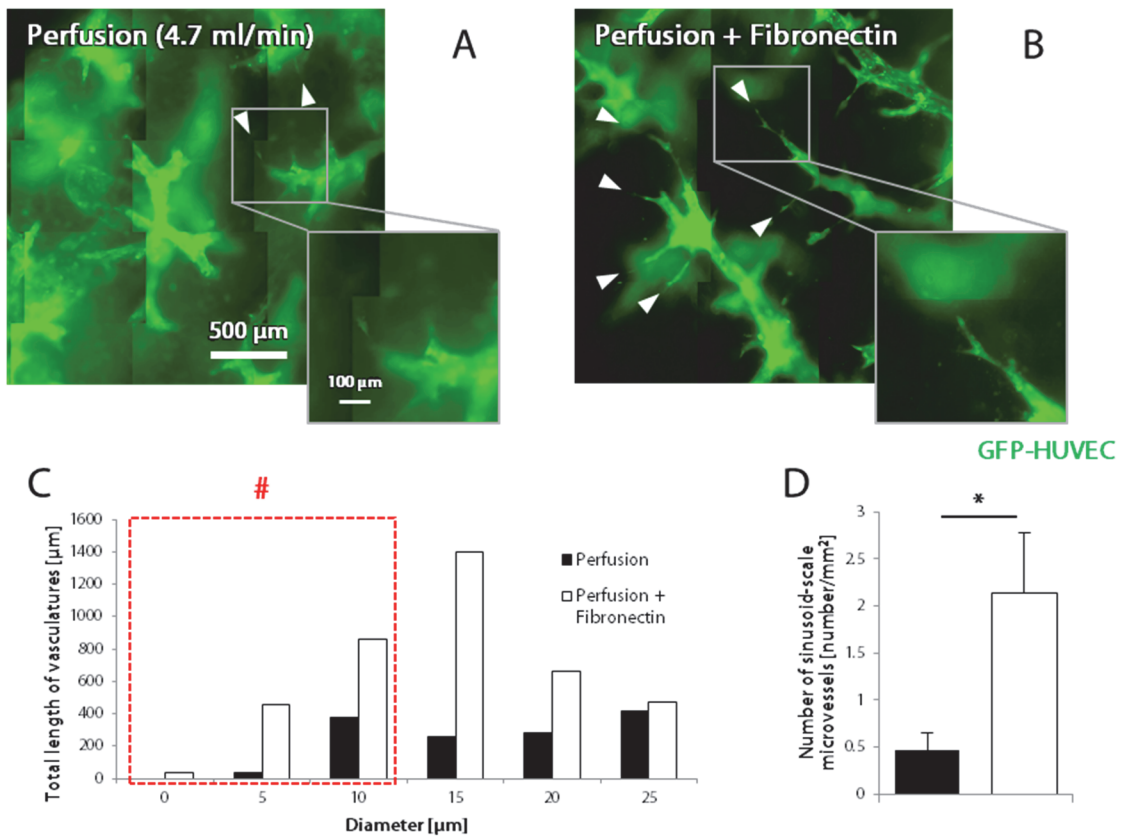


**Fig. 2-10 Fluorescence images of constructed sinusoid-scale microvessels in fibronectin-coated decellularized liver scaffolds.** (A) GFP-HUVECs formed sinusoid-scale microvessels in perfusion culture at 4.7 ml/min. (B) Sinusoid-scale microvessels were formed in fibronectin-coated decellularized liver scaffolds. Arrowheads indicate newly formed sinusoid-scale microvessels. (C) Histograms of vessel diameter in the recellularized liver scaffolds. Quantitative analysis shows that fibronectin-coated decellularized liver scaffolds enhanced the formation of sinusoid-scale microvessels compared to uncoated scaffolds (#). (D) The number of sinusoid-scale microvessels in decellularized liver scaffolds. Data are shown as mean  $\pm$  SE (N = 3, n = 9). Scale bars, 500, 100  $\mu$ m. \* $P$  < 0.05.

### 2-4-5 Alignment of GFP-HUVECs in perfusion culture

ECs elongate and align along the flow direction when continuously exposed to flow, because they sense flow-induced mechanical stimulation, such as FSS. Therefore, the morphology of GFP-HUVECs in decellularized liver scaffolds was analyzed to investigate whether the cells recognized FSS in this perfusion culture at 4.7 ml/min. Well-aligned GFP-HUVECs were observed on two-photon excitation laser microscopy after 2 days of perfusion culture (Fig. 2-11B, C), while no alignment was observed in static culture (Fig. 2-11A). To further investigate the alignment of cells in perfusion culture, fluorescence images were analyzed by OrientationJ to obtain color-coded images. These images showed that cortical actin and actin filaments of GFP-HUVECs were oriented along the central axis of the vasculature in perfusion culture (Fig. 2-11E, F), while those in static culture were not oriented in a specific direction (Fig. 2-11D). Quantitative analysis of the filament orientation clearly showed a significant peak in perfusion culture (Fig. 2-11H, I) compared to a flat distribution in static culture (Fig. 2-11G). In particular, the combination of perfusion culture and fibronectin coating represented higher peak value compared to the condition without fibronectin coating (Fig. 2-11H, I).

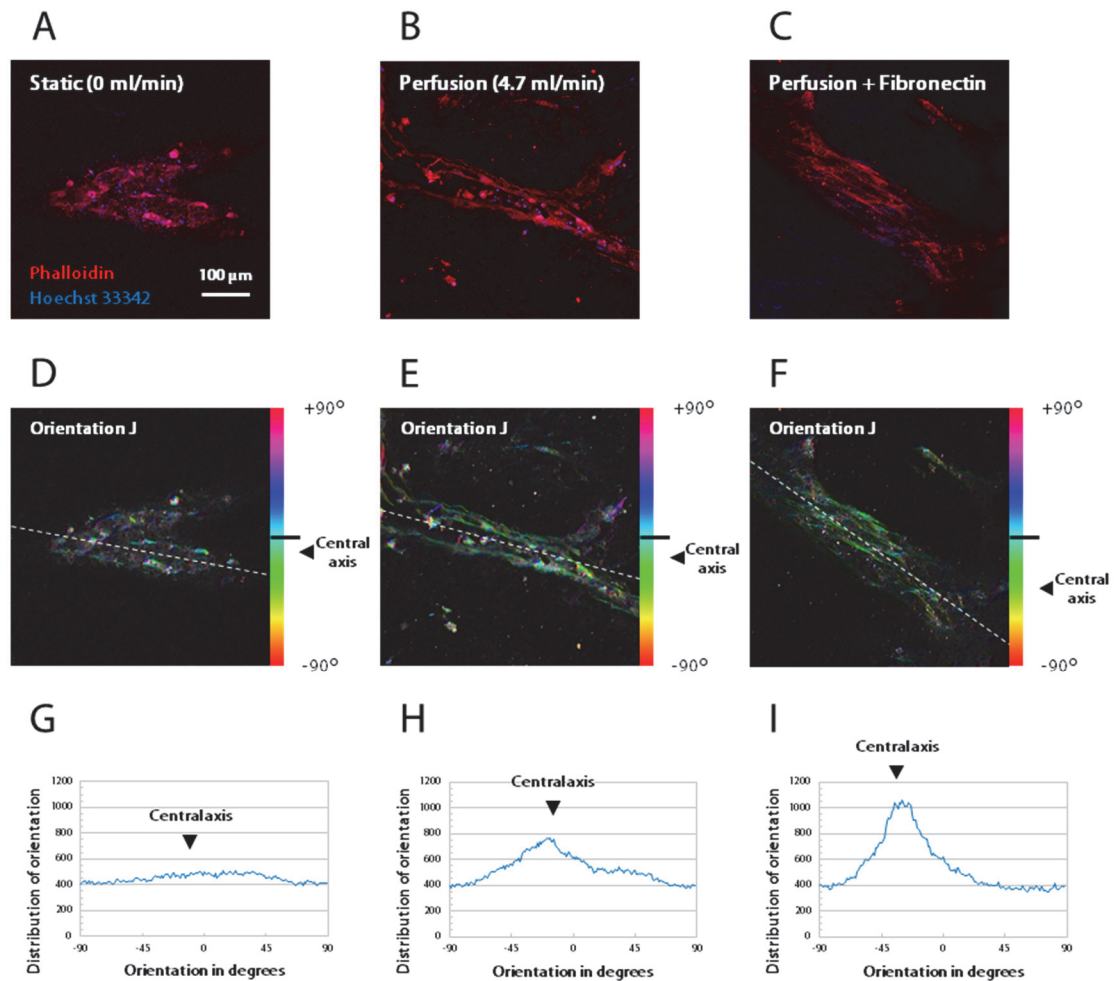


**Fig. 2-11 The Orientation of HUVECs in the recellularized liver in static and perfusion culture.** (A–C) Fluorescence images of HUVECs in a decellularized liver scaffold in static culture (A), perfusion culture at 4.7 ml/min (B), and the combination of perfusion culture at 4.7 ml/min and fibronectin coating (C). These images represent actin filaments stained with phalloidin (red) and cell nuclei stained with Hoechst 33342 (blue). (D–F) Color-coded images represent local orientation of actin filaments for each pixel in each condition. The dashed lines in the images represent the central axis of vessels. (G–I) Quantitative analysis of the filament orientation.

To investigate the FSS distribution on the lumen of vascular networks in detail, FSS was estimated using CFD analysis, based on previous reports with some modifications (Nishii *et al.*, 2016; Debbaut *et al.*, 2012). The results showed that the FSS values in decellularized liver scaffolds increased in accordance with volume flow rate at the PV (Fig. 2-12A–C). In addition, various levels of FSS were calculated depending on the geometry of vascular networks. For example, higher FSS was shown around vascular branches. These results indicate that both volume flow rate at the PV and the geometrical characteristics of vascular networks had an important effect on the level of local FSS.

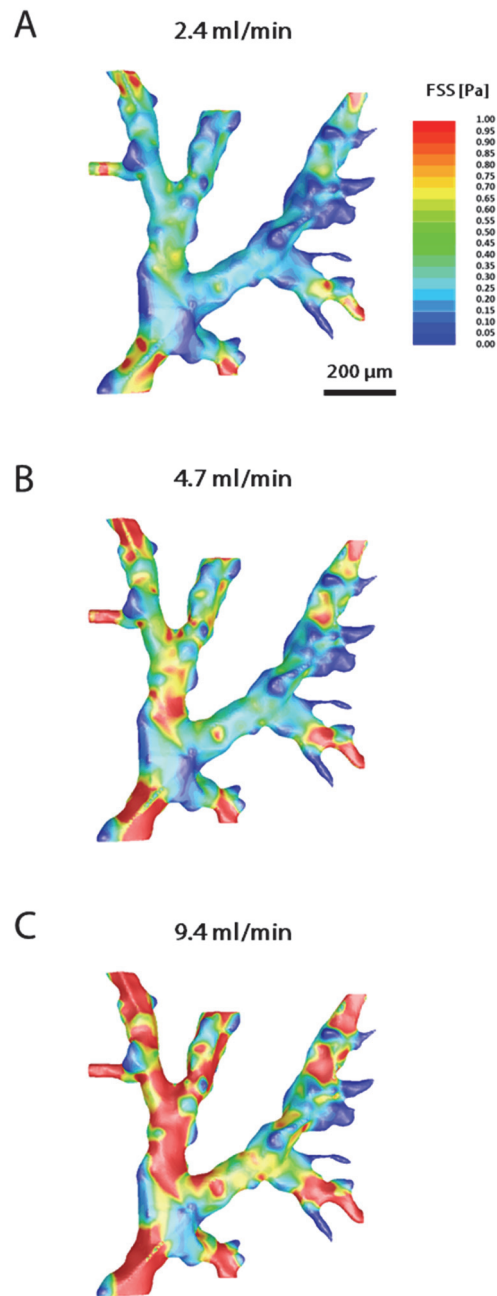


**Fig. 2-12 The distribution of FSS applied to the luminal surface of microvessels in different perfusion conditions.** (A–C) The contour plot displays the distribution of FSS applied to the luminal surface of constructed vascular network in low (A: 2.4 ml/min), middle (B: 4.7 ml/min), and high (C: 9.4 ml/min) perfusion culture conditions, respectively. Scale bar, 200  $\mu\text{m}$ .

## 2-5 Discussion

### 2-5-1 Liver tissue engineering using decellularized livers

The construction of an organ-scale liver tissue is a key challenge in the field of tissue engineering (Sudo, 2014). Previous studies have demonstrated that decellularized liver scaffolds provide suitable environments for parenchymal cells, such as hepatocytes and HepG2 cells (Uygun *et al.*, 2010; Soto-Gutierrez *et al.*, 2011; Baptista *et al.*, 2011; Yagi *et al.*, 2013; Kadota *et al.*, 2014; Shirakigawa *et al.*, 2013, 2012). However, little is known about the ability of decellularized liver scaffolds to facilitate construction of vascular networks, especially in terms of sinusoids. Therefore, the present study focused on the construction of hierarchical vascular networks, continuing from sinusoid-scale microvessels to large vasculatures, in decellularized liver scaffolds.

### 2-5-2 Disruption of extracellular microarchitectures in a decellularized liver

In this decellularization processes, chemical and enzymatic methods were used to eliminate cell components. The results indicated that several liver-specific ECM proteins, such as type I, III, and IV collagens and fibronectin, were retained in decellularized liver scaffolds. However, structural disruption of type I and III collagen and fibronectin networks was observed. In normal liver tissues, type I collagen and fibronectin are present in parenchymal tissues and sinusoids, while type III collagen was reported to be present along sinusoids as part of reticular fibers, which form a delicate meshwork providing support for hepatocytes, in the normal liver (Unsworth *et al.*, 1982; Yamamoto and Tahara, 1984). On the other hand, type IV collagen is present at the BM of large vessels (Yamamoto and Tahara, 1984). The results suggested that ECM microarchitectures of large vessels were retained. However, those of sinusoids were not well retained after the decellularization process and liver sinusoids have no BM. In addition, the subendothelial space of Disse contains various ECM proteins at low density. These characteristics of liver sinusoids suggest that the ECM microarchitecture around sinusoids is fragile, and

cannot be maintained after the decellularization processes. This is consistent with the structural disruption of ECM networks observed in the present study.

### 2-5-3 Recellularization of a decellularized liver

As the results revealed that sinusoidal ECM microarchitecture was not well retained in the decellularized liver, the present study aimed to construct vascular networks in the decellularized livers, focusing on sinusoid-scale microvessels. As expected, sinusoid-scale microvessels were not observed in decellularized liver scaffolds in static culture, while vascular networks with vessels of diameter  $> 20 \mu\text{m}$  were successfully constructed. These results suggested that ECs failed to construct sinusoid-scale microvessels, possibly because sinusoidal ECM microarchitectures were not well retained. Although other groups have reported the construction of vascular networks in decellularized liver scaffolds, they did not focus on the construction of sinusoid-scale microvessels. For example, rat decellularized liver scaffolds were recellularized with HUVECs, which resulted in the construction of hierarchical vascular networks (Shirakigawa *et al.*, 2013). In addition, primary rat liver sinusoidal endothelial cells (LSECs) and an immortalized EC line formed luminal structures of large vessels in decellularized liver scaffolds (Hussein *et al.*, 2016; Kojima *et al.*, 2018; Ko *et al.*, 2015). However, in these studies, fluorescence images represented the construction of vessels  $> 20 \mu\text{m}$  in diameter. In addition, Ko *et al.* demonstrated that reendothelialization of decellularized porcine liver scaffolds significantly reduced platelet adhesion, while slight accumulation of platelets was detected in extravascular regions.

### 2-5-4 Mechanical stress induced formation of microvessels

To promote the construction of sinusoid-scale microvessels in decellularized liver scaffolds, both mechanical and chemical factors were employed, because both of these factors were shown to induce the formation of microvessels in biomimetic microfluidic

chip models (Bogorad *et al.*, 2015). Firstly, perfusion culture was performed to apply 0.3–1.0 Pa FSS to the cells on the lumen of  $\phi$  50–60  $\mu\text{m}$  vessels. The results indicated that perfusion culture, especially at a flow rate of 4.7 ml/min (corresponding to 0.5 Pa FSS), enhanced the formation of sinusoid-scale microvessels, whereas no sinusoid-scale microvessels were detected in static culture. The most important point of these results was that sinusoid-scale microvessels were constructed by flow-induced mechanical stimulation, which were not constructed in static culture. These findings suggested that FSS induced the formation of vascular sprouts, resulting in the formation of sinusoid-scale microvessels in the perfusion culture of decellularized liver scaffolds. FSS has been reported to induce angiogenesis both *in vitro* and *in vivo* (Bernabeu *et al.*, 2014; Galie *et al.*, 2014). For example, ECs invaded into collagen gel to form 3D vascular networks when exposed to 0.3 Pa FSS for 48 hours in a parallel-plate flow chamber (Ueda *et al.*, 2004). In addition, 0.53 Pa FSS allowed HUVECs to form microvessels via angiogenesis through Akt phosphorylation and activation of matrix metalloproteinase (MMP)-2 (Kang *et al.*, 2008). On the other hand, 1.0 Pa intraluminal FSS triggered the formation of microvessels in microfluidic chips through activation of MMP-1 (Galie *et al.*, 2014). Furthermore, several studies showed that FSS upregulated the expression of angiogenic factors, such as VEGF, MMP-1, and MT1-MMP (Wragg *et al.*, 2014; Buchanan *et al.*, 2014). These previous studies suggested that construction of sinusoid-scale microvessels in the present study was promoted through the upregulation of VEGF and MMP induced by FSS.

In the present study, sinusoid-scale microvessels were effectively constructed in perfusion culture. There are two possibilities that perfusion culture promoted the construction of sinusoid-scale microvessels. First, perfusion culture promoted the vascular formation through increased delivery of oxygen and nutrients. Second, perfusion culture promoted the vascular formation through flow-induced mechanical stress. In the present study, it was hypothesized that flow-induced mechanical stress was involved in

the formation of sinusoid-scale microvessels. Therefore, it was investigated whether ECs recognized FSS in perfusion culture. The results verified that ECs sensed FSS in perfusion culture at 4.7 ml/min by quantitative analysis of actin filament alignment, which clearly showed that local orientation of actin filaments in ECs were aligned in the flow direction, whereas no alignment was detected in static culture. It is well known that ECs elongated and aligned parallel to the flow direction when they were exposed to FSS. For example, Ishibazawa *et al.* (2011) demonstrated such EC alignment using a flow chamber. In addition, actin filaments were also aligned parallel to the flow direction (van der Meer *et al.*, 2010). These endothelial morphological changes are key features of ECs in flow culture. It is also known that EC alignment is induced in response to FSS, both *in vivo* and *in vitro*, through mechanotransduction pathways (Yamamoto *et al.*, 2003; Dewey CF Jr, Bussolari SR, Gimbrone MA Jr, 1981). For example, 1.0 Pa FSS induced HUVEC alignment in the flow direction with an orbital shaker, and 2.0 Pa FSS promoted the alignment of actin filaments in HUVECs seeded on top of a 3D collagen gel scaffold (dela Paz *et al.*, 2012; Mina *et al.*, 2016). In addition, an effect of FSS on human retinal microvascular ECs was investigated in a parallel-plate flow chamber, and the results indicated that 0.6 Pa FSS induced EC alignment (Ishibazawa *et al.*, 2011). Moreover, FSS is known to regulate the permeability of EC monolayers (Price *et al.*, 2010; Colgan *et al.*, 2007). Previous *in vitro* studies demonstrated that FSS also enhanced vascular properties such as barrier function, mechanical strength, and vasodilation of the vessel (Quint *et al.*, 2011; Jung *et al.*, 2015; Price *et al.*, 2010). Although effects of increased delivery of oxygen and nutrients were remained unclear, the increased flow rate resulted in the decreased number of sinusoid-scale microvessels (9.4 ml/min) possibly due to upregulation of apoptosis pathway. A previous study demonstrated that ECs exposed to 1.2 Pa FSS resulted in enhanced apoptosis in a parallel plate flow chamber (Rennier and Ji, 2012). These findings suggested that FSS was at least partly involved in microvessel formation.

### 2-5-5 Chemical factor promoted formation of microvessels

Coating with fibronectin was also performed, to induce the formation of sinusoid-scale microvessels in decellularized livers. These results indicated that fibronectin coating significantly enhanced the formation of sinusoid-scale microvessels. ECM proteins are known to have important roles in cell-matrix attachment and a variety of EC activities. In a previous study, the effects of surface treatment with various ECM proteins on EC attachment were evaluated using polymeric scaffolds. Specifically, various ECM proteins, such as type I collagen, BM proteins (e.g., laminin and Matrigel), and fibronectin, were compared (Lee *et al.*, 2009). The results indicated that coating with laminin or fibronectin enhanced EC attachment on the scaffolds, although coating with type I collagen showed no difference compared to the uncoated scaffolds. Another group also demonstrated that coating of scaffolds with BM proteins enhanced EC–matrix adhesion in microfluidic channels. However, coating with BM proteins resulted in downregulation of vascular sprouting (Han *et al.*, 2015). On the other hand, fibronectin coating of decellularized fibroblast-derived ECM was reported to enhance the formation of microvessels *in vitro* (Mina *et al.*, 2016; Nicosia *et al.*, 1993). Moreover, FSS was reported to enhance EC migration via fibronectin receptor subunits,  $\alpha_5$  and  $\beta_1$  integrins (Urbich *et al.*, 2002). Taken together, these results suggest that coating with fibronectin rather than BM proteins is useful in terms of vascular sprouting. Accordingly, fibronectin coating in the present study appeared to improve both cell–matrix attachment and the formation of vascular sprouting in decellularized liver scaffolds, which was consistent with the enhanced formation of sinusoid-scale microvessels in fibronectin-coated decellularized livers.

### 2-5-6 Limitations and forthcoming challenges

Although hierarchical EC networks including sinusoid-scale microvessels were successfully constructed in decellularized liver scaffolds, there were some limitations.

First, antithrombotic functions of the constructed EC networks were not evaluated. For example, previous studies evaluated platelet adhesion on the luminal surface of the vasculature, to test the biocompatibility of recellularized liver grafts with ECs (Ko *et al.*, 2015; Hussein *et al.*, 2016; Kojima *et al.*, 2018). This platelet adhesion test is very important to evaluate whether constructed vessels was functional in decellularized liver scaffolds. However, in this study, the luminal surface of PV networks was recellularized with GFP-HUVECs, while that of HV networks remained as bare ECM fibers due to the absence of ECs. Although this seeding method has advantages in reducing the amount of cells needed in experiments and the requirement for detailed observation of microvessels, bare ECM fibers of HV networks may facilitate platelet accumulation. To evaluate platelet adhesion, reendothelialization of whole vascular networks, including PV, HV, and sinusoidal networks, will be needed. Second, CFD analysis revealed that ECs were exposed to various levels of FSS depending on both the geometry of vascular networks and the perfusion rate at the PV, which might be related to the morphology of ECs. However, it was difficult to investigate this potential correlation between EC morphology and FSS because only limited regions could be observed even by two-photon excitation microscopy. Third, GFP-HUVECs were employed for the construction of sinusoid-scale microvessels. Although HUVECs have been widely used in experiments on vascular formation, hepatic sinusoids are composed of LSECs, which are different from normal ECs in several respects, such as cell surface markers and fenestration (Poisson *et al.*, 2017). Therefore, LSECs are an ideal cell source for reendothelialization of decellularized livers. However, the long-term culture of LSECs has proven challenging, which has limited their use for reendothelialization of decellularized liver scaffolds. Finally, parenchymal cells, such as hepatocytes, were not used in the present study. As this study focused on analysis of vascular formation processes in decellularized livers, which cannot be observed by seeding of hepatocytes, only ECs were used in this study. Further investigations will be needed to evaluate the interactions between hepatocytes and ECs.

### 2-6 Summary

This chapter demonstrated the construction of hierarchical EC networks in decellularized liver scaffolds. The results indicated that sinusoid-scale microvessels were constructed in perfusion culture. In particular, range of FSS was important and 0.3–1.0 Pa FSS loaded on luminal surface of peripheral blood vessels ( $\phi$  50–60  $\mu\text{m}$ ) was critical for the construction of sinusoid-scale microvessels. Moreover, these results suggested that the combination of appropriate levels of FSS and fibronectin coating enhanced the formation of sinusoid-scale microvessels in decellularized liver scaffolds. This formation of sinusoid-scale microvessels is a critical step for the development of intact vascular networks, to address the limitations of recellularized liver scaffolds after transplantation, such as hemorrhage and thrombosis.

In this chapter, although PV networks including sinusoid-scale microvessels were constructed, HV networks remained as bare ECM fibers due to the absence of ECs. To extend PV networks, it is essential to investigate how to form HV networks and vascular anastomoses between PV and HV networks. However, there were some limitations of decellularized liver model such as difficult observation of thick tissues and a lot of animal sacrifice. To overcome these limitations, *in vitro* microfluidic system was employed to investigate how to form vascular anastomoses in the following chapter (Fig. 2-13).

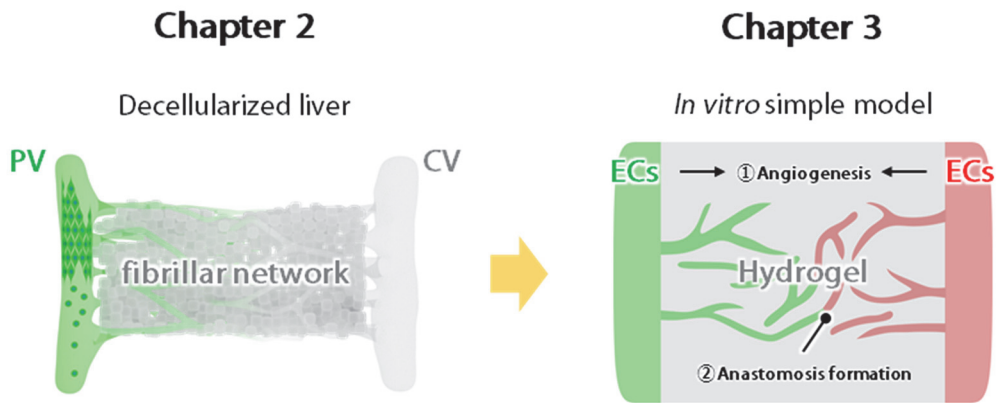


**Fig. 2-13 Strategic direction for *in vitro* formation of microvascular networks.** In chapter 2, mechanical and chemical factors induced the formation of sinusoid-scale microvessels in a decellularized liver, while entire HV networks were not constructed (left panel). Hence, in chapter 3, an *in vitro* simple model was developed to conduct experiments focusing on microvascular formation in a fibrillar network, since a simple model would be desirable to perform effective investigation of vascular formation including vascular anastomoses (right panel).

## **Chapter 3 Investigation of microvascular formation using a microfluidic chip**

### 3-1 Introduction

The demand for organ transplantation has rapidly increased over the past few decades due to a huge number of patients with chronic organ failure. However, organ shortage is a critical problem in medical transplantation, including liver and kidney (Caplan, 2016; Hong *et al.*, 2014). To overcome this problem, it is necessary to construct transplantable organ/tissue grafts *in vitro*. Over the last decade, researchers have attempted to construct transplantable bioengineered tissue grafts *in vitro* (Stevens *et al.*, 2017; Palakkan *et al.*, 2013; Kasuya *et al.*, 2012). Despite significant efforts, these studies remain in early stages of research due to poor graft survival after transplantation (Caralt *et al.*, 2015; Damania *et al.*, 2014).

To improve graft survival, rapid blood perfusion is required for maintenance of implanted tissue grafts after transplantation. For this reason, formation of vascular anastomoses is necessary for transplantation. Previous studies have demonstrated two approaches to construct vascular anastomosis. One is surgical anastomosis between implanted vessels of tissue-engineered grafts and host vessels of recipients (Brennan *et al.*, 2008). The other is anastomosis through self-organization between implanted EC networks and host vessels (Takebe *et al.*, 2014; Sekine *et al.*, 2013). In particular, the latter is critical for implantation because *in vivo* microvessel-scale anastomosis depends on self-organization of ECs (Bogorad *et al.*, 2015; Huang *et al.*, 2015). For example, a previous study reported transplantation of bioengineered tissue grafts, and succeeded in blood perfusion between engineered vessels and host vessels (Cheng *et al.*, 2011). However, processes of anastomosis formation between these vessels remained unclear due to difficulties in observation after transplantation.

Several studies have demonstrated *in vitro* vascular anastomosis models using

microfluidic chips, which have advantages for investigating processes involved in vascular anastomosis. For example, previous studies have successfully demonstrated formation of vascular anastomosis in a gel scaffold via angiogenesis and vasculogenesis in HUVEC monoculture (Wang *et al.*, 2016; Song *et al.*, 2012; Yeon *et al.*, 2012). These vascular networks failed to maintain their small luminal size and structures in long-term culture due to the lack of perivascular cells (e.g., mural cells and pericytes). *In vivo* vascular anastomoses are formed between engineered and host vessels, which include both ECs and perivascular cells. Therefore, it is necessary to establish an *in vitro* vascular anastomosis model, including perivascular cells, to further understand processes of *in vivo* vascular anastomosis formation.

To mimic *in vivo* vascular anastomosis formation, it is important to construct vessels covered with perivascular cells in a microfluidic chip. Previously, it was demonstrated coculture of HUVECs and human bone marrow-derived MSCs in a microfluidic chip and successfully constructed vascular networks covered with pericyte-like perivascular cells which expressed  $\alpha$  smooth muscle actin (SMA) (Yamamoto *et al.*, 2013). In addition, recent study demonstrated that vessels constructed in the HUVEC-MSC coculture model were in good agreement with *in vivo* microvessels in terms of morphology and function (Uwamori *et al.*, 2019; Yamamoto *et al.*, 2019). Thus, it is hypothesized that HUVEC-MSC coculture might be useful for establishment of an *in vitro* vascular anastomosis model by mimicking the *in vivo* microvessels covered by perivascular cells.

The study described in the present chapter investigated how to form vascular anastomoses between vessels with perivascular cells and nascent vessels using a microfluidic chip (Watanabe and Sudo, 2019). HUVEC monoculture demonstrated that ECs failed to form vascular anastomoses. HUVEC-MSC coculture was performed to induce angiogenesis, which led to formation of vascular anastomosis by day 10. This vascular anastomosis was constructed between nascent vessels and stable vessels, which were covered by MSC-derived perivascular cells. Furthermore, processes of *in vitro*

### Chapter 3 Investigation of microvascular formation using a microfluidic chip

anastomosis formation were monitored using GFP-HUVECs. Finally, the detailed structure of vascular anastomoses was observed to confirm continuous lumens.

## 3-2 Experimental design

### Aim

In chapter 2, sinusoid-scale microvessels were constructed in a decellularized liver, while HV networks remained as bare ECM fibers due to the absence of ECs. Therefore, this chapter was designed to construct microvascular networks including vascular networks, since vascular anastomosis formation is an important step in construction of arterio-venous networks (Cheng *et al.*, 2011; Song and Munn, 2011; Song *et al.*, 2012). In addition, experiments were conducted using microfluidic chips to make it easier to understand vascular formation process and reduce the number of animal sacrifice.

### Approaches

Microfluidic chips were designed to mimic a microenvironment of a hepatic lobule in a decellularized liver, where HUVECs were present in the PV and HV divided by a fibrillar matrix (500–1000  $\mu\text{m}$  width) (Fig. 3-1, upper panel). Microfluidic chips were fabricated with PDMS, which included three parallel channels. The central channel was filled with fibrin-collagen gel, resulting a gel region sandwiched by two channels for cell seeding. HUVECs were seeded in both channels to form vascular anastomoses in the gel region (Fig. 3-1, lower panel).

There is growing evidence that mechanical factors (e.g., FSS and interstitial flow) chemical factors (e.g., surface coating, chemical gradient, and coculture system) can regulate *in vitro* vascular formation (Shamloo *et al.*, 2012; McFadden *et al.*, 2013; Han *et al.*, 2015; Yamamoto *et al.*, 2019; Galie *et al.*, 2014; Abe *et al.*, 2019; Hsu *et al.*, 2013). In this chapter, chemical gradient and coculture system were utilized to form vascular anastomoses, because flow conditions sometimes result in complex system affected by a lot of factors such as convection and diffusion (Hsu *et al.*, 2013; Abe *et al.*, 2019).

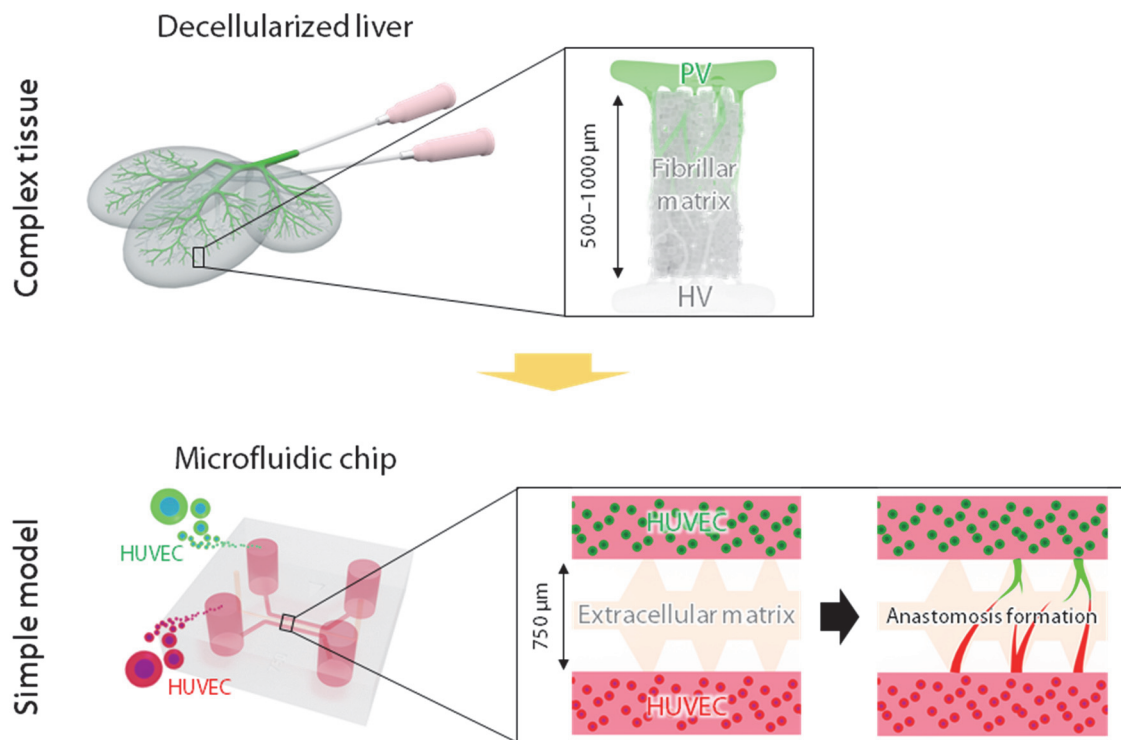


**Fig. 3-1 Experimental design for construction of microvascular networks.** In chapter 2, portal vein networks and sinusoid-scale microvessels were constructed in fibrillar matrix of a decellularized liver (upper panel). In chapter 3, a microfluidic system was employed as a simple *in vitro* model to investigate how to form microvascular networks (lower panel).

### 3-3 Materials and methods

#### 3-3-1 Fabrication of microfluidic chips

The fabrication process of microfluidic chips used in this study was described previously (Shin *et al.*, 2012). Briefly, master molds of microfluidic chips were produced by UV-photolithography techniques, and the molds were copied to polydimethylsiloxane (PDMS; Sylgard 184, Dow Corning, Midland, MI, USA). The PDMS chips were bonded to cover-glasses after exposure to air plasma, which resulted in formation of microchannels. The microchannels were coated with 1 mg/ml poly-D-lysine solution (Sigma-Aldrich) and rinsed twice with sterile distilled water. The coated microfluidic chips were dried for more than 24 hours until use.

A rat-tail type I collagen solution (Corning, NY, USA) was adjusted to 4 mg/ml and pH 7.4 with 0.5 N sodium hydroxide (Wako, Osaka, Japan). Similarly, fibrinogen (Sigma-Aldrich) was dissolved in PBS to 4 mg/ml. The fibrinogen and collagen solutions were then mixed at a 9:1 ratio. Finally, the fibrinogen-collagen solution was mixed with 10 unit/ml thrombin solution (Sigma-Aldrich) at a 10:1 ratio and injected into the gel channel of microfluidic chips (750  $\mu\text{m}$  width and 150  $\mu\text{m}$  height) (Fig. 3-2A, B). Microfluidic chips were then placed in a humidified 5%  $\text{CO}_2$  incubator at 37°C for 30 min to promote gelation. Finally, lateral microchannels were filled with cell culture medium and the chips were kept in the incubator until use.

#### 3-3-2 Cell preparation and *in vitro* formation of vascular anastomoses

HUVECs, GFP-HUVECs, and MSCs were cultured to form vascular anastomosis. HUVECs (Lonza) and GFP-HUVECs (Angio-Proteomie) were obtained commercially and cultured in endothelial growth medium-2 (EGM-2; Lonza) in a 5%  $\text{CO}_2$  incubator at 37°C. HUVECs and GFP-HUVECs were expanded in collagen-coated cell culture dishes and cells at passages 4–7 were used for experiments.

Isolation of MSCs from human bone marrow was previously described using the

LNGFR (CD271) and THY-1 (CD90) surface markers (Mabuchi *et al.*, 2013). The isolated MSCs were expanded in MSC growth medium: Dulbecco's modified Eagle's medium with low glucose (Invitrogen Life Technologies) supplemented with 20% FBS, 20 ng/ml bFGF, and 1% antibiotic-antimycotic (Gibco). Cells were then cultured in a humidified 5% CO<sub>2</sub> incubator at 37°C. All experiments were performed with cells at passages 5–7.

HUVECs were dissociated from cell culture dishes using trypsin-EDTA (Thermo Fisher Scientific) and suspended in EGM-2 at a concentration of  $1.0 \times 10^6$  cells/ml. MSCs were similarly detached using trypsin-EDTA and suspended in DMEM (Gibco) supplemented with 20% FBS (MSC medium) at a concentration of  $1.0 \times 10^6$  cells/ml. First, 10  $\mu$ l cell suspension of HUVECs were seeded in a microchannel through an outlet of the microchannel. Microfluidic chips were then tilted to promote cell attachment to the surface of the gel scaffold. Similarly, the other microchannel was filled with 10  $\mu$ l cell suspension of HUVECs and MSCs in total at ratios of 2:8, 5:5, and 8:2 (Fig. 3-3A, B). Subsequently, microfluidic chips were incubated for 30 min in a humidified 5% CO<sub>2</sub> incubator at 37°C to allow cell attachment. Finally, reservoirs of microchannels were replenished with a 1:1 mixture of EGM-2 and MSC medium supplemented with 10 ng/ml VEGF (R&D Systems, Minneapolis, MN, USA) and 15 ng/ml bFGF. The culture medium was replaced daily, and cells were cultured until day 10. During this culture period, HUVECs extended vascular networks from both microchannels and finally formed vascular anastomosis in the gel region (Fig. 3-3C, D).

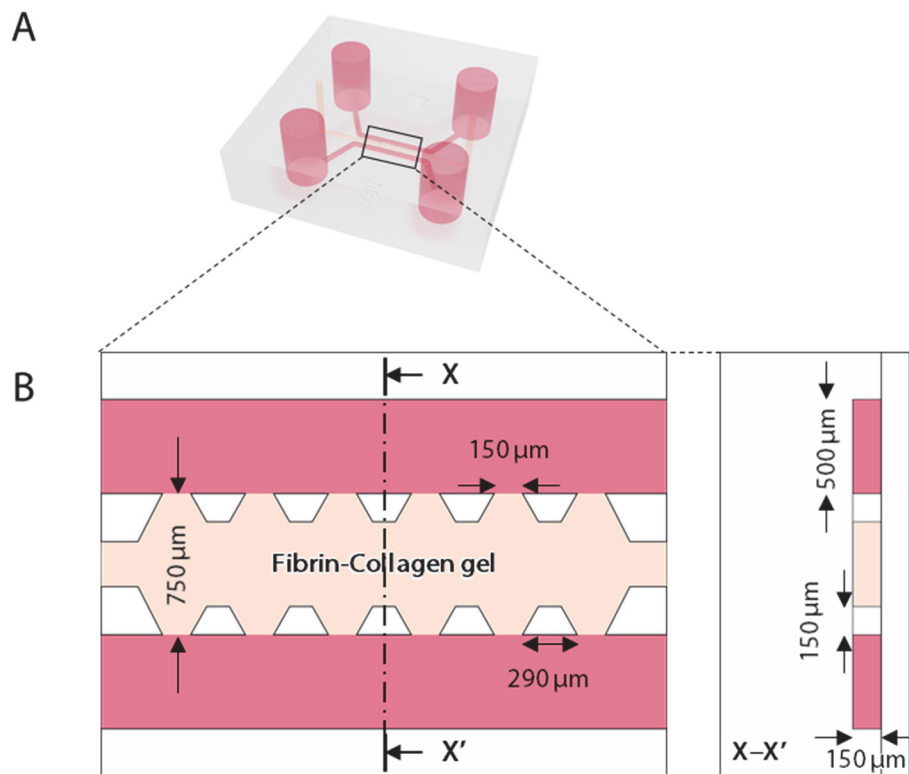


**Fig. 3-2 Schematic illustrations of a microfluidic chip.** (A, B) A schematic illustration of a microfluidic chip (A) and a gel region (B). Section X–X' represents cross-sectional view of microchannels.

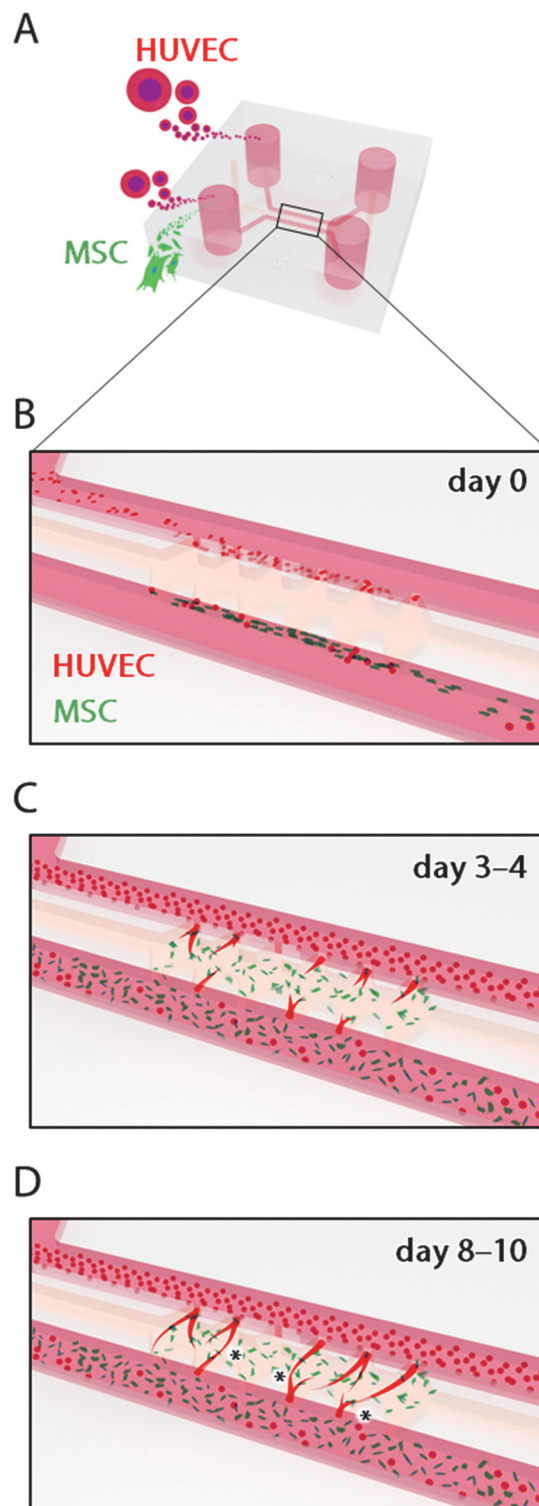


**Fig. 3-3 Schematic illustrations of an *in vitro* vascular anastomosis model in a microfluidic chip.** (A) A schematic illustration of a microfluidic chip. (B) Human umbilical vein endothelial cells (HUVECs, red) and mesenchymal stem cells (MSCs,

green) were seeded into microchannels and attached to the surfaces of the gel scaffold. (C) MSCs migrated into the gel and induced the formation of vascular sprouts. (D) Finally, microvessels extended from both sides of the gel contacted each other and formed vascular anastomosis (asterisks).

### 3-3-3 Immunofluorescent staining and imaging of vasculatures

A rabbit anti-CD146 antibody and a mouse anti- $\alpha$ SMA antibody (Sigma-Aldrich) were used as primary antibodies labeling HUVECs and pericyte-like perivascular cells, respectively (Yamamoto *et al.*, 2019). Alexa Fluor 594-conjugated anti-rabbit IgG (Invitrogen Life Technologies) and Alexa Fluor 488-conjugated anti-mouse IgG (Invitrogen Life Technologies) were used as secondary antibodies.

Samples were fixed in 4% PFA for 15 min at 25°C and permeabilized with 0.1% Triton X-100 for 5 min. After rinsing with PBS, samples were treated with BlockAce (DS Pharma Biomedical) for 1 h to inhibit non-specific staining. Samples were then incubated overnight with primary antibodies, followed by incubation with secondary antibodies. Thereafter, samples were incubated with DAPI (Invitrogen Life Technologies) for staining cell nuclei.

3D fluorescence images were obtained using a confocal laser-scanning microscope (LSM700; Carl Zeiss). The 2D projected images were generated from 3D fluorescence images using maximum intensity Z-projection in ImageJ (National Institutes of Health).

### 3-3-4 Quantitative analysis of vascular networks

Geometrical characteristics of vascular networks (e.g., vascular distance, total length, and number of anastomoses) were analyzed using 2D phase-contrast images or projected images of 3D confocal data generated by ImageJ. Maximum vascular distance was defined as the distance between the gel surface and the vascular tip. The maximum distance of vascular networks was measured in each region. This distance was measured using a straight-line tool in ImageJ. Total length of vascular networks was measured by multiple lines that were drawn along the long axis of the vessel using the straight-line tool. Vascular anastomosis was defined by a continuous lumen structure between microvessels, which was confirmed by cross-sectional images of vascular networks. The number of vascular anastomoses was counted manually.

### 3-3-5 Diffusion simulation of VEGF in HUVEC-MSK coculture

The concentration of VEGF in the hydrogel scaffold was calculated by Fick's second law using a finite element simulation software, COMSOL Multiphysics 5.2a (COMSOL Inc., Burlington, MA, USA). To create 3D models of microfluidic chips, gel channels, medium channels, and medium ports were modeled in COMSOL. VEGF distributions were calculated based on a previous study (Jeong *et al.*, 2011), using a diffusion coefficient of VEGF in the medium of  $2.5 \times 10^{-9} \text{ m}^2/\text{s}$ , and that in the gel scaffold of  $6.6 \times 10^{-11} \text{ m}^2/\text{s}$  (Helm *et al.*, 2005; Sudo *et al.*, 2009), respectively. The consumption rate of VEGF in HUVECs in microchannels was assumed to be 20 ng/day/ $10^6$  cells (Zandstra *et al.*, 1997), and VEGF secretion from MSCs in microchannels was assumed to be 24 ng/day/ $10^6$  cells (Beckermann *et al.*, 2008). Colormaps of VEGF distribution at 24 h were obtained.

### 3-3-6 Live-cell imaging of *in vitro* vascular anastomosis formation

To monitor the formation of vascular anastomosis, GFP-HUVECs were cultured with MSCs in a microfluidic chip. GFP-HUVECs were seeded in a microchannel, while both GFP-HUVECs and MSCs were seeded in the other channel. The cell culture medium was replenished daily, and fluorescence images were taken every other day until day 10 to monitor the process of anastomosis formation using a fluorescence microscope (Axio Observer Z1; Carl Zeiss).

### 3-3-7 Observation of the detailed structure of *in vitro* vascular anastomoses

Z-stack fluorescence images were acquired with 40× objective lens (EC Plan-Neofluar, NA 1.30; Carl Zeiss) to examine the detailed structure of vascular anastomosis between HUVECs and GFP-HUVECs using a confocal laser-scanning microscope (LSM700). Projected and cross-sectional images were generated from the z-stack

fluorescence images using maximum intensity Z-projection and orthogonal views in ImageJ, respectively. To demonstrate vascular anastomosis, 3D reconstruction images were generated from the z-stack fluorescence images by Imaris 7.7.0 software (Bitplane, Badenerstrasse, Zurich, Switzerland).

#### 3-3-8 Statistical analysis

Experiments were repeated several times to confirm repeatability of the results. Data are presented as means  $\pm$  standard error (SE). Student's t test was used to test for differences between 2 groups and Tukey's multiple comparison test was also used to test for differences among  $> 3$  groups, which were considered statistically significant at  $P < 0.05$ . Statistical analyses were performed using SPSS (IBM).

### 3-4 Results

#### 3-4-1 Vascular formation was inhibited in HUVEC-HUVEC monoculture

First, HUVECs were cultured in one of two microchannels to confirm the ability of vascular formation. In this “HUVEC-alone” condition, HUVECs attached to one side of the gel scaffold and formed vascular sprouts. These vascular sprouts gradually extended across the gel scaffold and finally developed into vascular networks. The constructed vessels reached to the other microchannel across the gel scaffold of 750  $\mu\text{m}$  width by day 10 (Fig. 3-4A). Next, HUVECs were cultured in both microchannels to assess whether HUVECs form vascular anastomosis *in vitro*. In this “HUVEC-HUVEC” condition, HUVECs attached to both sides of the gel scaffold. In contrast to the HUVEC-alone condition, vascular sprouts were hardly observed, at least by day 10 (Fig. 3-4B). Although some sprouts were formed, they were not stable and eventually regressed (Fig. 3-4B, arrowheads). Quantitative analysis was performed focusing on maximum vascular distance from the gel interface, which showed that the elongation of the constructed vessels was significantly inhibited in the HUVEC-HUVEC condition, compared to the HUVEC-alone condition (Fig. 3-4C, D). Specifically, maximum vascular distance was  $430 \pm 46.6 \mu\text{m}$  in the HUVEC-alone condition, while this figure was  $99.9 \pm 20.8 \mu\text{m}$  in the HUVEC-HUVEC condition on day 10.

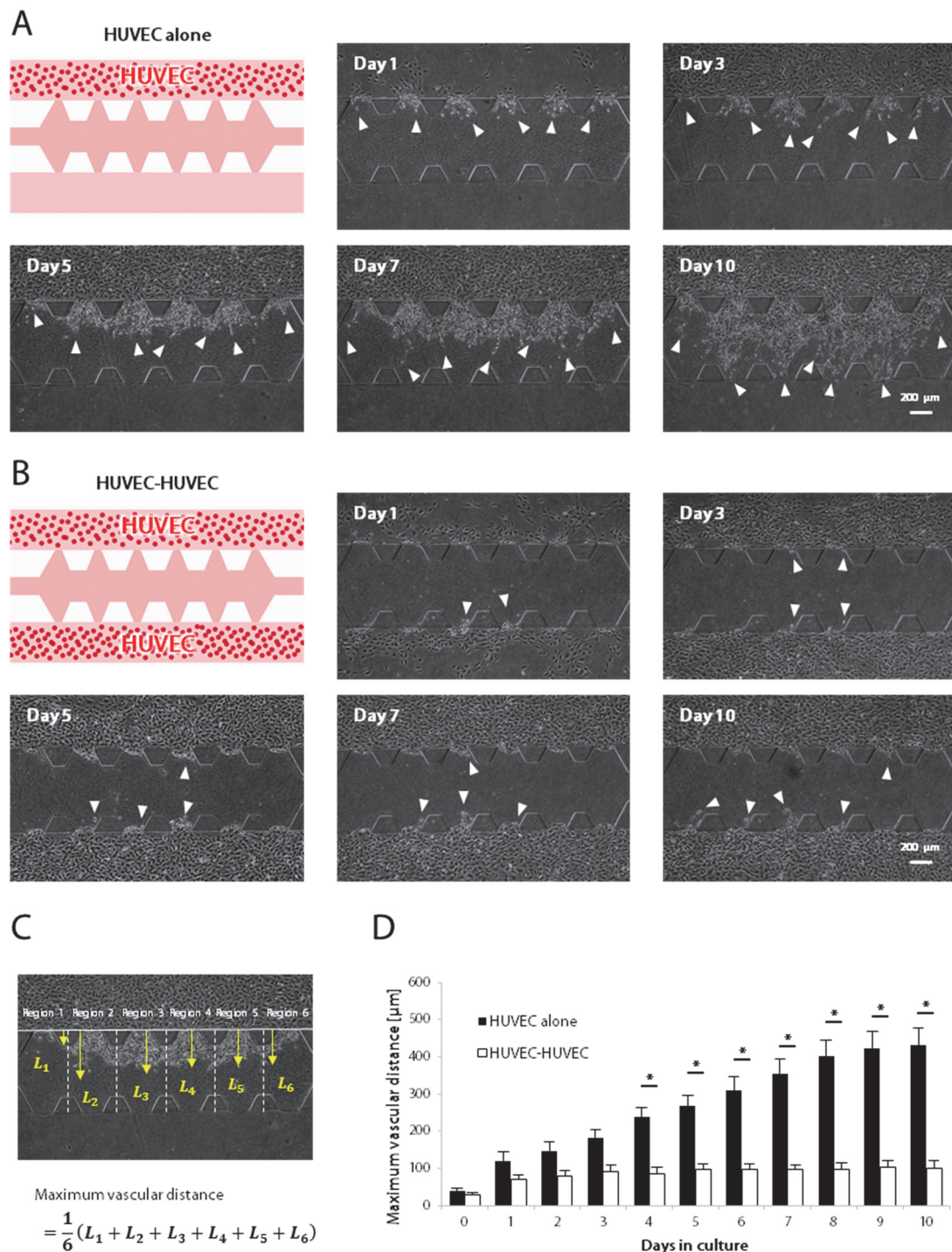


**Fig. 3-4 The processes of vascular formation in HUVEC monoculture.** (A) A schematic illustration of the “HUVEC-alone” condition. HUVECs were seeded in a microchannel and attached to one side of the gel scaffold. HUVECs formed vascular sprouts on day 1, which developed into networks extending into the entire gel by day 10.

### Chapter 3 Investigation of microvascular formation using a microfluidic chip

Arrowheads indicate tips of constructed vessels. (B) A schematic illustration of the “HUVEC-HUVEC” condition. HUVECs were seeded in both microchannels and attached to both sides of the gel scaffold. Although HUVECs formed some vascular sprouts, these were not stable and eventually regressed (arrowheads). (C) A schematic diagram for the measurement of maximum vascular distance. (D) Quantitative analysis of maximum vascular distance. Scale bars: 200  $\mu\text{m}$  (A), (B). \* $P < 0.05$  (N = 3, n = 11).

To investigate this inhibitory vascular formation in the HUVEC-HUVEC condition, computational simulation was performed focusing on VEGF concentration, because establishment of a VEGF gradient is known as an important factor to regulate vascular formation. In the initial condition, there was no VEGF gradient because both microchannels were filled with culture medium containing 10 ng/ml VEGF (data not shown). However, HUVECs consumed VEGF, resulting in changes in VEGF concentration. In the present study, HUVEC monoculture was performed without flow condition. Thus, concentrations of VEGF varied depending on the VEGF consumption rate of cells in microchannels due to the absence of fresh medium perfusion. The simulation results indicated that a VEGF gradient was formed by 24 h in the HUVEC-alone condition (Fig. 3-5A), while a flat distribution was obtained at 24 h in the HUVEC-HUVEC condition (Fig. 3-5B). These results indicated that VEGF distribution varied depending on initial cell distribution.

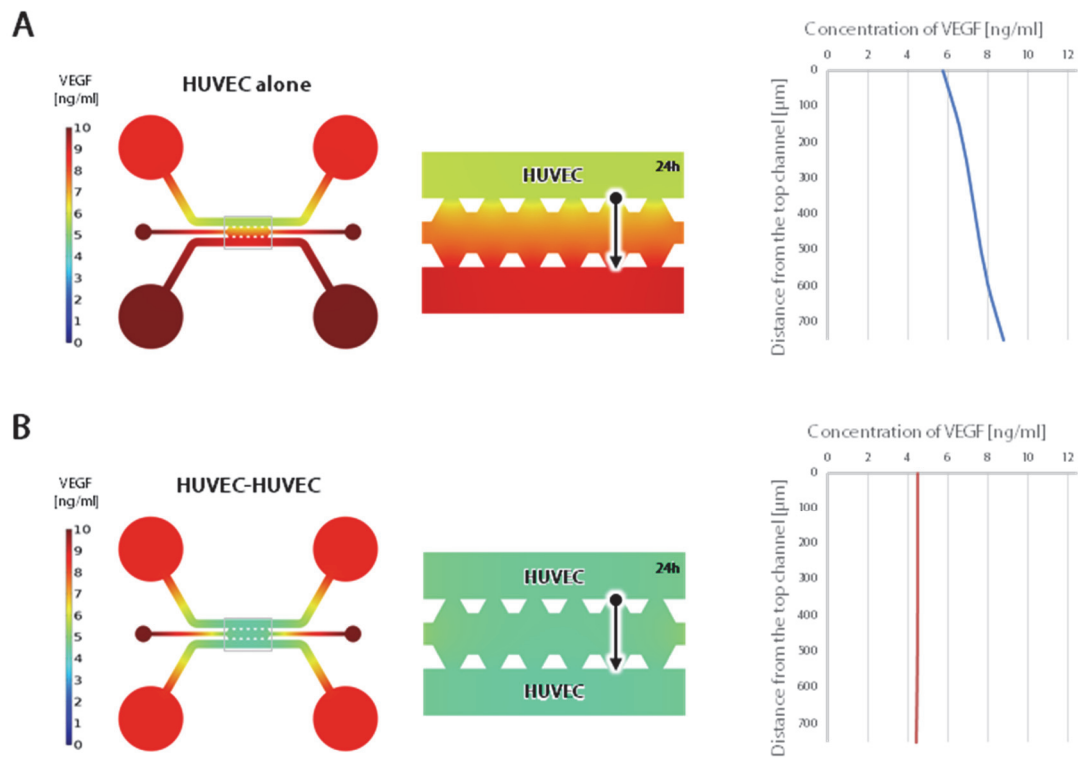


**Fig. 3-5 Computational simulation of VEGF gradients in HUVEC monoculture.** (A) The overall and enlarged views of colormap show the distribution of VEGF in the “HUVEC-alone” condition at 24 h of culture. The concentration gradient of VEGF was maintained across the gel scaffold. (B) The overall and enlarged views of colormap show the distribution of VEGF in the “HUVEC-HUVEC” condition at 24 h. No VEGF gradient was observed in the gel scaffold.

#### 3-4-2 HUVEC-MSC coculture promoted formation of *in vitro* vascular anastomoses

Recently, it was reported that MSCs promoted formation of microvascular networks in a microfluidic chip (Yamamoto *et al.*, 2019). Thus, HUVEC-MSC coculture was performed to support vascular anastomosis formation in a microfluidic chip. Specifically, MSCs were added to the HUVEC-HUVEC culture condition to induce angiogenesis. Moreover, a series of HUVEC:MSC ratios were tested in HUVEC-MSC coculture (Fig. 3-6A). Immunofluorescence images showed that vascular formation was dependent on HUVEC:MSC ratios. At a HUVEC:MSC ratio of 2:8, vascular networks were extended from both microchannels and they formed vascular anastomoses by day 10 (Fig. 3-6B, asterisks). Furthermore, enlarged images showed that these vascular networks were covered by perivascular cells, which were positive for a pericyte marker,  $\alpha$ SMA (Fig. 3-6B, (i, ii)). In contrast, vascular anastomoses were less frequently observed at HUVEC:MSC ratios of 5:5 and 8:2 (Fig. 3-6C, D).

Quantitative analysis showed that both maximum vascular distance and total length of vascular networks were significantly greater at the HUVEC:MSC ratio of 2:8, compared to the other ratios (Fig. 3-6E, F). Moreover, the number of vascular anastomoses was significantly increased at the HUVEC:MSC ratio of 2:8, which was > 3-times greater than the other ratios (Fig. 3-6G).

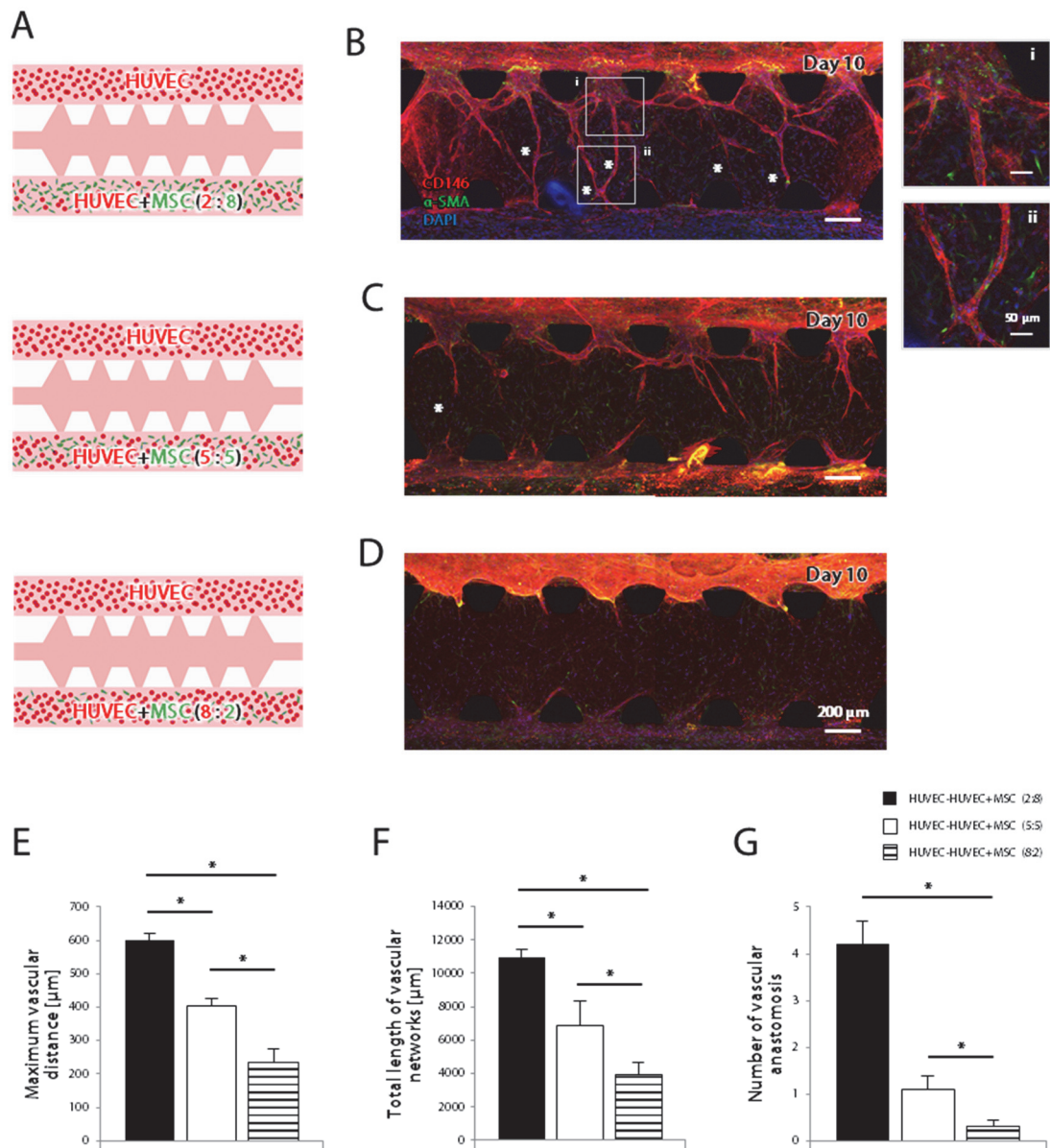


**Fig. 3-6 Comparison of *in vitro* vascular anastomosis models in HUVEC-MSC coculture at different HUVEC:MSC ratios.** (A) Schematic illustrations of cell culture conditions. HUVECs were seeded in microchannels, while both HUVECs and MSCs were seeded in the other microchannels at different HUVEC:MSC ratios (2:8, 5:5, 8:2). (B–D) Formation of vascular anastomosis in microfluidic chips. The fluorescence images represent the formation of vascular networks (CD146) covered by perivascular cells ( $\alpha$ SMA) on day 10. Cell nuclei were counterstained with DAPI. Asterisks indicate vascular anastomosis. Enlarged images (i) and (ii) correspond to the boxes (i) and (ii) in

B, respectively. (E–G) Quantitative analyses of maximum vascular distance (E), total length of vascular networks (F), and the number of vascular anastomoses (G) on day 10. Scale bars, 200  $\mu\text{m}$  (B–D) and 50  $\mu\text{m}$  (i, ii). Data are shown as mean  $\pm$  SE (N = 3, n = 10). \* $P < 0.05$ .

Computational simulation of VEGF concentrations in the HUVEC-MSK coculture were also performed at the HUVEC:MSK ratios of 2:8, 5:5, and 8:2 in static culture. Similar to the HUVEC monoculture, there was no VEGF gradient in the initial condition because both microchannels were filled with culture medium containing 10 ng/ml VEGF (data not shown). However, HUVECs consumed VEGF while MSKs produced VEGF, resulting in changes in local VEGF concentration near cells, depending on HUVEC:MSK ratios (Beckermann *et al.*, 2008). The simulation results showed that VEGF gradients were formed by 24 h under all conditions (Fig. 3-7A–C). Notably, the steepest VEGF gradient was detected at the HUVEC:MSK ratio of 2:8. This coculture condition was used for anastomosis formation in the following experiments.

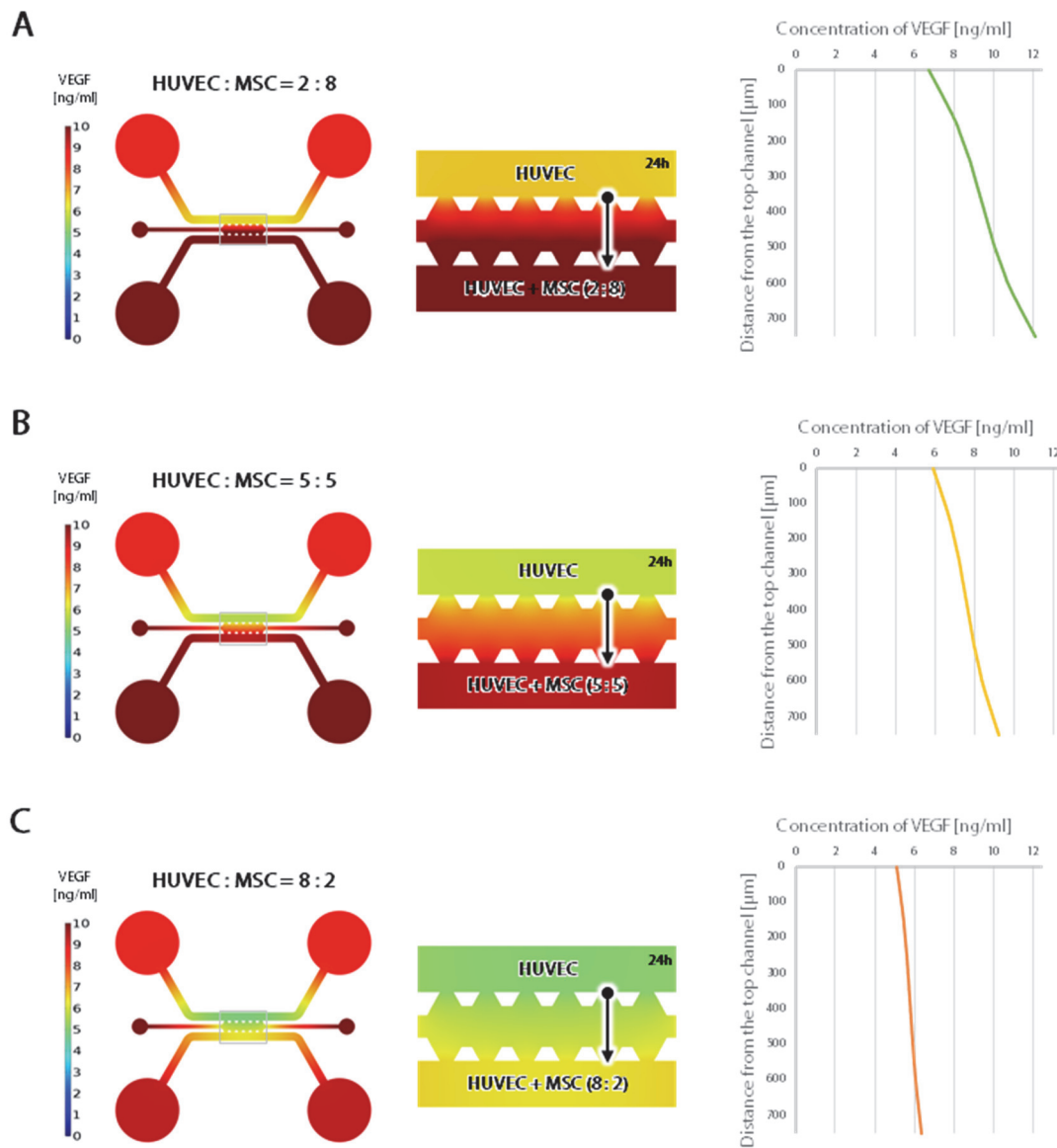


**Fig. 3-7 Computational simulation of VEGF gradients in HUVEC-MSC coculture at different HUVEC:MSC ratios.** (A–C) The overall and enlarged views of colormaps and graphs show the distribution of VEGF at 24 h in HUVEC-MSC coculture at HUVEC:MSC ratios of 2:8 (A), 5:5 (B), and 8:2 (C).

### 3-4-3 Live-imaging of *in vitro* vascular anastomosis formation

To further investigate the process of vascular anastomosis formation, live-cell imaging of GFP-HUVECs was performed until day 10 in the HUVEC-MSC coculture at the HUVEC:MSC ratio of 2:8. In this experiment, GFP-HUVECs were seeded in a microchannel, while both GFP-HUVECs and MSCs were seeded in the other microchannel (Fig. 3-8A). First, vascular sprouts were formed on day 2, which extended from the side of HUVECs alone (Fig. 3-8B, arrowheads). These vascular sprouts gradually extended across the gel scaffold, while vascular sprouts also extended from the side of HUVECs and MSCs by day 4 (Fig. 3-8C, arrowheads). These vascular sprouts extended from both microchannels and continued to extend. Vascular interconnections between tips of these vessels were formed during days 6–8 (Fig. 3-8D, E, asterisks). Finally, vascular anastomoses were developed in this microfluidic chip by day 10 (Fig. 3-8F, asterisks).

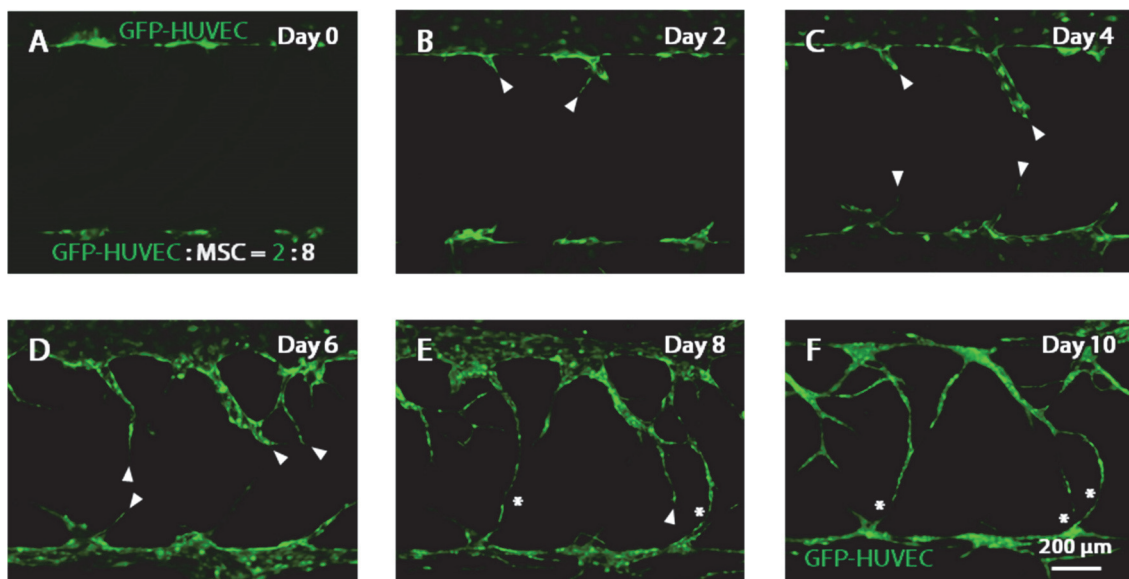


**Fig. 3-8 Live-cell imaging of GFP-HUVECs during *in vitro* vascular anastomosis formation.** (A) GFP-HUVECs were seeded a in microchannel, while both GFP-HUVECs and MSCs were seeded in the other microchannel at a HUVEC:MSC ratio of 2:8. (B–D) GFP-HUVECs formed vascular sprouts by day 4 from both sides of the microchannel and then extended vascular networks on day 6. Arrowheads indicate the tips of vascular networks. (E–F) Microvessels extended from different microchannels contacted each other and formed vascular anastomoses (asterisks) during days 8–10. Scale bar, 200  $\mu\text{m}$ .

#### 3-4-4 Investigation of the detailed structure of *in vitro* vascular anastomosis

To investigate the detailed structure of vascular anastomosis, vessels were stained and three-dimensionally observed by confocal microscopy. In this experiment, GFP-HUVECs were seeded in one of the two microchannels to distinguish vessels extended from each microchannel, while both HUVECs and MSCs were seeded in the other microchannel at a HUVEC:MSC ratio of 2:8 (Fig. 3-9A). Vascular structures were fixed on day 10 and stained for CD146, an endothelial marker. Immunofluorescence imaging showed that the upper part of the vessel was positive for both CD146 and GFP (Fig. 3-9B, i–ii), while the lower part of the vessel was positive for CD146 (Fig. 3-9B, iii). This represents vascular anastomosis because the upper part of the vessel was extended from the microchannel of GFP-HUVECs alone while the lower part of that was from the microchannel of both HUVECs and MSCs. Corresponding 3D reconstruction images indicated that vascular anastomosis with continuous lumens was formed (Fig. 3-9C–E).

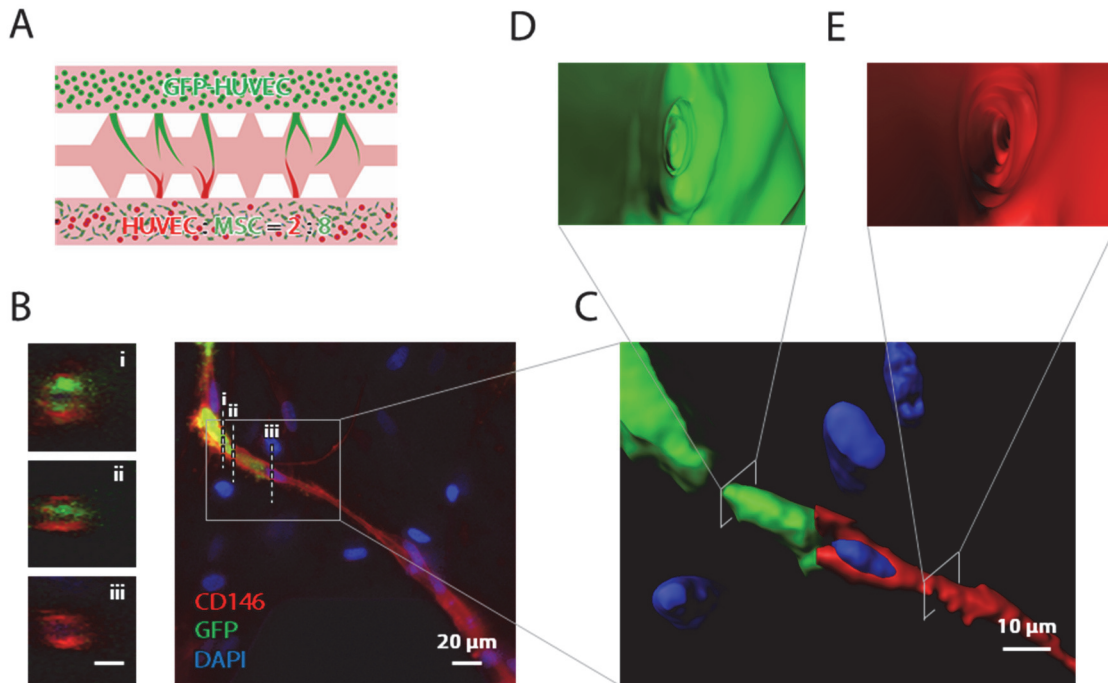


**Fig. 3-9 A detailed structure of vascular anastomosis between HUVECs and GFP-HUVECs.** (A) A schematic illustration of vascular anastomosis between HUVECs and GFP-HUVECs. GFP-HUVECs were seeded in a microchannel, while both HUVECs and MSCs were seeded in the other microchannel at a HUVEC:MSC ratio of 2:8. (B) A projected confocal image showing vascular anastomosis labeled with CD146 (HUVECs) and GFP (GFP-HUVECs). Cross-sectional images correspond to lines i–iii. (C–E) 3D reconstruction images of vascular anastomosis (C). 3D reconstructed images show that both GFP-HUVECs and HUVECs formed continuous lumens (D, E). Scale bars, 20 μm (B) and 10 μm (i–iii, C).

### 3-4-5 Pro-angiogenic effects of VEGF gradient in HUVEC-HUVEC monoculture

Finally, effects of VEGF gradient on vascular formation was tested in HUVEC-HUVEC monoculture to investigate whether VEGF gradient can induce the formation of vascular anastomosis in this model. To generate a VEGF gradient across the gel scaffold, one microchannel was filled with culture medium containing 50 ng/ml VEGF, while the other microchannel was filled with normal culture medium containing 10 ng/ml VEGF. In this condition, HUVECs formed some vascular sprouts, while only a few vascular sprouts were observed without VEGF gradient (Fig. 3-10A, B). Quantitative analysis revealed that the VEGF gradient significantly promoted vascular formation in the HUVEC-HUVEC condition. The maximum vascular distance was approximately 2.5-times greater in the presence of VEGF gradient than that without VEGF gradient (Fig. 3-10C). However, vascular anastomoses were not formed even in the presence of VEGF gradient.

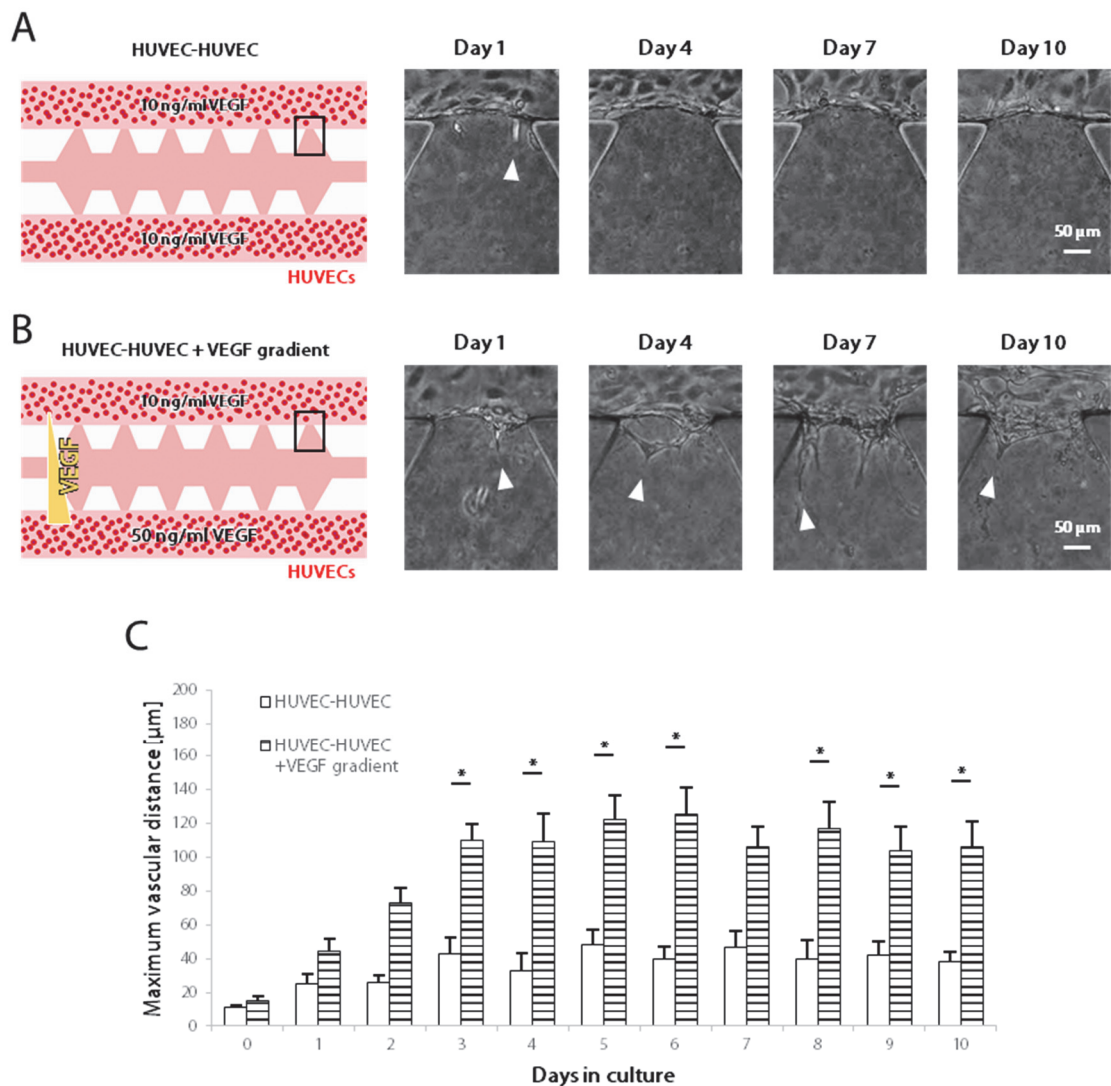


**Fig. 3-10 HUVEC-HUVEC monoculture with VEGF gradient.** (A) A schematic illustration and corresponding phase-contrast images of the “HUVEC-HUVEC” condition. An arrowhead indicates a vascular sprout. (B) A schematic illustration and corresponding phase-contrast images of the “HUVEC-HUVEC + VEGF gradient” condition. Arrowheads indicate vascular sprouts. (C) Quantitative analysis of maximum vascular distance. Scale bars, 50  $\mu\text{m}$  (A), (B). Data are shown as mean  $\pm$  SE (N = 2, n = 8). \* $p < 0.05$ .

### 3-5 Discussion

#### 3-5-1 Inhibition of vascular sprouting in HUVEC-HUVEC monoculture

In the present experiments, HUVEC monoculture was performed to form vascular anastomosis in a microfluidic chip. Contrary to expectations, vascular formation was significantly inhibited when HUVECs were seeded in both microchannels (“HUVEC-HUVEC” condition). This can be explained by VEGF gradient profiles in “HUVEC-alone” and “HUVEC-HUVEC” conditions. Simulation results indicated that a VEGF gradient across the gel scaffold was maintained in the “HUVEC-alone” condition, whereas it is not maintained in the “HUVEC-HUVEC” condition because HUVECs consumed VEGF supplemented in the medium in both microchannels. Moreover, VEGF gradient enhanced vascular formation in the HUVEC-HUVEC condition. These results suggest that VEGF gradient is one of the most important factors for regulating angiogenesis.

It is well-known that chemical gradients (e.g., VEGF and S1P) facilitate EC migration and vascular sprouting (Liu *et al.*, 2007; van Duinen *et al.*, 2019). Previous studies have reported that VEGF regulates the formation and orientation of vascular sprouts, which are parallel to the VEGF gradient (Shamloo *et al.*, 2012; Wu *et al.*, 2014). Furthermore, VEGF is also known to regulate EC morphogenesis via induction and activation of specific MMPs, which play important roles in EC migration (Funahashi *et al.*, 2011). However, vascular anastomoses were not formed even in the HUVEC-HUVEC condition in the presence of VEGF gradient. Although VEGF gradient induced angiogenesis, it was not sufficient for the formation of vascular anastomoses in this model. Therefore, HUVEC monoculture was not suitable for formation of vascular anastomosis in this microfluidic chip.

#### 4-3-2 Establishment of an *in vitro* vascular anastomosis model in HUVEC-MSC coculture

As the present study revealed that HUVEC monoculture failed to form vascular anastomosis even in the presence of VEGF gradient, HUVEC-MSC coculture was

utilized to induce vascular sprouting and anastomosis formation. The important findings of the present study are as follows: 1) the amount of MSCs added to the HUVEC monoculture significantly affected vascular formation, 2) greater numbers of vascular anastomoses were formed at a HUVEC:MSC ratio of 2:8, and 3) the addition of MSCs was critical for the formation of vascular anastomosis in this model. Two factors can help to explain these findings.

First, vascular formation was varied by different VEGF gradient profiles due to the different amount of MSCs added to the HUVEC-MSC coculture. As the results confirmed by computational diffusion analysis, the steepest VEGF gradient was maintained at 24 h at a HUVEC:MSC ratio of 2:8. This is consistent with the greatest number of vascular anastomoses at a HUVEC:MSC ratio of 2:8. However, this cannot explain vascular extension from the side of HUVECs and MSCs.

Second, there is a possibility that vascular formation was promoted by other secreted or juxtacrine factors of MSCs (Nassiri and Rahbarghazi, 2014). There are many evidences that MSCs promote vascular formation (McFadden *et al.*, 2013; Jeon *et al.*, 2014), which may induce the formation of vascular networks in a microfluidic chip. It was also demonstrated that HUVEC-MSC coculture promoted EC sprouting and migration along MSC networks in the gel scaffold (Yamamoto *et al.*, 2019). These findings suggested that multiple factors including VEGF gradient were involved in the formation of vascular networks and anastomoses in this model. In particular, HUVECs might extend vascular networks in response to a local gradient of chemical factors secreted by the MSCs distributed in the gel scaffold. This is consistent with the results that microvessels were extended from both microchannels, and there was subsequent formation of vascular contact between microvessels. In addition, other groups reported that ECs at the tips of adjacent sprouts would align ECM between them by a traction-mediated effect, which can also facilitate vascular contact and anastomosis formation (Vernon and Sage, 1995).

The addition of MSCs is also critical to mimic *in vivo* vascular anastomosis. Vascular anastomosis in this study was constructed between microvessels formed in HUVEC-MSC culture. The results demonstrated the construction of microvessels covered by MSC-derived perivascular cells, which was similar to *in vivo* microvessels because *in vivo* vascular anastomosis is regulated by not only EC but also perivascular cells (Hirschi and D'Amore, 1996; Ribatti *et al.*, 2011). Therefore, this culture model can recapitulate *in vivo* vascular anastomosis between engineered and host vessels.

### 3-5-3 Comparison of *in vitro* and *in vivo* anastomosis formation

As an *in vitro* model of vascular anastomosis was established in this study, the processes and detailed structures of anastomoses were investigated by live-cell imaging of GFP-HUVECs. Previous studies have reported the processes of vascular anastomosis formation during embryonic development using animal models (e.g., zebrafish). These studies described that a multistep process is involved in vascular anastomosis, including EC migration, vascular contact, and luminal formation (Herwig *et al.*, 2011; Lenard *et al.*, 2013). Specifically, vascular endothelial cadherin protein was shown to play critical roles in the early steps of vascular anastomosis, such as recognition of tip cells, contact formation, and lumen formation. Furthermore, it was confirmed that vascular anastomosis was formed through EC migration and vascular contact, finally resulting in the formation of continuous lumens. In addition, other groups reported that *in vivo* vascular anastomosis formation between arterial and venous vessels in zebrafish is regulated by a chemokine receptor, *cxcr4a*, and its ligand, *cxcl12b* (Bussmann *et al.*, 2011). This anastomosis model may provide detailed insight to further elucidate mechanism of *in vivo* anastomosis formation. Additional investigation will be needed to evaluate vascular functions after anastomosis generation, such as barrier functions and antithrombotic functions.

### 3-6 Summary

In this chapter, an *in vitro* vascular anastomosis model was established using microfluidic chips by regulating chemical factors. First, it was found that “HUVEC-HUVEC” condition failed to form vascular networks, while HUVEC-MSC coculture successfully promoted vascular anastomosis formation. Moreover, computational simulation suggested that local VEGF gradients play important roles in formation of vascular networks and anastomoses. However, since HUVECs failed to form vascular anastomoses in HUVEC-HUVEC conditions even in the presence of VEGF gradient, which indicated that the addition of MSCs was critical for vascular anastomoses in this culture model. This anastomosis model will provide useful information for the development of arterio-venous networks such as PV-sinusoid-HV networks in a decellularized liver.

In this chapter, microvascular networks including vascular anastomoses were constructed in a microfluidic chip by heterotypic cell–cell interaction and chemical factors (Fig. 3-11, left panel). Hence, the following chapter focuses on construction of functional organ-scale vascular networks with findings obtained in chapters 2 and 3 (Fig. 3-11, right panel).

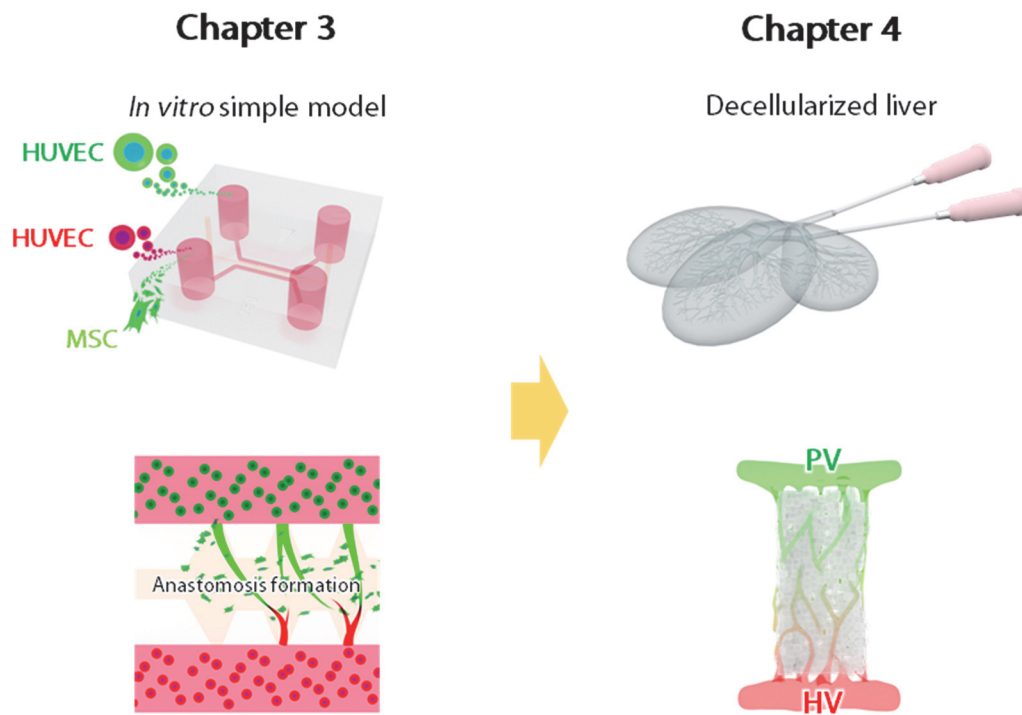


**Fig. 3-11 Strategic direction for construction of organ-scale vascular networks.** In chapter 3, microvascular networks were constructed in HUVEC-MSC coculture using a microfluidic chip. Hence, in chapter 4, a decellularized liver was used again to construct organ-scale vascular networks with findings obtained in chapters 2 and 3.

## **Chapter 4 Construction of functional vascular networks in a decellularized liver**

### 4-1 Introduction

Liver transplantation is only treatment for patients with end-stage liver diseases, because living livers cannot be replaced by artificial devices due to the complexity of liver functions. Although liver support strategies such as hepatocyte transplantation and bioartificial livers (e.g., MARS) have been widely developed as alternatives to conventional liver transplantation, artificial liver support systems cannot replace liver functions adequately and these systems have been used as bridge-to-transplant to gain time (Fox *et al.*, 1998; Palakkan *et al.*, 2013; Sauer *et al.*, 2004). Moreover, recent trends have focused on development of *in vitro* hepatic tissue constructs using biomaterials such as cells, scaffolds, and growth factors (Kasuya *et al.*, 2012, 2015; Ajoudanian *et al.*, 2019; Damania *et al.*, 2014; Takebe *et al.*, 2013; Koike *et al.*, 2019; Sakai *et al.*, 2015) in accordance with the principle of tissue engineering (Langer and Vacanti, 1993). However, these techniques have not been adopted in clinical use due to the small size of hepatic tissues-engineered constructs.

Recent advances in decellularization technique allowed us to construct organ-scale tissue constructs such as the heart, lungs, kidneys, and liver (Guyette *et al.*, 2014; Uygun *et al.*, 2010). Decellularized organs retain native ECM forming vasculature networks for nutrient and gas transport, and biochemical molecules that may promote cell attachment and tissue regeneration. Especially, Uygun *et al.* (2010) reported that a decellularized liver seeded with hepatocytes supported liver-specific function including albumin secretion, urea synthesis and CYP expression at comparable levels to normal liver. Moreover, Baptista *et al.* (2016) constructed bioengineered liver constructs using HepG2 cells and ECs, which resulted in formation of large clusters of HepG2 cells and EC networks in a decellularized liver. Although decellularized livers have allowed

construction of functional hepatic tissues in terms of liver structure and function, these recellularized livers have not been approved for clinical use due to the problem of clot formation after transplantation, because blood components (e.g., platelets) adhere to bare ECM and subsequently form thrombus (Ruggeri and Mendolicchio, 2007).

To prevent clot formation in recellularized livers, several groups have focused on endothelialization of decellularized liver scaffolds (Ko *et al.*, 2015; Devalliere *et al.*, 2018). For example, Ko *et al.* reported that decellularized liver scaffolds were coated with conjugating anti-endothelial cell antibodies (CD31), which resulted in enhanced coverage of the vascular walls with ECs. Moreover, Hussein *et al.* (2016) demonstrated that a heparin-gelatin coating on the inner surface of blood vessels improved antithrombotic function and EC coverage on vascular wall within decellularized livers, resulting in enhanced liver function after transplantation. Devalliere *et al.* (2018) enhanced endothelialization of decellularized liver scaffolds by conjugating elastin-like peptides grafted with cell binding domain to improve EC attachment on vascular walls. Despite these enormous efforts, complete elimination of platelet adhesion on vascular walls or in a parenchymal region has not been achieved. This may be due to incomplete formation of vascular networks including sinusoids.

Toward further improvement of EC coverage, a perfusion culture system has been established to form whole-liver vascular networks including sinusoid-scale microvessels (< 15  $\mu\text{m}$  in diameter) in a decellularized liver as described in chapter 2 (Watanabe *et al.*, 2019). This study demonstrated that FSS applied to ECs induced formation of sinusoid-scale microvessels in perfusion culture of a decellularized liver. Moreover, a combination of perfusion culture and surface coating with fibronectin significantly promoted the formation of sinusoid-scale microvessels compared to static culture. However, little is known about functions (e.g., antithrombotic) of constructed microvessels.

This chapter focuses on the investigation whether sinusoid-scale microvessels constructed in a decellularized liver have antithrombotic function. The results confirmed

that constructed microvessels reduced platelet deposition in a decellularized liver in perfusion culture with fibronectin coating compared to that in static culture. Moreover, enhanced EC coverage was achieved by route selection for cell seeding as well as mechanical and chemical factors. These findings will provide useful insights to construct a transplantable liver tissue using a decellularized liver in terms of whole-organ vascularization.

## 4-2 Experimental design

### Aim

This chapter was designed to construct functional organ-scale vascular networks including PV, sinusoidal, and HV networks utilizing the findings obtained in chapters 2 and 3.

### Approaches

Chapters 2 and 3 demonstrated that mechanical factors (e.g., FSS) and chemical factors (e.g., surface coating, chemical gradient, and heterotypic cell–cell interaction) can regulate *in vitro* formation of vascular networks including microvessels and vascular anastomoses. Hence, in this chapter, mechanical and chemical factors described in chapters 2 and 3 were utilized to form functional organ-scale vascular networks. Moreover, organ-scale vascular networks were constructed by considering cell seeding route as well as mechanical and chemical factors (Fig. 4-1).

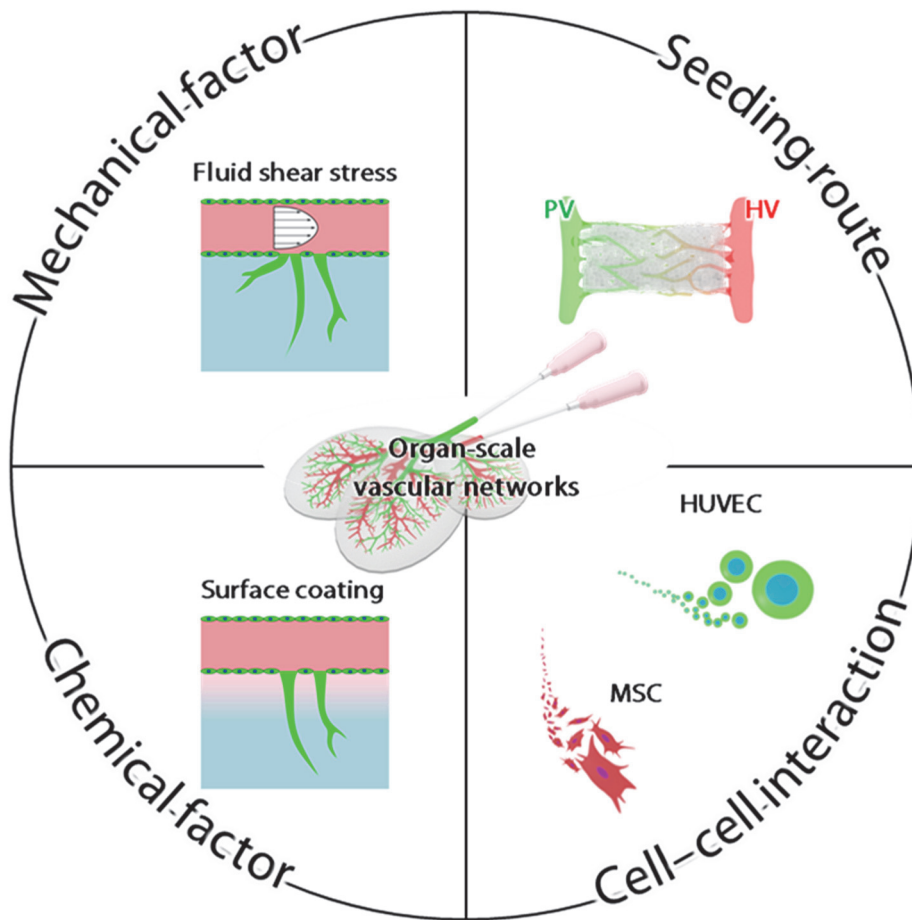


**Fig. 4-1 Experimental design for construction of functional organ-scale vascular networks.** It was demonstrated that mechanical and chemical factors (e.g., FSS and surface coating with fibronectin) were important to construct sinusoid-scale microvessels (chapter 2), while cell seeding route and heterotypic cell–cell interaction were critical for the formation of vascular networks including vascular anastomoses (chapter 3). Hence, in chapter 4, these findings were utilized to construct functional organ-scale vascular networks.

### 4-3 Materials and methods

#### 4-3-1 Animal experiment and liver harvest

Detailed methods and ethical committee approval were described in section 2-3-1. Surgical anesthesia was induced and maintained using 2–4% inhalation isoflurane and abdominal incision was made by scissors. The PV and IVC were cannulated with 20 G cannulas and ligated with silk sutures. Then, the liver was harvested from the rat and frozen at  $-80^{\circ}\text{C}$  for  $> 24$  hours until use.

#### 4-3-2 Decellularization of rat livers

The protocol to obtain a decellularized liver scaffold was described in section 2-3-2. Harvested livers were thawed in a water bath at  $37^{\circ}\text{C}$  and placed in a perfusion-based decellularization system. The cannula inserted in the PV was connected to a peristaltic pump (Cole-Palmer Instrument Co.) and perfused with PBS for 1 hour at a rate of approximately 6 ml/min. Subsequently, the liver was perfused with pre-warmed 0.05% trypsin-0.05% EGTA solution for 2 hours, 0.5% Triton X-100-0.05% EGTA solution for 3–12 hours, and PBS for 1 hour. After the decellularization procedure, RML, LML, and SRL were used for recellularization experiments.

#### 4-3-3 Recellularization of rat livers

Detailed methods were described in section 2-3-3 and 2-3-4. In recellularization experiments, GFP-HUVECs were used for recellularization of vascular networks in decellularized livers. DiI-MSCs and DiI-HUVECs were also prepared for recellularization experiments. HUVECs (Lonza) were labeled with Vybrant™ DiI cell-labeling solution (Thermo Fisher Scientific, Waltham, MA, USA).

To conduct HUVEC-MSC coculture in a decellularized liver, GFP-HUVECs and DiI-labeled MSCs were dissociated from cell culture dishes using trypsin-EDTA (Thermo Fisher Scientific) and suspended in DMEM with low glucose (Gibco) supplemented with

## Chapter 4 Construction of functional vascular networks in a decellularized liver

10% FBS, 1 mM ascorbic acid 2-phosphate, 10 ng/ml bFGF, and 1% antibiotic-antimycotic solution (Gibco) at a concentration of  $1.0 \times 10^6$  cells/ml, respectively. Cell suspensions of  $5.0 \times 10^6$  GFP-HUVECs with different number of MSCs ( $5.0 \times 10^6$ ,  $1.0 \times 10^6$ ,  $5.0 \times 10^5$  cells) were injected into decellularized livers through the PVs. Fluorescence images of constructed EC networks were observed using a fluorescence microscope (Axio Observer Z1; Carl Zeiss).

To perform HUVEC monoculture condition, cell suspensions of  $1.0 \times 10^7$  GFP-HUVECs were seeded into decellularized liver scaffolds through the PV, divided into two injections. In addition, the HV was also used in some experiments to compare cell seeding routes (e.g., PV and HV). After 2 hours of incubation for cell attachment, the culture medium was replenished with fresh medium, and the medium was replenished every other day. Fluorescence images of constructed EC networks were observed using a fluorescence microscope (Axio Observer Z1; Carl Zeiss) on days 0, 2, 4, and 6. Constructed EC networks in the  $2.0 \text{ mm} \times 2.0 \text{ mm}$  ROI were analyzed using ImageJ (National Institutes of Health). The diameter and length of constructed vessels in decellularized livers were measured and histograms of vessel diameter were produced.

To perform perfusion culture, the recellularized liver was placed in a perfusion chamber and the cannula inserted into the PV of the liver was connected to a peristaltic pump after 2 hours of incubation for cell attachment. The recellularized liver was then perfused at 4.7 ml/min through the PV for 2 days, since the perfusion culture condition at 4.7 ml/min was estimated to be an appropriate condition for the formation of sinusoid-scale microvessels in chapter 2. In this perfusion condition,  $\phi 50 \mu\text{m}$  vessels were exposed to approximately 0.5 Pa FSS. Detailed methods and results were described in sections 2-3-4 and 2-4-3.

### 4-3-4 Fibronectin coating of a decellularized liver

To improve microvessel formation, decellularized liver scaffolds were immersed in

50 µg/ml fibronectin solution (Sigma) overnight before liver recellularization.

#### 4-3-5 *Ex vivo* blood perfusion

Whole blood was freshly collected from male Sprague-Dawley rats (Sankyo Labo Service Corporation) and diluted in culture medium at a ratio of 1:5. The diluted blood was infused through the PVs of a decellularized and recellularized livers at a flow rate of 1 ml/min. All samples were then incubated under static condition for 1 hour to promote platelet adhesion on ECM within decellularized livers. After incubation, samples were rinsed with PBS and then fixed in 4% PFA for immunofluorescence staining analysis.

To determine platelet adhesion on ECM, sample sections were stained with a mouse anti-integrin  $\alpha_{IIb}$  antibody (Santa Cruz Biotechnology Inc., Santa Cruz, CA, USA) and Alexa Fluor 647-conjugated mouse anti-goat antibody (Invitrogen Life Technologies, Carlsbad, CA, USA), followed by visualization by confocal microscopy (LSM700; Zeiss).

#### 4-3-6 Statistical analysis

Experiments were repeated several times to confirm repeatability of the results. Data are presented as means  $\pm$  standard deviation (SD). Student's t test was used to test for differences between 2 groups and Tukey's multiple comparison test was also used to test for differences among  $> 3$  groups, which were considered statistically significant at  $P < 0.05$ . Statistical analyses were performed using SPSS (IBM).

## 4-4 Results

### 4-4-1 HUVEC-MSK coculture in a decellularized liver

Based on previous findings that HUVEC-MSK coculture promoted *in vitro* vascular formation, both GFP-HUVECs and MSCs were injected into a decellularized liver through the PV (Fig. 4-2A). The results showed that decellularized livers seeded with GFP-HUVECs and MSCs greatly constricted under all conditions on day 4 (Fig. 4-2B). In addition, fluorescence images revealed that MSCs migrated into the parenchymal regions, while vascular networks were not observed in a decellularized liver. Moreover, quantitative analysis showed that recellularized livers greatly constricted in a time-dependent manner (Fig. 4-2D). Although minimum contraction was confirmed when a decellularized liver was seeded at a GFP-HUVEC:MSC ratio of 10:1, these results indicated that decellularized livers seeded with GFP-HUVECs and MSCs cannot maintain their shapes.

To overcome this problem, perfusion culture of a decellularized liver was utilized to prevent tissue contraction by hydrostatic pressure. In this experiment, a decellularized liver seeded with GFP-HUVECs and MSCs at 10:1 ratio was perfused at 1, 2, 3, and 4 ml/min through the PV (Fig. 4-3A). Although quantitative analysis showed that a recellularized liver maintained its shape for 7 days of culture (Fig. 4-3C), vascular networks similar to those constructed in chapter 2 were not observed (Fig. 4-3B).

# Chapter 4 Construction of functional vascular networks in a decellularized liver

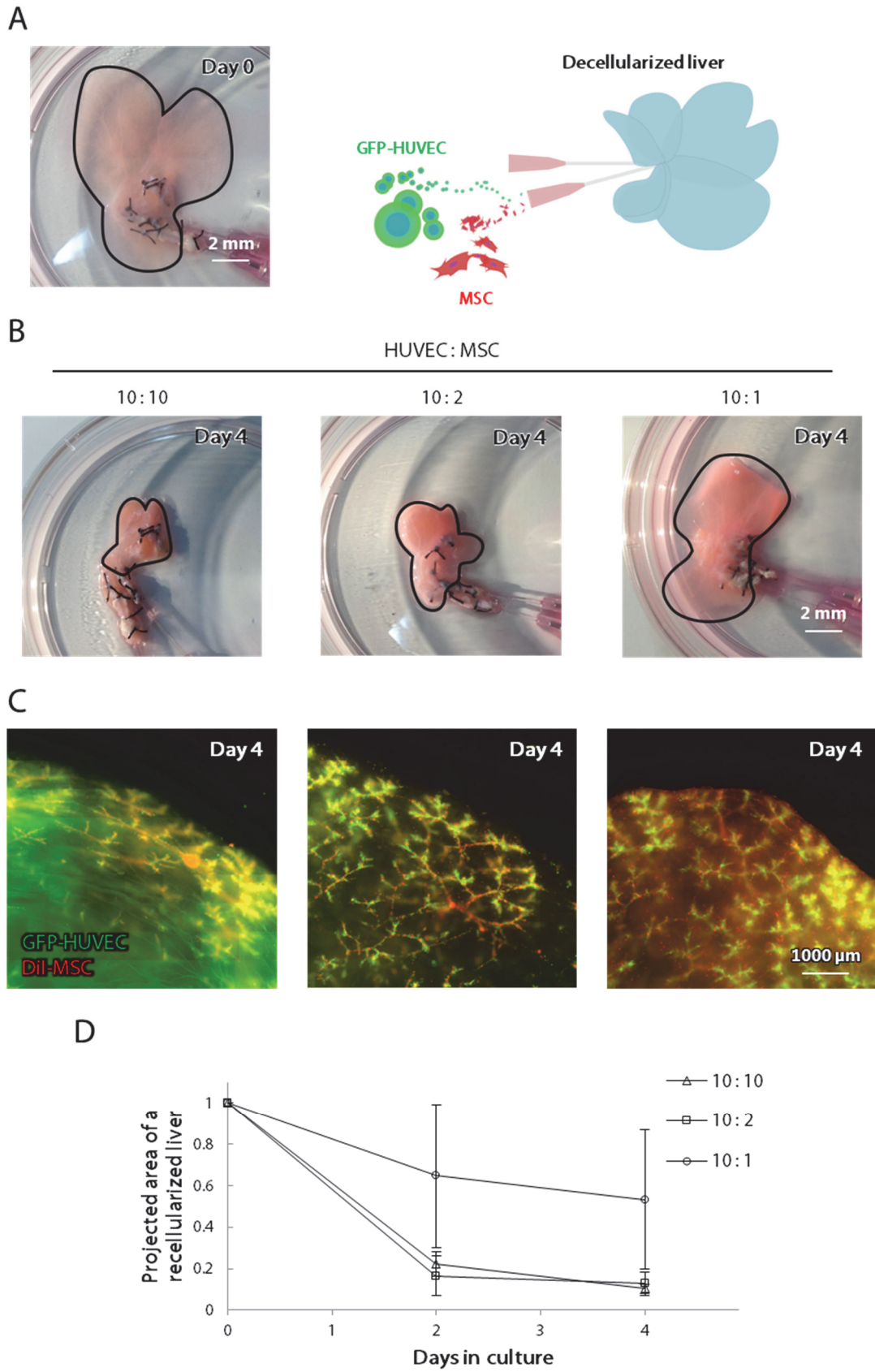


**Fig. 4-2 HUVEC-MSC coculture in a decellularized liver of static culture.** (A) An overall image and a schematic illustration of HUVEC-MSC coculture in decellularized livers. (B, C) Overall and fluorescence images of recellularized livers seeded with different HUVEC-MSC ratios (10:10, 10:2, and 10:1) on days 0, 2, and 4. (D) Quantitative analysis of contraction coefficient of recellularized livers on day 4. Scale bars, 2 mm (A, B), 1000  $\mu\text{m}$  (C). Data are shown as mean  $\pm$  SD (N = 1, n = 3).

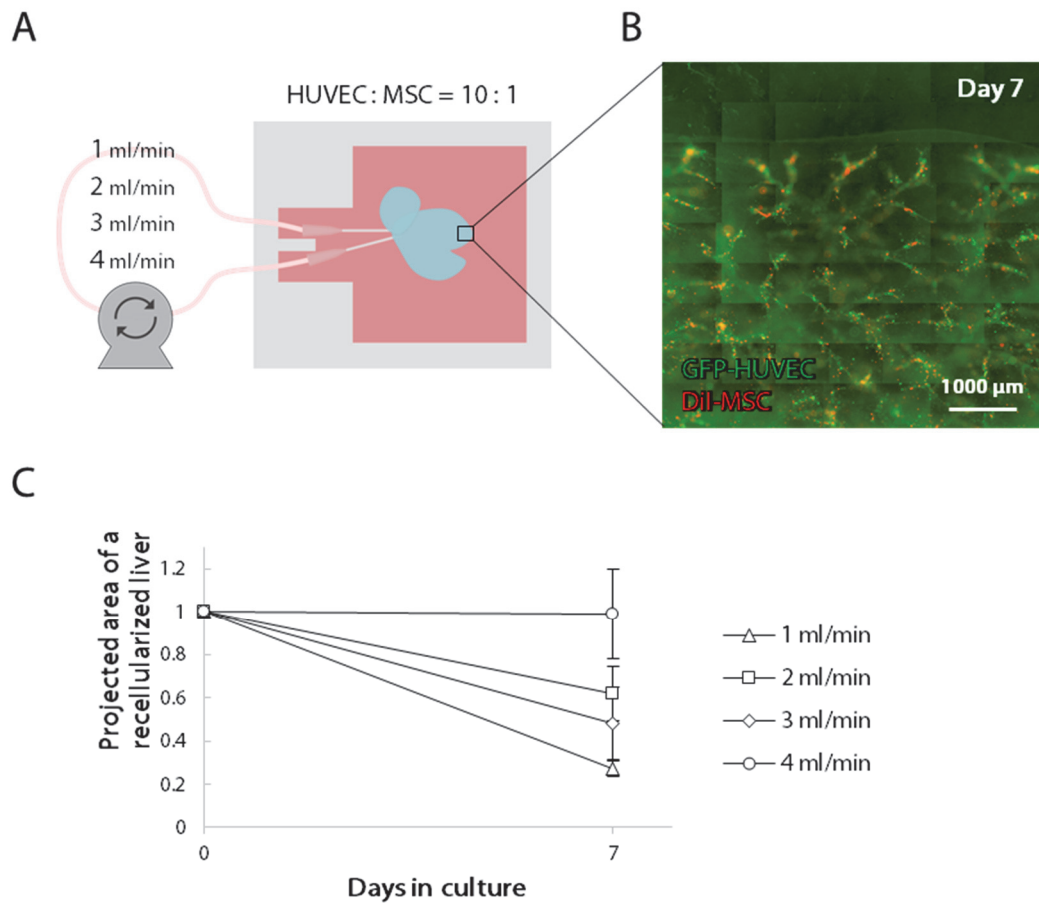


**Fig. 4-3 HUVEC-MSC coculture in decellularized livers of perfusion culture.** (A) A schematic illustration of perfusion culture of HUVEC-MSC coculture in a decellularize liver under different flow rate (1, 2, 3, and 4 ml/min). (B) A fluorescence image of EC networks on day 7 in perfusion culture at 4 ml/min through the PV. GFP-HUVECs and DiI-labeled MSCs were used for this experiment. (C) Quantitative analysis of contraction coefficient of recellularized livers on days 0 and 7. Scale bars, 2 mm (B), 1000  $\mu$ m. Data are shown as mean  $\pm$  SD (N = 1, n = 3).

#### 4-4-2 Maintenance of EC networks in perfusion culture with fibronectin coating

To examine the integrity of constructed sinusoid-scale microvessels, a recellularized liver in perfusion culture with fibronectin coating was monitored. Prior to perfusion culture, a decellularized liver was coated with fibronectin, and then infused with GFP-HUVECs to form sinusoid-scale microvessels (Fig. 4-4A). After 2 days of perfusion culture, sinusoid-scale microvessels were formed in a recellularized liver with continuous lumens (Fig. 4-4B, i–iii). Moreover, these microvessels were also observed on day 4. Although sinusoid-scale microvessels were successfully maintained during days 2–4, these microvessels regressed on day 6 (Fig. 4-4C). Moreover, a quantitative analysis showed that the number of these microvessels was significantly greater on days 2 and 4 compared to that on day 6 (Fig. 4-4D). On the other hand, the length of these microvessels were  $269 \pm 62 \mu\text{m}$  and  $306 \pm 134 \mu\text{m}$  on days 2 and 4, respectively (Fig. 4-4E).

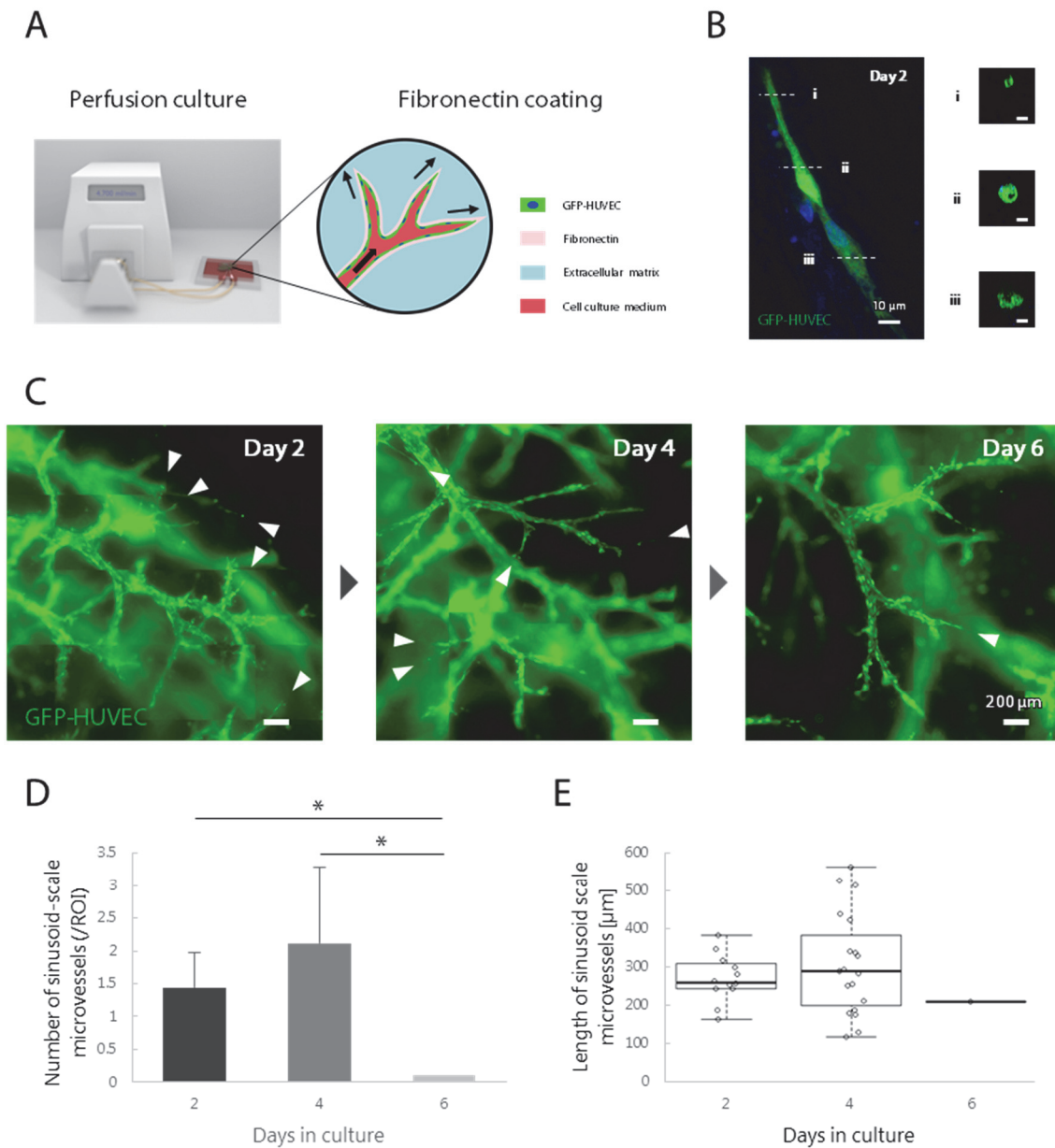


**Fig. 4-4 Maintenance of sinusoid-scale microvessels in perfusion culture of a decellularized liver.** (A) Schematic illustrations of perfusion culture and fibronectin coating. (B) A confocal image of a detailed structure of a constructed sinusoid-scale microvessel on day 2. Cross-sectional images correspond to lines i–iii, which shows continuous lumens of the microvessel. (C) Fluorescence images of constructed EC networks during days 2–6. Arrowheads indicate sinusoid-scale microvessels. (D, E) A quantitative analysis of constructed sinusoid-scale microvessels in decellularized livers.

Number (D) and length (E) of sinusoid-scale microvessels on days 2, 4, and 6 in the 2.0 mm × 2.0 mm ROI. Scale bars, 10 μm (B), 5 μm (i–iii), 200 μm (C). Data are shown as mean ± SD (N = 3, n = 9). \**P* < 0.05.

4-4-3 *Ex vivo* blood perfusion test of a recellularized liver

Following 2 days of cell culture, decellularized and recellularized livers were perfused with diluted whole-blood through the PVs and incubated them for investigating platelet deposition (Fig. 4-5A). After blood perfusion, blood was seen in entire region of a decellularized liver (Fig. 4-5B), while blood was retained in vasculatures in recellularized livers (Fig. 4-5C). Histological analyses revealed that decellularized livers exhibited higher platelet deposition compared to those seeded with ECs. Interestingly, fluorescence images showed that recellularized livers in perfusion culture with fibronectin coating exhibited reduced number of deposited platelets in the  $80 \times 80 \mu\text{m}$  ROI compared to that in static culture (Fig. 4-6A). Moreover, a quantitative analysis of platelet deposition showed that EC networks constructed in the condition of “perfusion + fibronectin” significantly reduced number of platelets compared to that in a decellularized liver (Fig. 4-6B). These results that indicated constructed endothelium in perfusion culture with fibronectin coating had antithrombotic function in terms of platelet deposition.

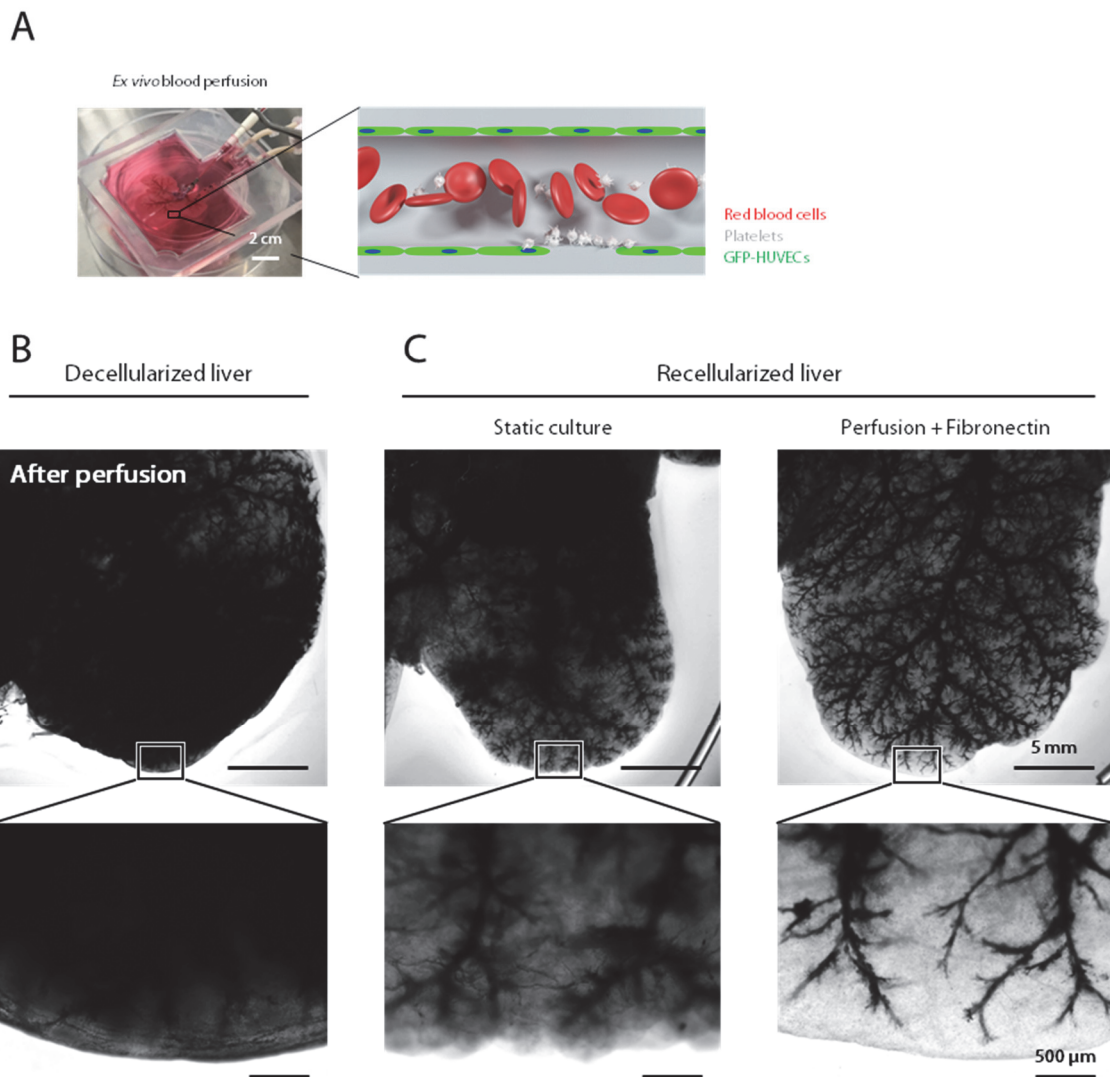


**Fig. 4-5 A schematic illustration and bright field images of decellularized and recellularized livers after blood perfusion.** (A) Schematic diagrams of *ex vivo* perfusion of diluted whole-blood through the PV. (B) Stereomicroscope images of a decellularized liver after blood perfusion. (C) Stereomicroscope images of recellularized livers in static culture and perfusion culture with fibronectin coating after blood perfusion. Scale bars, 5 mm and 500  $\mu\text{m}$ .

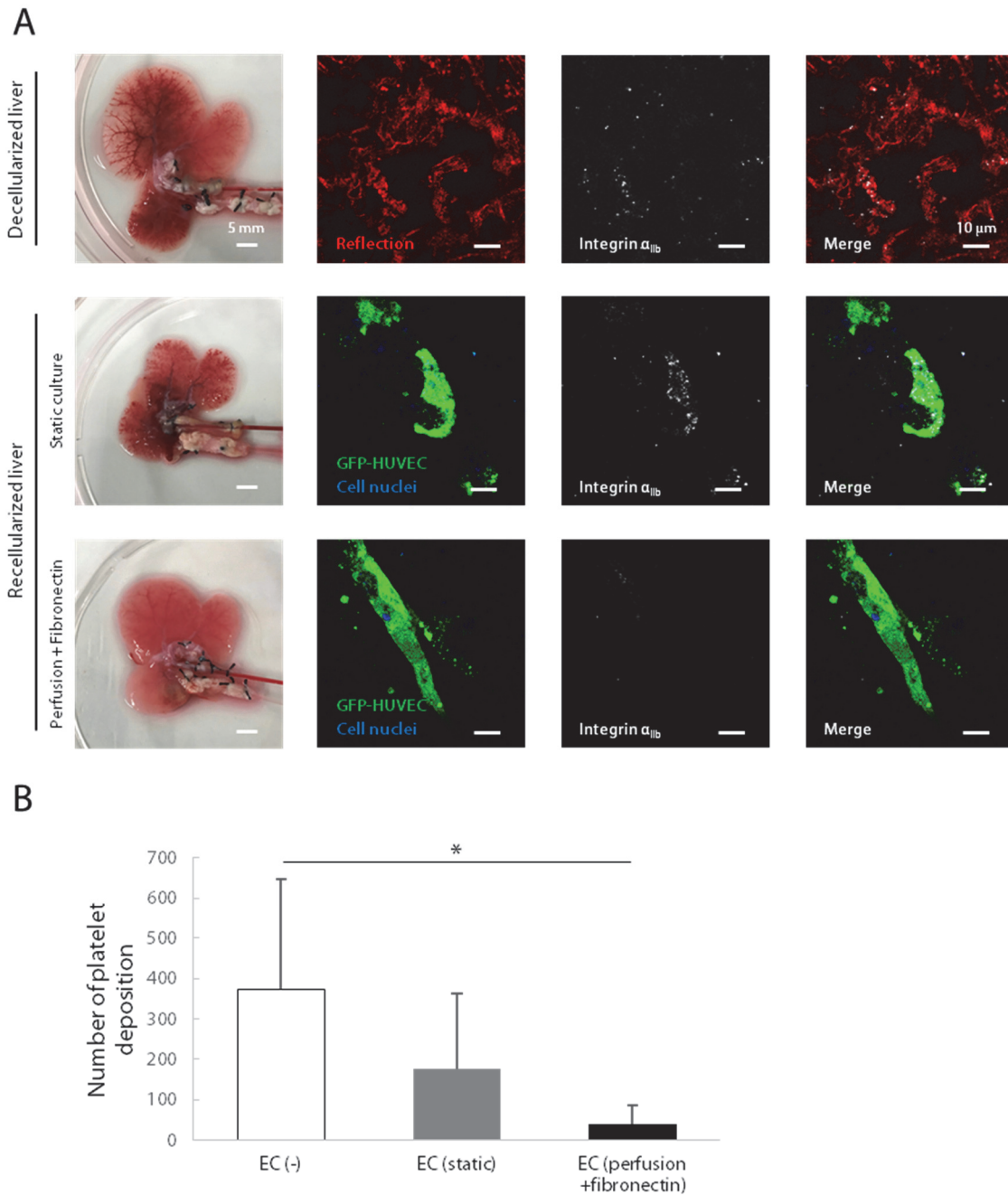


**Fig. 4-6 *Ex vivo* blood perfusion of recellularized livers.** (A) *Ex vivo* blood perfusion of recellularized liver with GFP-HUVECs in “static culture” or “perfusion + fibronectin”. Fluorescence images represent platelet deposition in decellularized or recellularized livers after 1 hour of blood perfusion in each condition. Platelet deposition was detected by an antibody against platelet surface marker, anti-integrin  $\alpha_{IIb}$ . (B) A quantitative analysis of platelet deposition in decellularized livers. Scale bars, 5 mm and 10  $\mu$ m. Data

are shown as mean  $\pm$  SD (N = 2, n = 8). \* $P < 0.05$ .

#### 4-4-4 Comparison of a cell seeding route in a decellularized liver

The liver is composed of several tubular networks such as HA, PV, HV, and BD. These networks can be used as injection routes in a decellularized liver. For this reason, to extend EC networks in a decellularized liver, both PV and HV were used as injection routes. Fluorescence images showed that a hierarchical EC network was formed during days 0–4 when GFP-HUVECs were seeded through PV (“PV” condition) (Fig. 4-7A). In contrast, more complex EC networks were observed in a decellularized liver when ECs were seeded through both the PV and HV (“PV+HV” condition) compared to the “PV” condition (Fig. 4-7B). A quantitative analysis revealed that EC density significantly increased in the “PV+HV” condition compared to that in the “PV” condition (Fig. 4-7C). In addition, total EC length in the “PV+HV” condition was significantly greater than that in the “PV” condition on days 0–4 (Fig. 4-7D).

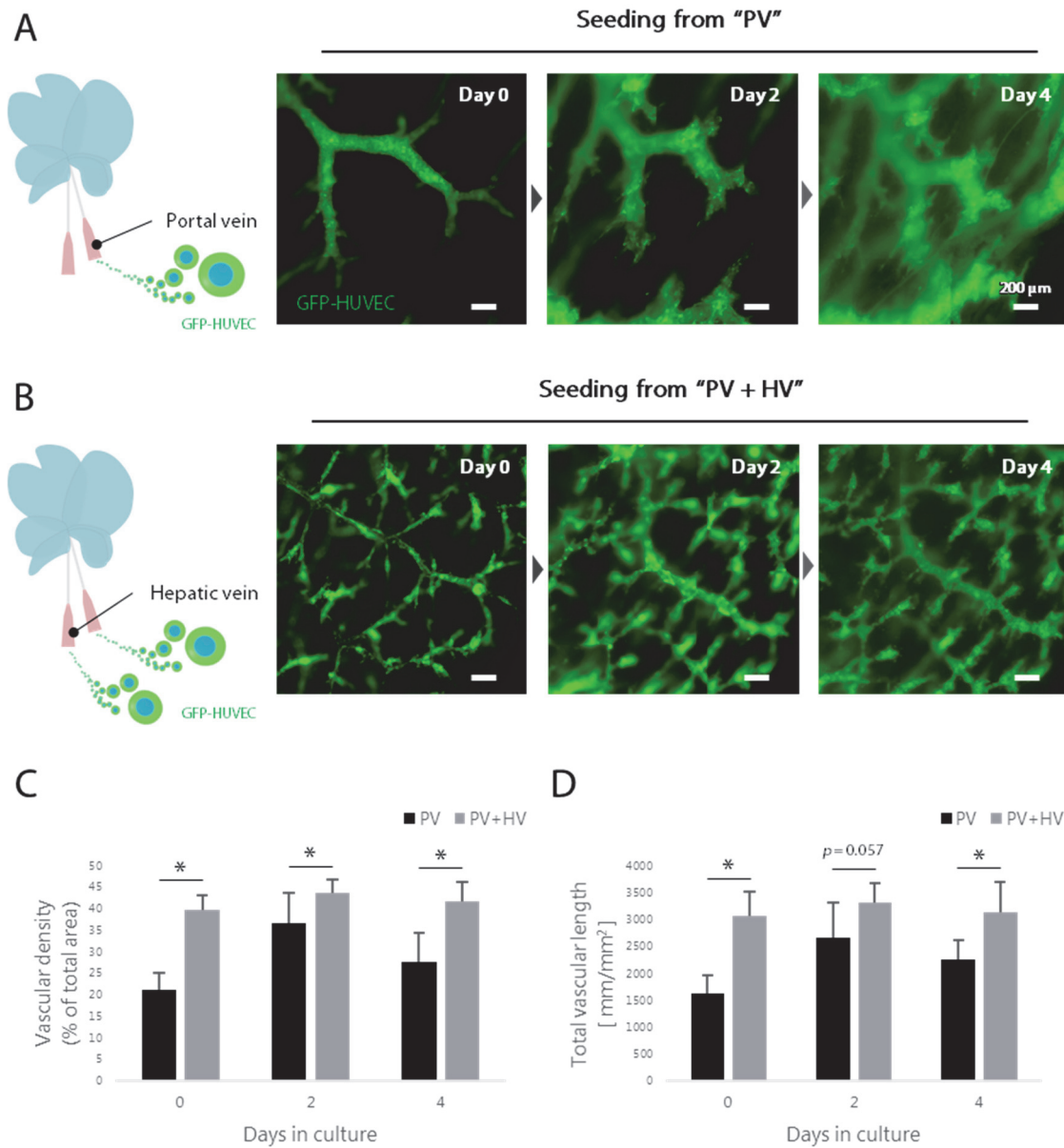


**Fig. 4-7 Comparison of a seeding route for recellularization.** (A, B) Schematic illustrations and fluorescence images of recellularization through the PV (A) or both PV and HV (B). Fluorescence images represent EC networks formed in decellularized livers during days 0–4. (C, D) Quantitative analyses of EC density (C) and total EC length (D). Scale bars, 200  $\mu\text{m}$ . Data are shown as mean  $\pm$  SD (N = 3, n = 9). \* $P < 0.05$ .

Moreover, two types of fluorescent labeled ECs were used in this experiment to distinguish ECs seeded from different routes. To construct vascular networks in a decellularized liver, PV was seeded with GFP-HUVECs, while HV was seeded with DiI-labeled HUVEC, which resulted in the formation of hierarchical EC networks labeled with GFP (green) or DiI (red) (Fig. 4-8A). Fluorescence images showed that GFP-HUVECs and DiI-HUVECs form clearly different EC networks, respectively. These EC networks were maintained for at least 4 days of culture (Fig. 4-8B). However, sinusoid-scale microvessels were not observed in static culture even in the “PV+HV” condition.

Furthermore, under the “perfusion + fibronectin” condition, EC contacts between GFP-labeled EC networks and DiI-labeled EC networks were observed in a decellularized liver on day 2 (Fig. 4-9A, B).

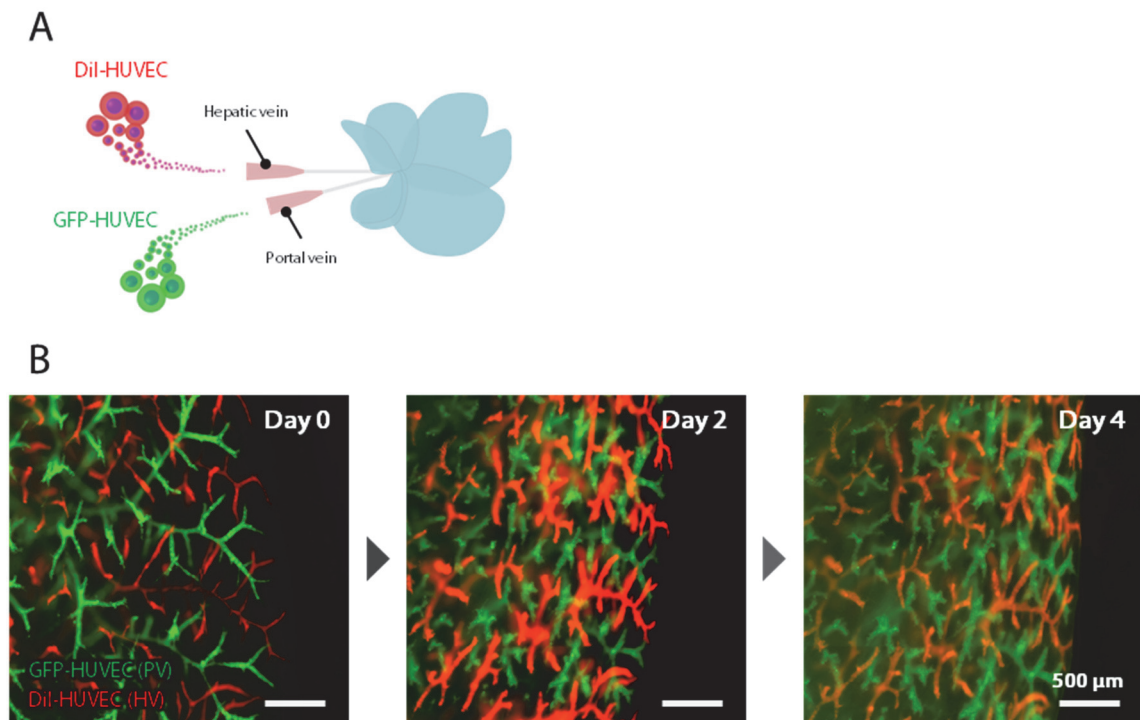


**Fig. 4-8** Live-cell imaging of GFP- and DiI-HUVEC in a decellularized liver. (A) A schematic illustration of cell seeding using GFP-HUVECs and DiI-HUVECs. GFP-HUVECs were seeded through the PV, while DiI-HUVECs were seeded through the HV. (B) Fluorescence images showed two distinct EC networks during days 0–4. The PV and HV networks were composed of GFP-HUVECs and DiI-HUVECs, respectively. Scale bars, 500  $\mu\text{m}$ .

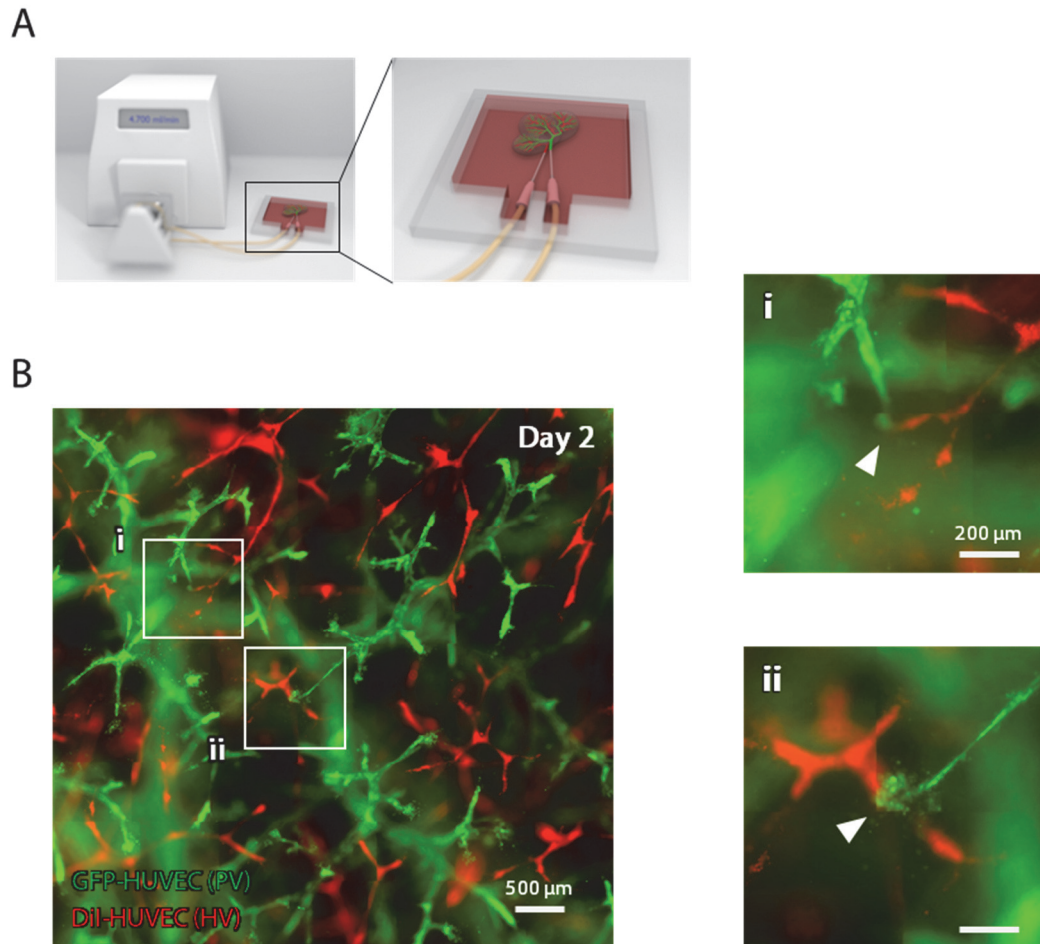


**Fig. 4-9 Live-cell imaging of PV and HV networks in perfusion culture.** (A) Schematic illustrations of perfusion culture of a decellularized liver seeded with GFP-HUVECs and DiI-HUVECs. The reendothelialized liver was perfused with cell culture medium through the PV. (B) Fluorescence images of PV and HV networks. EC contacts between GFP-labeled microvessels and DiI-labeled microvessels were observed on day 2 in a decellularized liver. Scale bars, 500  $\mu\text{m}$  (B), 200  $\mu\text{m}$  (i–ii).

## 4-5 Discussion

Organ decellularization is a promising strategy for the generation of transplantable livers. Several groups have developed functional tissue-engineered liver tissues using decellularized livers in terms of liver structures and functions such as albumin and urea synthesis (Uygun *et al.*, 2010; Ogiso *et al.*, 2016; Baptista *et al.*, 2011; Shirakigawa *et al.*, 2013; Yagi *et al.*, 2013; Kadota *et al.*, 2014; Soto-Gutierrez *et al.*, 2011; Baptista *et al.*, 2016). However, there remained obstacles for clinical use such as clot formation in a decellularized liver due to incomplete vascular formation.

### 4-5-1 HUVEC-MSC coculture in a decellularized liver

Recent evidence have suggested that EC-MSC coculture can induce the formation of microvascular networks *in vitro* (Carrion *et al.*, 2010; McFadden *et al.*, 2013; Yamamoto *et al.*, 2013, 2019). However, EC networks and sinusoid-scale microvessels were not formed in a decellularized liver under HUVEC-MSC coculture condition, while recellularized liver tissues constricted in a time-dependent manner. On the other hand, MSCs were also reported to induce cell-mediated contraction (Nirmalanandhan *et al.*, 2006). Moreover, MSCs on the matrix surface was reported to differentiate toward a myofibroblast or SMC phenotype with ascorbic acid treatment (Weidenhamer *et al.*, 2015), which may result in contraction of recellularized livers. From a practical perspective, it appeared to be difficult to construct stable vascular networks using GFP-HUVECs and MSCs in a decellularized liver due to the tissue contraction.

### 4-5-2 Antithrombotic functions of constructed EC networks

To overcome the problem of clot formation, several groups have focused on reendothelialization of a decellularized liver (Meng *et al.*, 2019; Kojima *et al.*, 2018; Ko *et al.*, 2015; Hussein *et al.*, 2016). Especially, EC networks were successfully constructed including sinusoid-scale microvessels using a decellularized liver in chapter 2 (Watanabe

*et al.*, 2019). However, little is known about antithrombotic functions of constructed sinusoid-scale microvessels in a decellularized liver. Thus, it is essential to investigate whether these microvessels have antithrombotic functions. In this chapter, it is demonstrated that platelet deposition in a decellularized liver effectively reduced in the condition of perfusion culture with fibronectin coating, while platelets were observed in static culture. These results indicated that constructed vascular networks including sinusoid-scale microvessels had antithrombotic functions and might prevent following clot formation (Ruggeri and Mendolicchio, 2007). Moreover, as described in chapter 2, ECs in the condition of perfusion culture and fibronectin coating aligned in the flow direction, while ECs in static culture showed round shape in chapter 2 (Watanabe *et al.*, 2019). This may promote an antithrombotic phenotype on ECs. In addition, platelets observed in this study was smaller than those reported in previous studies (Jain *et al.*, 2016; Barrile *et al.*, 2018). This can be explained by difference in matrix stiffness of a decellularized liver. A previous study determined that Rac1 and actomyosin activity mediate substrate stiffness-dependent platelet adhesion, spreading, and activation to different degrees and suggested that platelets took more time to spread and activate on softer gel less than 2500 kPa (Qiu *et al.*, 2014). In addition, matrix stiffness of a decellularized liver was estimated to be 914 Pa (Nishii *et al.*, 2016).

Although EC networks reduced platelet deposition, platelet deposition was still observed in a decellularized liver even in the condition of perfusion and fibronectin coating. This observation can be explained by two factors. One is an adverse immune response of ECs. For example, Ko *et al.* (2015) and Hussein *et al.* (2016) perfused porcine blood into vascular networks composed of human ECs. On the other hand, Devalliere *et al.* used rat blood and human ECs. In these studies, adverse immune response might induce platelet deposition. The other is due to incomplete coverage of the inner surface of a decellularized liver. When GFP-HUVECs were seeded through PV, they were

distributed in the PV network, while those cells were not observed in the HV network. This may induce platelet deposition in a decellularized liver around the HV network.

### 4-5-3 Maintenance of sinusoid-scale microvessels in a decellularized liver

In the present study, sinusoid-scale microvessels ( $< 15 \mu\text{m}$ ) were formed with the combination of perfusion culture and fibronectin coating. These structures were maintained until day 4, but eventually regressed. Several studies successfully performed *in vitro* formation of vascular networks using a microfluidic chip (Han *et al.*, 2015; Abe *et al.*, 2019; Song and Munn, 2011). However, these vascular networks were unstable and its structures were not maintained for more than 1 week due to the lack of supporting cells such as perivascular cells or fibroblasts (Yamamoto *et al.*, 2013, 2019; Yeon *et al.*, 2012; Wang *et al.*, 2016). These results correspond with the results in this study. These findings suggested that coculture with supporting cells might enable long-term culture of vascular networks in a decellularized liver.

In terms of total length of sinusoid-scale microvessels, GFP-HUVECs extended larger EC networks on day 4 compared to day 2, which suggested that these microvessels extended their structures in a time-dependent manner for at least 4 days. However, length of these microvessels was shorter than the radius of a hepatic lobule (350–500  $\mu\text{m}$ ). Hence, further improvements in terms of microvessel length are needed in order to construct whole-organ EC networks.

### 4-5-4 Optimization of the cell seeding route for recellularization

To improve EC coverage in a decellularized liver, optimization of the cell seeding route was performed. Currently, the PV was generally used as a cell seeding route for recellularization (Uygun *et al.*, 2010; Kojima *et al.*, 2018). However, recent evidence suggests that selection of a seeding route can be critical for recellularization such as cell distribution and engraftment. For example, Ogiso *et al.* (2016) demonstrated that

hepatocyte seeded through the biliary tree entered the parenchyma and distributed throughout the liver lobule. On the other hand, Baptista *et al.* (2011) demonstrated that PV-seeded ECs were predominantly deposited in the periportal regions of the liver lobule, whereas vena cava-perfused beads were concentrated in the region of the CV. However, optimization of the cell seeding route using cells have not been investigated. In this chapter, it was revealed that cell seeding from both PV and HV effectively enhanced EC coverage in a decellularized liver. This result indicated that cells seeded from PV were trapped in the periportal region and were not able to across sinusoid regions toward the CV. These findings indicated that a combination of the optimized seeding route and self-organization by mechanical and chemical factors may be useful to construct microvascular networks between PV and HV.

#### 4-6 Summary

In this chapter, the validity of vascular networks including sinusoid-scale microvessels constructed in a decellularized liver was determined in terms of hemocompatibility. EC networks showed antithrombotic functions and reduced platelet deposition. In particular, the recellularized liver with ECs in the combination of perfusion culture and fibronectin coating significantly reduced platelet deposition compared to the decellularized liver without ECs and fibronectin coating. Furthermore, improvement of EC coverage in a decellularized was achieved. Especially, the use of HV in addition to PV as a route of cell seeding significantly enhanced EC density and total length of EC networks. Taken together, these results indicated that route selection for cell seeding as well as mechanical and chemical factors were important to construct functional EC networks including sinusoid-scale microvessels *in vitro*. These findings will provide useful information for the development of transplantable livers in terms of hemocompatibility.

## Chapter 5 Concluding remarks

### 5-1 Summary and conclusions

*In vitro* construction of tissue-engineered liver transplants has been proposed as an alternative strategy to the conventional liver transplantation, because available donor livers are in short supply. Although the decellularization techniques have allowed us to construct whole-organ liver tissues *in vitro*, it is still difficult to construct transplantable liver tissues due to the lack of intact vascular networks, resulting in clot formation after transplantation. Especially, large vasculatures were successfully constructed in a decellularized liver in previous studies, while little is known about construction of sinusoids ( $< 15 \mu\text{m}$ ). The purpose of this thesis is to develop functional vascular networks including sinusoid-scale microvessels using decellularized livers and determine the validity of the vascular networks in terms of hemocompatibility.

Chapter 2 described the construction of sinusoid-scale microvessels in a decellularized liver by regulating mechanical and chemical factors (Fig. 5-1, chapter 2). Based on hypothesized that both mechanical factors (e.g., shear stress) and chemical factors (e.g., surface coating) can induce formation of microvessels *in vitro*, experiments were performed. To investigate effects of shear stress on EC morphology, an *in vitro* perfusion culture system with a decellularized liver was developed. This experiment demonstrated that perfusion culture promoted formation of sinusoid-scale microvessels in decellularized livers, which was not observed in static culture. In particular, perfusion culture at 4.7 ml/min through the PV promoted the formation of sinusoid-scale microvessels compared to other culture conditions. In particular, range of FSS was important and approximately 0.5 Pa FSS loaded on  $\phi$  50–60  $\mu\text{m}$  blood vessels was critical for the construction of sinusoid-scale microvessels. In perfusion culture, a well-aligned EC layer was observed in a decellularized liver, which suggested that ECs aligned in response to the flow-induced shear stress. Furthermore, the number of sinusoid-scale

## Chapter 5 Concluding remarks

microvessels was significantly increased in perfusion culture of a decellularized liver with fibronectin coating compared to that without the coating. These results indicate that the combination of mechanical and chemical factors (FSS and surface coating of fibronectin) is useful for the effective formation of *in vitro* microvessels.

Chapter 3 described *in vitro* formation of microvascular formation including vascular anastomoses between microvessels in HUVEC-MSC coculture using a microfluidic chip (Fig. 5-1, chapter 3). To construct large tissues containing continuous vascular networks such as arterio-venous networks, formation of vascular anastomosis is an essential process for connection between vasculatures. First, HUVECs were seeded in two channels of a microfluidic chip divided by a gel region. This experiment showed that vascular formation was inhibited when HUVECs were seeded on both sides of the gel, while HUVECs extended vascular networks when they were seeded on one side only. Next, a series of HUVEC:MSC ratios was tested to induce vascular anastomoses. The results demonstrated that addition of MSCs induced vascular anastomosis formation. In particular, the greater number of vascular anastomoses was observed at a HUVEC:MSC ratio of 2:8 compared to the other conditions, which indicated that the ratio of heterotypic cells is important for vascular anastomosis formation. Moreover, the processes of vascular anastomosis in this model was in good agreement with *in vivo* vascular anastomosis formation. Furthermore, these results suggested that local VEGF gradients played important roles in vascular formation. These findings suggest that heterotypic cell–cell interaction is critical and chemical factor (VEGF gradient) is important for *in vitro* formation of vascular anastomosis.

Chapter 4 described improvement of EC coverage in a decellularized liver and determined the validity of constructed EC networks (Fig. 5-1, chapter 4). Although HUVEC-MSC coculture was performed to promote formation of sinusoid-scale microvessels, recellularized livers cannot maintain their shapes due to contraction force of MSCs. Accordingly, HUVEC monoculture was conducted to construct organ-scale

## Chapter 5 Concluding remarks

vascular networks. To construct functional whole-organ liver tissues, it is important to form vascular networks including arteries, veins, and microvessels. It was found that sinusoid-scale microvessels were formed by mechanical and chemical factors in chapter 2, while venous networks were not constructed. The results showed that the use of the HV in addition to the PV as a route of cell seeding significantly enhanced EC density and total length of EC networks in a decellularized liver. These findings indicated that route selection for cell seeding was important for effective reendothelialization. This result indicated that cell seeding through the HV was essential to form HV networks. Moreover, in this chapter, antithrombotic functions of the reendothelialized liver was also assessed. Constructed EC networks reduced platelet deposition in a decellularized liver. In particular, the combination of perfusion culture and fibronectin coating significantly reduced platelet deposition compared to the decellularized liver. This result suggested that GFP-HUVECs formed functional EC networks including sinusoid-scale microvessels in terms of hemocompatibility. These findings suggest that route selection for cell seeding as well as mechanical and chemical factors is important for *in vitro* formation of functional vascular networks including sinusoid-scale microvessels.

In conclusions, the study in this thesis demonstrated the *in vitro* construction of functional organ-scale vascular networks continuing from large vasculatures to sinusoid-scale microvessels in a decellularized liver. These findings will provide important insights for *in vitro* fabrication of transplantable liver tissues in terms of vascularization.

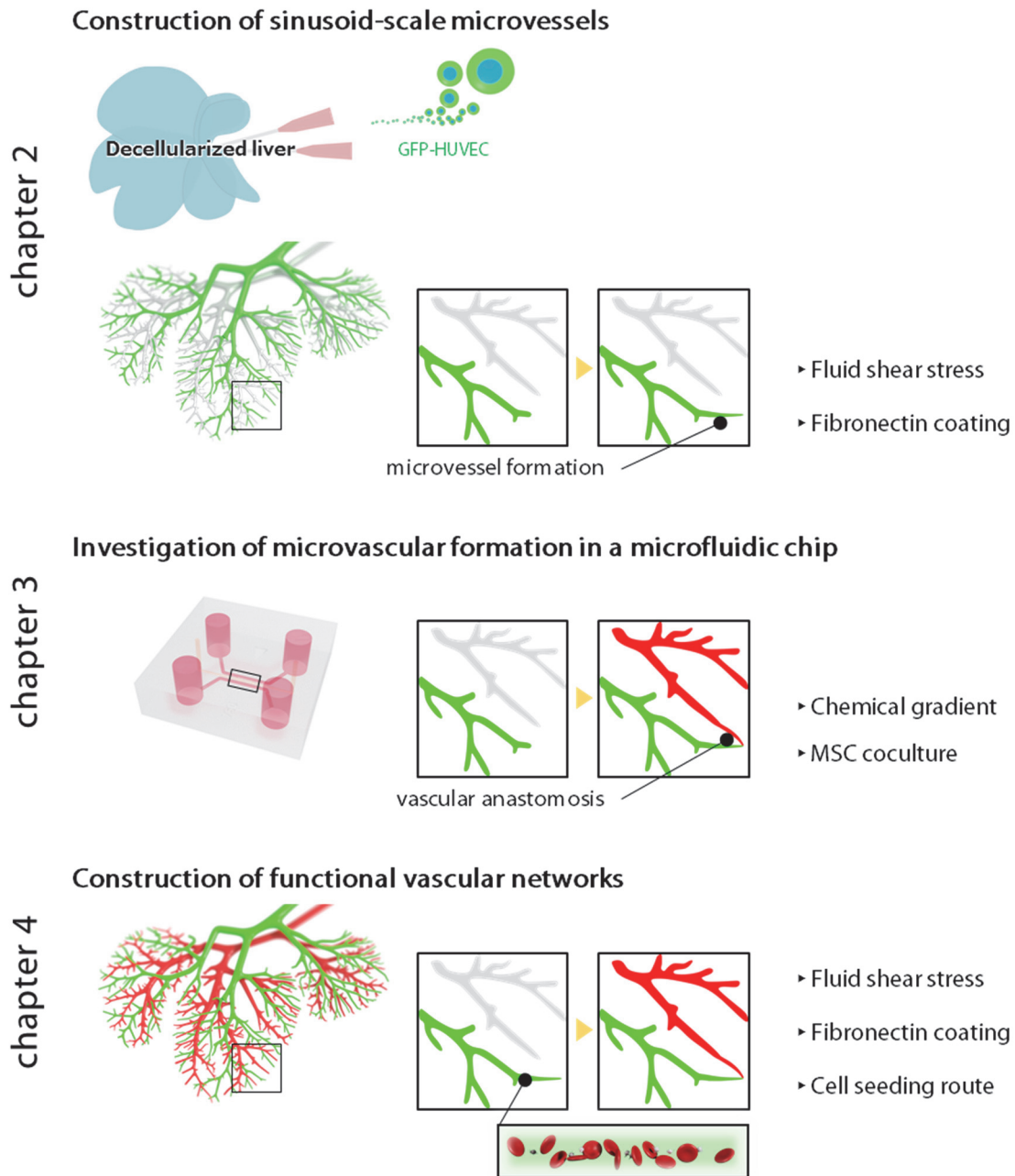


**Fig. 5-1 Summary of findings obtained in this thesis.** In chapter 2, it was demonstrated that fluid shear stress and surface coating of fibronectin promoted the formation of sinusoid-scale microvessels. In chapter 3, the results indicated that VEGF gradient and coculture with MSC were useful for the formation of microvascular networks including vascular anastomosis. Finally, in chapter 4, it was demonstrated that cell seeding route as

## Chapter 5 Concluding remarks

well as the combination of mechanical and chemical factors were important for the construction of functional vascular networks.

### 5-2 Future prospects

Although functional EC networks were obtained using decellularized livers, this model still has room for improvement. For example, further improvement of EC coverage will be needed for clinical transplantation of liver tissues. To achieve blood perfusion in liver tissues, complete EC coverage of vasculatures and connection between PV and HV networks such as vascular anastomoses are essential. Moreover, the density of microvessels should be improved since sinusoid-scale microvessels had lower density compared to sinusoidal networks in *in vivo* hepatic lobule (Morita *et al.*, 1998).

To obtain functional tissue-engineered liver grafts *in vitro*, reconstruction of both parenchymal tissues containing hepatocytes) and non-parenchymal tissues containing cholangiocytes, Kupffer cells, HSCs, LSECs will be required. To construct parenchymal tissues, a combination of decellularized livers and iPSC-derived hepatic cells (Takayama *et al.*, 2014, 2012; Kido *et al.*, 2015; Kouji *et al.*, 2017) produced from patients will be valid because both of them have low immunogenicity and may avoid adverse immune response after transplantation. Moreover, a previous study demonstrated construction of biliary networks *in vitro* with continuous lumen using rat cholangiocytes (Hashimoto *et al.*, 2008). These results might be applied to whole-organ liver engineering including parenchymal tissues, vascular networks, and biliary networks in a decellularized liver.

Regarding scaffolds for organ engineering, it has been believed that the use of 3D bioprinters alone will not be enough for biofabrication of human organs supported by a short review of Mironov *et al.* (2011). However, recent advances enabled biofabrication of large tissues using 3D printers based on inkjet technology, direct extrusion technology, stereolithography, and laser lithography (Pereira *et al.*, 2018). More recently, Noor *et al.* (2019) developed a whole-heart structure with major blood vessels 3D printing techniques using patient-derived hydrogels. Moreover, Grigoryan *et al.* (2019) developed a bioinspired lung alveolar model by stereolithographic production of synthetic polymer hydrogels containing intricate and functional vascular architectures in terms of

oxygenation. In the future, these techniques may develop an organ-scale scaffold using only artificial materials such as synthetic polymers instead of the current tissue-derived biomaterials such as decellularized organs.

Besides liver transplantation, this decellularized liver graft has potential as physiological and pathological liver models, which enhance our understanding of liver biology by providing representative platforms for drug toxicity studies (Damania *et al.*, 2014). Drug-induced hepatotoxicity is of concern in drug discovery and development because drug-induced liver injury is a cause of acute and chronic liver disease. Hence, *in vitro* liver models and preclinical trials are needed for drug assessment. This decellularized liver model may further enhance understanding of bile-related disorders and hugely impact the field of drug developments since decellularized livers retain native liver microenvironment. With recent advances in technology, it is possible to establish models that resembles native liver using decellularized livers and may serve as a guide to unresolved questions. Furthermore, tissue-engineered liver tissues using decellularized liver grafts would be used as cancer metastasis models. Since decellularized livers retain native ECM structures, these liver grafts can recapitulate *in vivo* microenvironments with its cell–cell and cell–ECM which may propose new treatment strategies for cancer.

This thesis proposed various strategies for *in vitro* formation of vascular networks. These strategies can be adopted for other purposes. For example, chapter 2 indicated that ECs formed *in vitro* microvessels in response to approximately 0.5 Pa FSS in combination with fibronectin. This finding may support microvessel formation in other biomaterials such as decellularized organs and tissues, which can prevent clot formation and enable oxygen and nutrients supply. In addition, chapter 3 demonstrated that heterotypic cell–cell interaction was useful for *in vitro* vascular anastomosis formation. This anastomosis model can provide useful insights to construct a larger tissue by assembling multiple

## Chapter 5 Concluding remarks

tissue-engineered constructs by forming vascular anastomosis between these tissues. Moreover, chapter 4 was designed to test antithrombotic functions by perfusion of whole blood. This model can be used as an *in vitro* organ-scale thrombosis model to investigate EC–blood interactions, which may be useful to analyze hematologic diseases such as hemophilia.

In conclusion, these techniques for *in vitro* construction of vascular networks described in this thesis based on decellularization techniques would be useful for clinical application in many aspects.

## References

- Abe, Y., M. Watanabe, S. Chung, R.D. Kamm, K. Tanishita, and R. Sudo. 2019. Balance of interstitial flow magnitude and vascular endothelial growth factor concentration modulates three-dimensional microvascular network formation. *APL Bioeng.* 3:1–12.
- Adeva-Andany, M.M., N. Pérez-Felpete, C. Fernández-Fernández, C. Donapetry-García, and C. Pazos-García. 2016. Liver glucose metabolism in humans. *Biosci. Rep.* 36:1–15.
- Ajoudanian, M., K. Enomoto, Y. Tokunaga, H. Minami, S. Chung, K. Tanishita, R.D. Kamm, and R. Sudo. 2019. Self-organization of hepatocyte morphogenesis depending on the size of collagen microbeads relative to hepatocytes. *Biofabrication.* 11:1–11.
- Almazroo, O.A., M.K. Miah, and R. Venkataramanan. 2017. Drug Metabolism in the Liver. *Clin. Liver Dis.* 21:1–20.
- Baeyens, N., S. Nicoli, B.G. Coon, T.D. Ross, K. Van Den Dries, J. Han, H.M. Lauridsen, C.O. Mejean, A. Eichmann, J.L. Thomas, J.D. Humphrey, and M.A. Schwartz. 2015. Vascular remodeling is governed by a VEGFR3-dependent fluid shear stress set point. *Elife.* 2015:1–35.
- Baptista, P.M., E.C. Moran, D. Vyas, M.H. Ribeiro, A. Atala, J.L. Sparks, and S. Soker. 2016. Fluid Flow Regulation of Revascularization and Cellular Organization in a Bioengineered Liver Platform. *Tissue Eng. Part C.* 22:199–207.
- Baptista, P.M., M.M. Siddiqui, G. Lozier, S.R. Rodriguez, A. Atala, and S. Soker. 2011. The use of whole organ decellularization for the generation of a vascularized liver organoid. *Hepatology.* 53:604–617.
- Barrile, R., A.D. van der Meer, H. Park, J.P. Fraser, D. Simic, F. Teng, D. Conegliano, J. Nguyen, A. Jain, M. Zhou, K. Karalis, D.E. Ingber, G.A. Hamilton, and M.A. Otieno. 2018. Organ-on-Chip Recapitulates Thrombosis Induced by an anti-CD154 Monoclonal Antibody: Translational Potential of Advanced Microengineered Systems. *Clin. Pharmacol. Ther.* 104:1240–1248.
- Beckermann, B.M., G. Kallifatidis, A. Groth, D. Frommhold, A. Apel, J. Mattern, A. V. Salnikov, G. Moldenhauer, W. Wagner, A. Diehlmann, R. Saffrich, M. Schubert, A.D. Ho, N. Giese, M.W. Büchler, H. Friess, P. Büchler, and I. Herr. 2008. VEGF expression by mesenchymal stem cells contributes to angiogenesis in pancreatic carcinoma. *Br. J. Cancer.* 99:622–631.
- Bernabeu, M.O., M.L. Jones, J.H. Nielsen, T. Krüger, R.W. Nash, D. Groen, S. Schmieschek, J. Hetherington, H. Gerhardt, C.A. Franco, and P. V Coveney. 2014. Computer simulations reveal complex distribution of haemodynamic forces in a mouse retina model of angiogenesis. *Interface.* 11:1–17.
- Bogorad, M.I., J. DeStefano, J. Karlsson, A.D. Wong, S. Gerecht, and P.C. Searson. 2015. Review: In vitro microvessel models. *Lab Chip.* 15:4242–4255.
- Boyer, J.L. 1996. Bile duct epithelium: Frontiers in transport physiology. *Am. J. Physiol.*

## References

- *Gastrointest. Liver Physiol.* 270:1–5.
- Brennan, M.P., A. Dardik, N. Hibino, J.D. Roh, G.N. Nelson, X. Papademitris, T. Shinoka, and C.K. Breuer. 2008. Tissue-engineered vascular grafts demonstrate evidence of growth and development when implanted in a juvenile animal model. *Ann. Surg.* 248:370–376.
- Bruinsma, B.G., Y. Kim, T.A. Berendsen, S. Ozer, and B.E. Uygun. 2015. Layer-by-layer heparinization of decellularized liver matrices to reduce thrombogenicity of tissue engineered grafts. *J. Clin. Transl. Res.* 1:1–17.
- Buchanan, C.F., S.S. Verbridge, P.P. Vlachos, and M.N. Rylander. 2014. Flow shear stress regulates endothelial barrier function and expression of angiogenic factors in a 3D microfluidic tumor vascular model. *Cell Adh. Migr.* 8:517–524.
- Budd, J.S., K.E. Allen, P.R.F. Bell, and R.F.L. James. 1990. The effect of varying fibronectin concentration on the attachment of endothelial cells to polytetrafluoroethylene vascular grafts. *J. Vasc. Surg.* 12:126–130.
- Bussmann, J., S.A. Wolfe, and A.F. Siekmann. 2011. Arterial-venous network formation during brain vascularization involves hemodynamic regulation of chemokine signaling. *Development.* 138:1717–1726.
- Caplan, A.L. 2016. Finding a solution to the organ shortage. *Can. Med. Assoc. J.* 188:1182–1183.
- Caralt, M., J.S. Uzarski, S. Jacob, K.P. Obergfell, N. Berg, B.M. Bijonowski, K.M. Kiefer, H.H. Ward, A. Wandinger-Ness, W.M. Miller, Z.J. Zhang, M.M. Abecassis, and J.A. Wertheim. 2015. Optimization and critical evaluation of decellularization strategies to develop renal extracellular matrix scaffolds as biological templates for organ engineering and transplantation. *Am J Transpl.* 15:64–75.
- Carrion, B., C.P. Huang, C.M. Ghajar, S. Kachgal, E. Kniazeva, N.L. Jeon, and A.J. Putnam. 2010. Recreating the Perivascular Niche Ex Vivo Using a Microfluidic Approach. *Biotechnol. Bioeng.* 107:1020–1028.
- Cheng, G., S. Liao, H.K. Wong, D.A. Lacorre, E. Di Tomaso, P. Au, D. Fukumura, R.K. Jain, and L.L. Munn. 2011. Engineered blood vessel networks connect to host vasculature via wrapping-and-tapping anastomosis. *Blood.* 118:4740–4749.
- Chung, S., R. Sudo, P.J. MacK, C.R. Wan, V. Vickerman, and R.D. Kamm. 2009. Cell migration into scaffolds under co-culture conditions in a microfluidic platform. *Lab Chip.* 9:269–275.
- Cines, D.B., E.S. Pollak, C.A. Buck, J. Loscalzo, G.A. Zimmerman, R.P. McEver, J.S. Pober, T.M. Wick, B.A. Konkle, B.S. Schwartz, E.S. Barnathan, K.R. McCrae, B.A. Hug, A.-M. Schmidt, and D.M. Stern. 1998. Endothelial Cells in Physiology and in the Pathophysiology of Vascular Disorders. *Blood.* 91:3527–3561.
- Colgan, O.C., G. Ferguson, N.T. Collins, R.P. Murphy, G. Meade, P.A. Cahill, and P.M. Cummins. 2007. Regulation of bovine brain microvascular endothelial tight junction assembly and barrier function by laminar shear stress. *Am. J. Physiol. Circ. Physiol.* 292:3190–3197.

## References

- Cox, B., and A. Emili. 2006. Tissue subcellular fractionation and protein extraction for use in mass-spectrometry-based proteomics. *Nat. Protoc.* 1:1872–1878.
- Crapo, P.M., T.W. Gilbert, and S.F. Badylak. 2011. An overview of tissue and whole organ decellularization processes. *Biomaterials.* 32:3233–3243.
- Damania, A., E. Jain, and A. Kumar. 2014. Advancements in in vitro hepatic models: Application for drug screening and therapeutics. *Hepatol. Int.* 8:23–38.
- Davis, C.A., S. Zambrano, P. Anumolu, A.C.B. Allen, L. Sonoqui, and M.R. Moreno. 2015. Device-Based In Vitro Techniques for Mechanical Stimulation of Vascular Cells: A Review. *J. Biomech. Eng.* 137:1–22.
- Deanfield, J.E., J.P. Halcox, and T.J. Rabelink. 2007. Endothelial function and dysfunction: Testing and clinical relevance. *Circulation.* 115:1285–1295.
- Debbaut, C., D. De Wilde, C. Casteleyn, P. Cornillie, D. Van Loo, L. Van Hoorebeke, D. Monbaliu, Y.D. Fan, and P. Segers. 2012. Modeling the impact of partial hepatectomy on the hepatic hemodynamics using a rat model. *IEEE Trans. Biomed. Eng.* 59:3293–3303.
- Devalliere, J., Y. Chen, K. Dooley, M.L. Yarmush, and B.E. Uygun. 2018. Improving functional re-endothelialization of acellular liver scaffold using REDV cell-binding domain. *Acta Biomater.* 78:151–164.
- Dewey CF Jr, Bussolari SR, Gimbrone MA Jr, D.P. 1981. The dynamic response of vascular endothelial cells to fluid shear stress. *J Biomech Eng.* 103:177–185.
- van Duinen, V., D. Zhu, C. Ramakers, A.J. van Zonneveld, P. Vulto, and T. Hankemeier. 2019. Perfused 3D angiogenic sprouting in a high-throughput in vitro platform. *Angiogenesis.* 22:157–165.
- Elias, H. 1949. A re-examination of the structure of the mammalian liver. *Am. J. Anat.* 84:311–333.
- Esmon, C.T. 1995. Thrombomodulin as a model of molecular mechanisms that modulate protease specificity and function at the vessel surface. *FASEB J.* 9:946–955.
- Even-Ram, S., and K.M. Yamada. 2005. Cell migration in 3D matrix. *Curr. Opin. Cell Biol.* 17:524–532.
- Fisher, R.A., and S.C. Strom. 2006. Human hepatocyte transplantation: Worldwide results. *Transplantation.* 82:441–449.
- Fox, I.J., J.R. Chowdhury, S.S. Kaufman, T.C. Goertzen, N.R. Chowdhury, P.I. Warkentin, K. Dorko, B. V. Sauter, and S.C. Strom. 1998. Treatment of the Crigler-Najjar syndrome type I with hepatocyte transplantation. *N. Engl. J. Med.* 338:1422–1426.
- Funahashi, Y., C.J. Shawber, A. Sharma, E. Kanamaru, Y.K. Choi, and J. Kitajewski. 2011. Notch modulates VEGF action in endothelial cells by inducing Matrix Metalloprotease activity. *Vasc. Cell.* 3:1–12.
- Galie, P.A., D.-H.T. Nguyen, C.K. Choi, D.M. Cohen, P.A. Janmey, and C.S. Chen. 2014.

## References

- Fluid shear stress threshold regulates angiogenic sprouting. *Proc. Natl. Acad. Sci.* 111:7968–7973.
- Gerhardt, H. 2008. VEGF and endothelial guidance in angiogenic sprouting. *Organogenesis.* 4:241–246.
- Ghaffari, S., R.L. Leask, and E.A. V Jones. 2015. Flow dynamics control the location of sprouting and direct elongation during developmental angiogenesis. *Development.* 142:4151–7.
- Gilbert, T.W., S. Wognum, E.M. Joyce, D.O. Freytes, M.S. Sacks, and S.F. Badylak. 2008. Collagen fiber alignment and biaxial mechanical behavior of porcine urinary bladder derived extracellular matrix. *Biomaterials.* 29:4775–4782.
- Gilpin, A., and Y. Yang. 2017. Decellularization Strategies for Regenerative Medicine: From Processing Techniques to Applications. *Biomed Res. Int.* 2017:1–13.
- Gordillo, M., T. Evans, and V. Gouon-Evans. 2015. Orchestrating liver development. *Development.* 142:2094–2108.
- Gray, K.M., and K.M. Stroka. 2017. Vascular endothelial cell mechanosensing: New insights gained from biomimetic microfluidic models. *Semin. Cell Dev. Biol.* 71:106–117.
- Grigoryan, B., S.J. Paulsen, D.C. Corbett, D.W. Sazer, C.L. Fortin, A.J. Zaita, P.T. Greenfield, N.J. Calafat, J.P. Gounley, A.H. Ta, F. Johansson, A. Randles, J.E. Rosenkrantz, J.D. Louis-Rosenberg, P.A. Galie, K.R. Stevens, and J.S. Miller. 2019. Multivascular networks and functional intravascular topologies within biocompatible hydrogels. *Science.* 364:458–464.
- Guyette, J.P., S.E. Gilpin, J.M. Charest, L.F. Tapias, X. Ren, and H.C. Ott. 2014. Perfusion decellularization of whole organs. *Nat. Protoc.* 9:1451–1468.
- Haga, J., M. Shimazu, G. Wakabayashi, M. Tanabe, S. Kawachi, Y. Fuchimoto, K.H. Yasuhide, M. Masaki, K. Masaki, and Y. Kitagawa. 2008. Liver regeneration in donors and adult recipients after living donor liver transplantation. *Liver Transplant.* 14:1718–1724.
- Han, S., Y. Shin, H.E. Jeong, J.S. Jeon, R.D. Kamm, D. Huh, L.L. Sohn, and S. Chung. 2015. Constructive remodeling of a synthetic endothelial extracellular matrix. *Sci. Reports.* 5:1–10.
- Hashimoto, W., R. Sudo, K. Fukasawa, M. Ikeda, T. Mitaka, and K. Tanishita. 2008. Ductular network formation by rat biliary epithelial cells in the dynamical culture with collagen gel and dimethylsulfoxide stimulation. *Am. J. Pathol.* 173:494–506.
- Hasso, S., and J. Chan. 2011. Chemical Approaches to Angiogenesis in Development and Regeneration. *Methods Cell Biol.* 101:181–195.
- Helm, C.-L.E., M.E. Fleury, A.H. Zisch, F. Boschetti, and M.A. Swartz. 2005. Synergy between interstitial flow and VEGF directs capillary morphogenesis in vitro through a gradient amplification mechanism. *Proc. Natl. Acad. Sci. U. S. A.* 102:15779–15784.

## References

- Herity, N.A., M.R. Ward, S. Lo, and A.C. Yeung. 1999. Review: Clinical Aspects of Vascular Remodeling. *J. Cardiovasc. Electrophysiol.* 10:1016–1024.
- Herwig, L., Y. Blum, A. Krudewig, E. Ellertsdottir, A. Lenard, H.G. Belting, and M. Affolter. 2011. Distinct cellular mechanisms of blood vessel fusion in the zebrafish embryo. *Curr. Biol.* 21:1942–1948.
- Higgins, G.M., and R.M. Anderson. 1931. Experimental Pathology of the Liver. Restoration of the Liver of the White Rat Following Partial Surgical Removal. *Am. Med. Assoc. Arch. Pathol.* 12:186–202.
- Hirschi, K.K., and P.A. D'Amore. 1996. Pericytes in the microvasculature. *Cardiovasc. Res.* 32:687–698.
- Hodde, J., A. Janis, D. Ernst, D. Zopf, D. Sherman, and C. Johnson. 2007. Effects of sterilization on an extracellular matrix scaffold: Part I. Composition and matrix architecture. *J. Mater. Sci. Mater. Med.* 18:537–543.
- Hofmann, A.F. 1988. Bile Salts As Biological Surfactants. *Colloids and Surfaces.* 30:145–173.
- Hong, J.C., R. Venick, H. Yersiz, P. Kositamongkol, F.M. Kaldas, H. Petrowsky, D.G. Farmer, V. Agopian, S. V. McDiarmid, J.R. Hiatt, and R.W. Busuttil. 2014. Liver transplantation in children using organ donation after circulatory death: A case-control outcomes analysis of a 20-year experience in a single center. *JAMA Surg.* 149:77–82.
- Hsu, Y.H., M.L. Moya, P. Abiri, C.C.W. Hughes, S.C. George, and A.P. Lee. 2013. Full range physiological mass transport control in 3D tissue cultures. *Lab Chip.* 13:81–89.
- Huang, Y., D. Tong, S. Zhu, L. Wu, Q. Mao, Z. Ibrahim, W.P.A. Lee, G. Brandacher, and J.U. Kang. 2015. Evaluation of microvascular anastomosis using real-time, ultra-high-resolution, fourier domain doppler optical coherence tomography. *Plast. Reconstr. Surg.* 135:711–720.
- Hussein, K.H., K.-M. Park, K.-S. Kang, and H.-M. Woo. 2016. Heparin-gelatin mixture improves vascular reconstruction efficiency and hepatic function in bioengineered livers. *Acta Biomater.* 38:82–93.
- Ishibazawa, A., T. Nagaoka, T. Takahashi, K. Yamamoto, A. Kamiya, J. Ando, and A. Yoshida. 2011. Effects of Shear Stress on the Gene Expressions of Endothelial Nitric Oxide Synthase, Endothelin-1, and Thrombomodulin in Human Retinal Microvascular Endothelial Cells. *Investig. Ophthalmology Vis. Sci.* 52:8496–8504.
- Jadlowiec, C.C., T. Taner, and W.J. Von. 2016. Liver transplantation: Current status and challenges. *World J Gastroenterol.* 22:4438–4445.
- Jain, A., A.D. van der Meer, A.L. Papa, R. Barrile, A. Lai, B.L. Schlechter, M.A. Otieno, C.S. Loudon, G.A. Hamilton, A.D. Michelson, A.L. Frelinger, and D.E. Ingber. 2016. Assessment of whole blood thrombosis in a microfluidic device lined by fixed human endothelium. *Biomed. Microdevices.* 18:1–7.
- Japan OrganTransplant Network. 2019. 2019 Japan OrganTransplant Network.

## References

- Jeon, J.S., S. Bersini, J.A. Whisler, M.B. Chen, G. Dubini, J.L. Charest, M. Moretti, and R.D. Kamm. 2014. Generation of 3D functional microvascular networks with human mesenchymal stem cells in microfluidic systems. *Integr. Biol.* 6:555–563.
- Jeong, G.S., S. Han, Y. Shin, G.H. Kwon, R.D. Kamm, S.H. Lee, and S. Chung. 2011. Sprouting angiogenesis under a chemical gradient regulated by interactions with an endothelial monolayer in a microfluidic platform. *Anal. Chem.* 83:8454–8459.
- Ji, R., N. Zhang, N. You, Q. Li, W. Liu, N. Jiang, J. Liu, H. Zhang, D. Wang, K. Tao, and K. Dou. 2012. The differentiation of MSCs into functional hepatocyte-like cells in a liver biomatrix scaffold and their transplantation into liver-fibrotic mice. *Biomaterials.* 33:8995–9008.
- Jung, Y., H. Ji, Z. Chen, H. Fai Chan, L. Atchison, B. Klitzman, G. Truskey, and K.W. Leong. 2015. Scaffold-free, Human Mesenchymal Stem Cell-Based Tissue Engineered Blood Vessels. *Sci. Rep.* 5:1–9.
- Kadota, Y., H. Yagi, K. Inomata, K. Matsubara, T. Hibi, Y. Abe, M. Kitago, M. Shinoda, H. Obara, O. Itano, and Y. Kitagawa. 2014. Mesenchymal stem cells support hepatocyte function in engineered liver grafts. *Organogenesis.* 10:268–277.
- Kang, H., K. Bayless, and R. Kaunas. 2008. Fluid shear stress modulates endothelial cell invasion into three-dimensional collagen matrices. *Am. J. Physiol. Circ. Physiol.* 295:2087–2097.
- Kasuya, J., R. Sudo, G. Masuda, T. Mitaka, M. Ikeda, and K. Tanishita. 2015. Reconstruction of hepatic stellate cell-incorporated liver capillary structures in small hepatocyte tri-culture using microporous membranes. *J. Tissue Eng. Regen. Med.* 9:247–256.
- Kasuya, J., R. Sudo, R. Tamogami, G. Masuda, T. Mitaka, M. Ikeda, and K. Tanishita. 2012. Reconstruction of 3D stacked hepatocyte tissues using degradable, microporous poly(D,L-lactide-co-glycolide) membranes. *Biomaterials.* 33:2693–2700.
- Kido, T., Y. Kouji, K. Suzuki, A. Kobayashi, Y. Miura, E.Y. Chern, M. Tanaka, and A. Miyajima. 2015. CPM is a useful cell surface marker to isolate expandable bi-potential liver progenitor cells derived from human iPS cells. *Stem Cell Reports.* 5:508–515.
- Kim, S., H. Lee, M. Chung, and N.L. Jeon. 2013. Engineering of functional, perfusable 3D microvascular networks on a chip. *Lab Chip.* 13:1489–1500.
- Kmiec, Z. 2001. Cooperation of liver cells in health and disease. *Adv. Anat. Embryol. Cell Biol.* 161:1–151.
- Ko, I.K., L. Peng, A. Peloso, C.J. Smith, A. Dhal, D.B. Deegan, C. Zimmerman, C. Clouse, W. Zhao, T.D. Shupe, S. Soker, J.J. Yoo, and A. Atala. 2015. Bioengineered transplantable porcine livers with re-endothelialized vasculature. *Biomaterials.* 40:72–79.
- Koike, H., K. Iwasawa, R. Ouchi, M. Maezawa, K. Giesbrecht, N. Saiki, A. Ferguson, M. Kimura, W.L. Thompson, J.M. Wells, A.M. Zorn, and T. Takebe. 2019. Modelling

## References

- human hepato-biliary-pancreatic organogenesis from the foregut–midgut boundary. *Nature*. 574:112–116.
- Kojima, H., K. Yasuchika, K. Fukumitsu, T. Ishii, S. Ogiso, Y. Miyauchi, R. Yamaoka, T. Kawai, H. Katayama, E.Y. Yoshitoshi-Uebayashi, S. Kita, K. Yasuda, N. Sasaki, J. Komori, and S. Uemoto. 2018. Establishment of practical recellularized liver graft for blood perfusion using primary rat hepatocytes and liver sinusoidal endothelial cells. *Am. J. Transplant.* 1–9.
- Korshunov, V.A., S.M. Schwartz, and B.C. Berk. 2007. Vascular remodeling: Hemodynamic and biochemical mechanisms underlying Glagov’s phenomenon. *Arterioscler. Thromb. Vasc. Biol.* 27:1722–1728.
- Koui, Y., T. Kido, T. Ito, H. Oyama, S.W. Chen, Y. Katou, K. Shirahige, and A. Miyajima. 2017. An In Vitro Human Liver Model by iPSC-Derived Parenchymal and Non-parenchymal Cells. *Stem Cell Reports.* 9:490–498.
- Langer, R., and J.P. Vacanti. 1993. Tissue engineering. *Science*. 260:920–926.
- Lee, E.J., G. Vunjak-Novakovic, Y. Wang, and L.E. Niklason. 2009. A biocompatible endothelial cell delivery system for in vitro tissue engineering. *Cell Transplant.* 18:731–743.
- Lehr, E.J., G.R. Rayat, B. Chiu, T. Churchill, L.E. McGann, J.Y. Coe, and D.B. Ross. 2011. Decellularization reduces immunogenicity of sheep pulmonary artery vascular patches. *J. Thorac. Cardiovasc. Surg.* 141:1056–1062.
- Lenard, A., E. Ellertsdottir, L. Herwig, A. Krudewig, L. Sauter, H.G. Belting, and M. Affolter. 2013. In vivo analysis reveals a highly stereotypic morphogenetic pathway of vascular anastomosis. *Dev. Cell.* 25:492–506.
- Lieber, C.S. 2000. Alcohol: Its metabolism and interaction with nutrients. *Annu. Rev. Nutr.* 20:395–430.
- Lin, S.-Z., R.-H. Fu, Y.-C. Wang, S.-P. Liu, T.-R. Shih, H.-L. Lin, Y.-M. Chen, J.-H. Sung, C.-H. Lu, J.-R. Wei, Z.-W. Wang, S.-J. Huang, C.-H. Tsai, and W.-C. Shyu. 2014. Decellularization and Recellularization Technologies in Tissue Engineering. *Cell Transplant.* 23:621–630.
- Liu, L., B.D. Ratner, E.H. Sage, and S. Jiang. 2007. Endothelial cell migration on surface-density gradients of fibronectin, VEGF, or both proteins. *Langmuir.* 23:11168–11173.
- Mabuchi, Y., S. Morikawa, S. Harada, K. Niibe, S. Suzuki, F. Renault-Mihara, D.D. Houlihan, C. Akazawa, H. Okano, and Y. Matsuzaki. 2013. LNGFR+THY-1+VCAM-1hi+ cells reveal functionally distinct subpopulations in mesenchymal stem cells. *Stem Cell Reports.* 1:152–165.
- Mannino, R.G., D.R. Myers, B. Ahn, Y. Wang, Margo Rollins, H. Gole, A.S. Lin, R.E. Guldborg, D.P. Giddens, L.H. Timmins, and W.A. Lam. 2015. Do-it-yourself in vitro vasculature that recapitulates in vivo geometries for investigating endothelial-blood cell interactions. *Sci. Rep.* 5:1–12.
- Martinez-Hernandez, A., and P.S. Amenda. 1995. The extracellular matrix in hepatic

## References

- regeneration. *FASEB J.* 9:1401–1410.
- Maslak, E., A. Gregorius, and S. Chlopicki. 2015. Liver sinusoidal endothelial cells (LSECs) function and NAFLD; NO-based therapy targeted to the liver. *Pharmacol. Reports.* 67:689–694.
- McFadden, T.M., G.P. Duffy, A.B. Allen, H.Y. Stevens, S.M. Schwarzmaier, N. Plesnila, J.M. Murphy, F.P. Barry, R.E. Guldborg, and F.J. O'Brien. 2013. The delayed addition of human mesenchymal stem cells to pre-formed endothelial cell networks results in functional vascularization of a collagen-glycosaminoglycan scaffold in vivo. *Acta Biomater.* 9:9303–9316.
- van der Meer, A.D., A.A. Poot, J. Feijen, and I. Vermes. 2010. Analyzing shear stress-induced alignment of actin filaments in endothelial cells with a microfluidic assay. *Biomicrofluidics.* 4:1–5.
- Meng, F., F. Almohanna, A. Altuhami, A.M. Assiri, and D. Broering. 2019. Vasculature reconstruction of decellularized liver scaffolds via gelatin-based re-endothelialization. *J. Biomed. Mater. Res. Part A.* 107:392–402.
- Michalopoulos, G.K., and M.C. DeFrances. 1997. Liver Regeneration. *Science.* 276:60–66.
- Mina, S.G., W. Wang, Q. Cao, P. Huang, B.T. Murray, and G.J. Mahler. 2016. Shear stress magnitude and transforming growth factor-beta 1 regulate endothelial to mesenchymal transformation in a three-dimensional culture microfluidic device. *RSC Adv.* 6:85457–85467.
- Mironov, V., V. Kasyanov, and R.R. Markwald. 2011. Organ printing: From bioprinter to organ biofabrication line. *Curr. Opin. Biotechnol.* 22:667–673.
- Moran, E.C., P.M. Baptista, D.W. Evans, S. Soker, and J.L. Sparks. 2012. Evaluation of parenchymal fluid pressure in native and decellularized liver tissue. *Biomed. Sci. Instrum.* 48:303–309.
- Morita, M., W. Qun, H. Watanabe, Y. Doi, M. Mori, and K. Enomoto. 1998. Analysis of the sinusoidal endothelial cell organization during the developmental stage of the fetal rat liver using a sinusoidal endothelial cell specific antibody, SE-1. *Cell Struct. Funct.* 23:341–348.
- Murphy, S.L., J. Xu, K.D. Kochanek, S.C. Curtin, and E. Arias. 2015. Deaths: Final Data for 2015. *Natl. Vital Stat. Reports.* 66:1–75.
- Nassiri, S.M., and R. Rahbarghazi. 2014. Interactions of Mesenchymal Stem Cells with Endothelial Cells. *Stem Cells Dev.* 23:319–332.
- Nicosia, R.F., E. Bonanno, and M. Smith. 1993. Fibronectin promotes the elongation of microvessels during angiogenesis in vitro. *J. Cell. Physiol.* 154:654–661.
- Nirmalanandhan, V.S., M.S. Levy, A.J. Huth, and D.L. Butler. 2006. Effects of Cell Seeding Density and Collagen Concentration on Contraction Kinetics of Mesenchymal Stem Cell–Seeded Collagen Constructs. *Tissue Eng.* 12:1865–1872.
- Nishii, K., G. Reese, E.C. Moran, and J.L. Sparks. 2016. Multiscale computational model

## References

- of fluid flow and matrix deformation in decellularized liver. *J. Mech. Behav. Biomed. Mater.* 57:201–214.
- Noor, N., A. Shapira, R. Edri, I. Gal, L. Wertheim, and T. Dvir. 2019. 3D Printing of Personalized Thick and Perfusable Cardiac Patches and Hearts. *Adv. Sci.* 6:1970066 (10 pages).
- Ogiso, S., K. Yasuchika, K. Fukumitsu, T. Ishii, H. Kojima, Y. Miyauchi, R. Yamaoka, J. Komori, H. Katayama, T. Kawai, E.Y. Yoshitoshi, S. Kita, K. Yasuda, and S. Uemoto. 2016. Efficient recellularisation of decellularised whole-liver grafts using biliary tree and foetal hepatocytes. *Sci. Rep.* 6:1–10.
- Palakkan, A.A., D.C. Hay, A.K. Pr, K. Tv, and J.A. Ross. 2013. Liver tissue engineering and cell sources: issues and challenges. *Liver Int.* 33:666–676.
- dela Paz, N.G., T.E. Walshe, L.L. Leach, M. Saint-Geniez, and P.A. D 'amore. 2012. Role of shear-stress-induced VEGF expression in endothelial cell survival. *J. Cell Sci.* 125:831–843.
- Pereira, F.D.A.S., V. Parfenov, Y.D. Khesuani, A. Ovsianikov, and V. Mironov. 2018. Commercial 3D Bioprinters. In *3D Printing and Biofabrication*. A. Ovsianikov, J. Yoo, and V. Mironov, editors. 535–549.
- Poisson, J., S. Lemoine, C. Boulanger, F. Durand, R. Moreau, D. Valla, and P.-E. Rautou. 2017. Liver sinusoidal endothelial cells: Physiology and role in liver diseases. *J. Hepatol.* 66:212–227.
- Pomfret, E.A., J.J. Pomposelli, F.D. Gordon, N. Erbay, L.L. Price, W.D. Lewis, and R.L. Jenkins. 2003. Liver regeneration and surgical outcome in donors of right-lobe liver grafts. *Transplantation.* 76:5–10.
- Prasertsung, I., S. Kanokpanont, T. Bunaprasert, V. Thanakit, and S. Damrongsakkul. 2007. Development of acellular dermis from porcine skin using periodic pressurized technique. *J. Biomed. Mater. Res. - Part B Appl. Biomater.* 85:210–219.
- Price, G.M., K.H.K. Wong, J.G. Truslow, A.D. Leung, C. Acharya, and J. Tien. 2010. Effect of mechanical factors on the function of engineered human blood microvessels in microfluidic collagen gels. *Biomaterials.* 31:6182–6189.
- Qiu, Y., A.C. Brown, D.R. Myers, Y. Sakurai, R.G. Mannino, R. Tran, B. Ahn, E.T. Hardy, M.F. Kee, S. Kumar, G. Bao, T.H. Barker, and W.A. Lam. 2014. Platelet mechanosensing of substrate stiffness during clot formation mediates adhesion, spreading, and activation. *Proc. Natl. Acad. Sci. U. S. A.* 111:14430–14435.
- Quint, C., Y. Kondo, R.J. Manson, J.H. Lawson, A. Dardik, and L.E. Niklason. 2011. Decellularized tissue-engineered blood vessel as an arterial conduit. *Proc. Natl. Acad. Sci.* 108:9214–9219.
- Rennier, K., and J.Y. Ji. 2012. Shear stress regulates expression of death-associated protein kinase in suppressing TNF $\alpha$ -induced endothelial apoptosis. *J. Cell. Physiol.* 227:2398–2411.
- Rezakhaniha, R., A. Agianniotis, J.T.C. Schrauwen, A. Griffa, D. Sage, C.V.C. Bouten, F.N. Van De Vosse, · M Unser, · N Stergiopulos, N. Stergiopulos, and M. Unser.

## References

2012. Experimental investigation of collagen waviness and orientation in the arterial adventitia using confocal laser scanning microscopy. *Biomech Model Mechanobiol.* 11:461–473.
- Ribatti, D., B. Nico, and E. Crivellato. 2011. The role of pericytes in angiogenesis. *Int. J. Dev. Biol.* 55:261–268.
- Rodrigues, S.F., and D.N. Granger. 2015. Blood cells and endothelial barrier function. *Tissue Barriers.* 3:1–2.
- Rouwkema, J., and A. Khademhosseini. 2016. Vascularization and Angiogenesis in Tissue Engineering: Beyond Creating Static Networks. *Trends Biotechnol.* 34:733–745.
- Ruggeri, Z.M., and G.L. Mendolicchio. 2007. Adhesion mechanisms in platelet function. *Circ. Res.* 100:1673–1685.
- Sakai, Y., K. Yamanouchi, K. Ohashi, M. Koike, R. Utoh, H. Hasegawa, I. Muraoka, T. Suematsu, A. Soyama, M. Hidaka, M. Takatsuki, T. Kuroki, and S. Eguchi. 2015. Vascularized subcutaneous human liver tissue from engineered hepatocyte/fibroblast sheets in mice. *Biomaterials.* 65:66–75.
- Sauer, I.M., M. Goetz, I. Steffen, G. Walter, D.C. Kehr, R. Schwartlander, Y.J. Hwang, A. Pascher, J.C. Gerlach, and P. Neuhaus. 2004. In Vitro Comparison of the Molecular Adsorbent Recirculation System (MARS) and Single-pass Albumin Dialysis (SPAD). *Hepatology.* 39:1408–1414.
- Sekine, H., T. Shimizu, K. Sakaguchi, I. Dobashi, M. Wada, M. Yamato, E. Kobayashi, M. Umezu, and T. Okano. 2013. In vitro fabrication of functional three-dimensional tissues with perfusable blood vessels. *Nat. Commun.* 4:1310–1399.
- Shamloo, A., H. Xu, and S. Heilshorn. 2012. Mechanisms of vascular endothelial growth factor-induced pathfinding by endothelial sprouts in biomaterials. *Tissue Eng. - Part A.* 18:320–330.
- Shimoda, H., H. Yagi, H. Higashi, K. Tajima, K. Kuroda, Y. Abe, M. Kitago, M. Shinoda, and Y. Kitagawa. 2019. Decellularized liver scaffolds promote liver regeneration after partial hepatectomy. *Sci. Rep.* 9:1–11.
- Shin, Y., S. Han, J.S. Jeon, K. Yamamoto, I.K. Zervantonakis, R. Sudo, R.D. Kamm, and S. Chung. 2012. Microfluidic assay for simultaneous culture of multiple cell types on surfaces or within hydrogels. *Nat. Protoc.* 7:1247–1259.
- Shirakigawa, N., H. Ijima, and T. Takei. 2012. Decellularized liver as a practical scaffold with a vascular network template for liver tissue engineering. *J. Biosci. Bioeng.* 114:546–551.
- Shirakigawa, N., T. Takei, and H. Ijima. 2013. Base structure consisting of an endothelialized vascular-tree network and hepatocytes for whole liver engineering. *J. Biosci. Bioeng.* 116:740–745.
- Sigovan, M., V. Rayz, W. Gasper, H.F. Alley, C.D. Owens, and D. Saloner. 2013. Vascular Remodeling in Autogenous Arterio-Venous Fistulas by MRI and CFD. *Ann. Biomed. Eng.* 41:657–668.

## References

- Sobrino, A., D.T.T. Phan, R. Datta, X. Wang, S.J. Hachey, M. Romero-López, E. Gratton, A.P. Lee, S.C. George, and C.C.W. Hughes. 2016. 3D microtumors in vitro supported by perfused vascular networks. *Sci. Rep.* 6:1–11.
- Song, J.W., D. Bazou, L.L. Munn, and E.L. Steele. 2012. Anastomosis of endothelial sprouts forms new vessels in a tissue analogue of angiogenesis. *Integr. Biol.* 4:857–862.
- Song, J.W., and L.L. Munn. 2011. Fluid forces control endothelial sprouting. *Proc. Natl. Acad. Sci. U. S. A.* 108:15342–15347.
- Soto-Gutierrez, A., L. Zhang, C. Medberry, K. Fukumitsu, D. Faulk, H. Jiang, J. Reing, R. Gramignoli, J. Komori, M. Ross, M. Nagaya, E. Lagasse, D. Stolz, S.C. Strom, I.J. Fox, and S.F. Badylak. 2011. A whole-organ regenerative medicine approach for liver replacement. *Tissue Eng. Part C.* 17:677–86.
- Stevens, K.R., M.A. Scull, V. Ramanan, C.L. Fortin, R.R. Chaturvedi, K.A. Knouse, J.W. Xiao, C. Fung, T. Mirabella, A.X. Chen, M.G. Mccue, M.T. Yang, H.E. Fleming, K. Chung, Y.P. De Jong, C.S. Chen, C.M. Rice, and S.N. Bhatia. 2017. In situ expansion of engineered human liver tissue in a mouse model of chronic liver disease. *Sci. Transl. Med.* 9:1–10.
- Strom, S., and R. Fisher. 2003. Hepatocyte transplantation: New possibilities for therapy. *Gastroenterology.* 124:568–571.
- Sudo, R. 2014. Multiscale tissue engineering for liver reconstruction. *Organogenesis.* 10:1–9.
- Sudo, R., S. Chung, I.K. Zervantonakis, V. Vickerman, Y. Toshimitsu, L.G. Griffith, and R.D. Kamm. 2009. Transport-mediated angiogenesis in 3D epithelial coculture. *FASEB J.* 23:2155–2164.
- Takayama, K., M. Inamura, K. Kawabata, M. Sugawara, K. Kikuchi, M. Higuchi, Y. Nagamoto, H. Watanabe, K. Tashiro, F. Sakurai, T. Hayakawa, M.K. Furue, and H. Mizuguchi. 2012. Generation of metabolically functioning hepatocytes from human pluripotent stem cells by FOXA2 and HNF1 $\alpha$  transduction. *J. Hepatol.* 57:628–636.
- Takayama, K., Y. Morisaki, S. Kuno, Y. Nagamoto, K. Harada, N. Furukawa, M. Ohtaka, K. Nishimura, K. Imagawa, F. Sakurai, M. Tachibana, R. Sumazaki, E. Noguchi, M. Nakanishi, K. Hirata, K. Kawabata, and H. Mizuguchi. 2014. Prediction of interindividual differences in hepatic functions and drug sensitivity by using human iPSC-derived hepatocytes. *Proc. Natl. Acad. Sci. U. S. A.* 111:16772–16777.
- Takebe, T., N. Koike, K. Sekine, R. Fujiwara, T. Amiya, Y.-W. Zheng, and H. Taniguchi. 2014. Engineering of human hepatic tissue with functional vascular networks. *Organogenesis.* 10:260–267.
- Takebe, T., K. Sekine, M. Enomura, H. Koike, M. Kimura, T. Ogaeri, R.-R. Zhang, Y. Ueno, Y.-W. Zheng, N. Koike, S. Aoyama, Y. Adachi, and H. Taniguchi. 2013. Vascularized and functional human liver from an iPSC-derived organ bud transplant. *Nature.* 499:481–4.
- Takebe, T., K. Sekine, M. Kimura, E. Yoshizawa, S. Ayano, M. Koido, S. Funayama, N.

## References

- Nakanishi, T. Hisai, T. Kobayashi, T. Kasai, R. Kitada, A. Mori, H. Ayabe, Y. Ejiri, N. Amimoto, Y. Yamazaki, S. Ogawa, M. Ishikawa, Y. Kiyota, Y. Sato, K. Nozawa, S. Okamoto, Y. Ueno, and H. Taniguchi. 2017. Massive and Reproducible Production of Liver Buds Entirely from Human Pluripotent Stem Cells. *Cell Rep.* 21:2661–2670.
- Tatsumi, K., and T. Okano. 2017. Hepatocyte Transplantation: Cell Sheet Technology for Liver Cell Transplantation. *Curr. Transplant. Reports.* 4:184–192.
- Ueda, A., M. Koga, M. Ikeda, S. Kudo, and K. Tanishita. 2004. Effect of shear stress on microvessel network formation of endothelial cells with in vitro three-dimensional model. *Am. J. Physiol. Circ. Physiol.* 287:994–1002.
- Ueda, A., R. Sudo, M. Ikeda, S. Kudo, and K. Tanishita. 2006. Initial bFGF Distribution Affects the Depth of Three-dimensional Microvessel Networks in vitro. *J. Biomech. Sci. Eng.* 1:136–146.
- Unsworth, D.J., D.L. Scott, T.J. Almond, H.K. Beard, E.J. Holborow, and K.W. Walton. 1982. Studies on reticulin. I: Serological and immunohistological investigations of the occurrence of collagen type III, fibronectin and the non-collagenous glycoprotein of Pras and Glynn in reticulin. *Br J Exp Pathol.* 63:154–166.
- Urbich, C., E. Dermbach, A. Reissner, M. Vasa, A.M. Zeiher, and S. Dimmeler. 2002. Shear stress-induced endothelial cell migration involves integrin signaling via the fibronectin receptor subunits  $\alpha 5$  and  $\beta 1$ . *Arterioscler. Thromb. Vasc. Biol.* 22:69–75.
- Uwamori, H., Y. Ono, T. Yamashita, K. Arai, and R. Sudo. 2019. Comparison of organ-specific endothelial cells in terms of microvascular formation and endothelial barrier functions. *Microvasc. Res.* 122:60–70.
- Uygun, B.E., A. Soto-Gutierrez, H. Yagi, M.-L. Izamis, M.A. Guzzardi, C. Shulman, J. Milwid, N. Kobayashi, A. Tilles, F. Berthiaume, M. Hertl, Y. Nahmias, M.L. Yarmush, and K. Uygun. 2010. Organ reengineering through development of a transplantable recellularized liver graft using decellularized liver matrix. *Nat. Med.* 16:814–20.
- Vernon, R.B., and E.H. Sage. 1995. Between molecules and morphology. Extracellular matrix and creation of vascular form. *Am. J. Pathol.* 147:873–83.
- Wang, X., D.T.T. Phan, A. Sobrino, S.C. George, C.C.W. Hughes, and A.P. Lee. 2016. Engineering anastomosis between living capillary networks and endothelial cell-lined microfluidic channels. *Lab Chip.* 16:282–290.
- Wang, X., Q. Sun, and J. Pei. 2018. Microfluidic-based 3D engineered microvascular networks and their applications in vascularized microtumor models. *Micromachines.* 9:1–26.
- Watanabe, M., and R. Sudo. 2019. Establishment of an in vitro vascular anastomosis model in a microfluidic device. *J. Biomech. Sci. Eng.* 14:1–17.
- Watanabe, M., K. Yano, K. Okawa, T. Yamashita, K. Tajima, K. Sawada, H. Yagi, Y. Kitagawa, K. Tanishita, and R. Sudo. 2019. Construction of sinusoid-scale microvessels in perfusion culture of a decellularized liver. *Acta Biomater.* 95:307–318.

## References

- Weidenhamer, N.K., D.L. Moore, F.L. Lobo, N.T. Klair, and R.T. Tranquillo. 2015. Influence of culture conditions and extracellular matrix alignment on human mesenchymal stem cells invasion into decellularized engineered tissues. *J. Tissue Eng. Regen. Med.* 9:605–618.
- Woods, T., and P.F. Gratzler. 2005. Effectiveness of three extraction techniques in the development of a decellularized bone-anterior cruciate ligament-bone graft. *Biomaterials.* 26:7339–7349.
- Wragg, J.W., S. Durant, H.M. Mcgettrick, K.M. Sample, S. Egginton, and R. Bicknell. 2014. Shear stress regulated gene expression and angiogenesis in vascular endothelium. *Microcirculation.* 21:290–300.
- Wu, Y., M.A. Al-Ameen, and G. Ghosh. 2014. Integrated Effects of Matrix Mechanics and Vascular Endothelial Growth Factor (VEGF) on Capillary Sprouting. *Ann. Biomed. Eng.* 42:1024–1036.
- Xu, J., S.L. Murphy, K.D. Kochanek, B. Bastian, and E. Arias. 2018. Deaths: Final Data for 2016. *Natl. Vital Stat. Reports.* 67:1–76.
- Yagi, H., K. Fukumitsu, K. Fukuda, M. Kitago, M. Shinoda, H. Obara, O. Itano, S. Kawachi, M. Tanabe, G.M. Coudriet, J.D. Piganelli, T.W. Gilbert, A. Soto-Gutierrez, and Y. Kitagawa. 2013. Human-scale whole-organ bioengineering for liver transplantation: A regenerative medicine approach. *Cell Transplant.* 22:231–242.
- Yamamoto, K., T. Takahashi, T. Asahara, N. Ohura, T. Sokabe, A. Kamiya, and J. Ando. 2003. Proliferation, differentiation, and tube formation by endothelial progenitor cells in response to shear stress. *J Appl Physiol.* 95:2081–2088.
- Yamamoto, K., K. Tanimura, Y. Mabuchi, Y. Matsuzaki, S. Chung, R.D. Kamm, M. Ikeda, K. Tanishita, and R. Sudo. 2013. The stabilization effect of mesenchymal stem cells on the formation of microvascular networks in a microfluidic device. *J. Biomech. Sci. Eng.* 8:114–128.
- Yamamoto, K., K. Tanimura, M. Watanabe, H. Sano, H. Uwamori, Y. Mabuchi, Y. Matsuzaki, S. Chung, R.D. Kamm, K. Tanishita, and R. Sudo. 2019. Construction of continuous capillary networks stabilized by pericyte-like perivascular cells. *Tissue Eng. Part A.* 25:499–510.
- Yamamoto, M., and E. Tahara. 1984. Distribution of Collagen Types I, III, and V in Fibrotic and Neoplastic Human Liver. *Acta Pathol. Jpn.* 34:77–86.
- Yamamura, N., R. Sudo, M. Ikeda, and K. Tanishita. 2007. Effects of the mechanical properties of collagen gel on the in vitro formation of microvessel networks by endothelial cells. *Tissue Eng.* 13:1443–1453.
- Yeon, J.H., H.R. Ryu, M. Chung, Q.P. Hu, and N.L. Jeon. 2012. In vitro formation and characterization of a perfusable three-dimensional tubular capillary network in microfluidic devices. *Lab Chip.* 12:2815–2822.
- Zandstra, P.W., E. Conneally, A.L. Petzer, J.M. Piret, and C.J. Eaves. 1997. Cytokine manipulation of primitive human hematopoietic cell self-renewal. *Proc. Natl. Acad. Sci. U. S. A.* 94:4698–703.

## References

Zhou, Q., L. Li, and J. Li. 2015. Stem cells with decellularized liver scaffolds in liver regeneration and their potential clinical applications. *Liver Int.* 35:687–694.

## Achievements

### Publications

#### Main publications

1. Watanabe M., Yano K., Okawa K., Yamashita T., Tajima K., Sawada K., Yagi H., Kitagawa Y., Tanishita K., and Sudo R. “Construction of sinusoid-scale microvessels in perfusion culture of a decellularized liver” *Acta Biomaterialia*, 95: 307–318, 2019.
2. Watanabe M., and Sudo R. “Establishment of an *in vitro* vascular anastomosis model in a microfluidic device” *Journal of Biomechanical Science and Engineering*, 14(3): 1–17, 2019.

#### Other publications

3. Yamamoto K., Tanimura K., Watanabe M., Sano H., Uwamori H., Mabuchi Y., Matsuzaki Y., Chung S., Kamm R.D., Tanishita K., and Sudo R. “Construction of continuous capillary networks stabilized by pericyte-like perivascular cells” *Tissue Engineering Part A*, 25(5–6): 499–510, 2019.
4. Abe Y., Watanabe M., Chung S., Kamm R.D., Tanishita K., and Sudo R. “Balance of interstitial flow magnitude and vascular endothelial growth factor concentration modulates three-dimensional microvascular network formation” *APL Bioengineering*, 3(3): 1–12, 2019.

### International conferences

#### Oral presentation

1. Watanabe M., Murai R., and Sudo R., “Investigation of microvessel morphological change and corresponding vascular wall shear stress distribution during *in vitro* vascular remodeling in a microfluidic device” 8<sup>th</sup> World Congress of Biomechanics, Dublin, Ireland, 2018.

## Achievements

### Poster presentation

2. Watanabe M., Uwamori H., and Sudo R., “Construction of capillary anastomosis in a microfluidic device” 37<sup>th</sup> Annual International Conference of the IEEE Engineering in Medicine and Biology Society Biomedical Engineering, Milan, Italy, 2015.
3. Watanabe M., Murai R., and Sudo R., “Microfluidic-based application of an *in vitro* microvessel model: investigation of vascular morphology and corresponding wall shear stress during vascular remodeling” Lab-on-a-Chip and Microfluidics World Congress 2018, San Diego, USA, 2018.
4. Watanabe M., Yano K., Okawa K., and Sudo R., “Construction of *in vitro* hierarchical vascular networks using tissue-derived microchannels” EMBS Micro and Nanotechnology in Medicine Conference 2018, Hawaii, USA, 2018.
5. Watanabe M., Yano K., Okawa K., and Sudo R., “Regeneration of organ-scale vascular networks in a decellularized liver by flow-induced mechanical stress” International Symposium on SSS Laser Processing, Yokohama, Japan, 2019.
6. Watanabe M., Yano K., Okawa K., Yamashita T., and Sudo R., “Flow-induced mechanical force promotes microvascular formation in a decellularized liver” 3<sup>rd</sup> International Symposium on Nanoarchitectonics for Mechanobiology, Tsukuba, Japan, 2019.
7. Watanabe M., and Sudo R., “Engineering of *in vitro* vascular anastomosis under vascular endothelial growth factor (VEGF) gradients in a microfluidic device” TERMIS European Chapter Meeting 2019, Rhodes, Greece, 2019.

## Achievements

### Domestic conferences

#### 口頭発表

1. 渡邊應文, 上森寛元, 須藤亮, “マイクロ流体デバイスを利用した毛細血管網吻合条件の検討” 日本機械学会 2015年度年次大会, 札幌, 2015.
2. 渡邊應文, 矢野公規, 大川航輝, 須藤亮, “血管内皮細胞と間葉系幹細胞の共培養による脱細胞化肝臓内の血管ネットワークの再構築” 日本機械学会 バイオエンジニアリング講演会, 名古屋, 2017.
3. 渡邊應文, 矢野公規, 大川航輝, 須藤亮, “脱細胞化肝臓骨格の還流培養における類洞スケールの毛細血管構造の構築” 日本機械学会 バイオフロンティア講演会, 千葉, 2018.

#### ポスター発表

4. 渡邊應文, 矢野公規, 大川航輝, 八木洋, 北川雄光, 須藤亮, “脱細胞化肝臓骨格の還流培養による類洞様構造の構築” 肝細胞研究会, 横浜, 2019.

### Awards

1. Certificate of Merit for Outstanding Young Researcher Presentation at 8<sup>th</sup> World Congress of Biomechanics 2018 (Dublin, Ireland).

## Acknowledgements

My research activities for this thesis were carried out at Keio University under the guidance of Prof. Ryo Sudo. Firstly, I would like to express my sincere gratitude to him for the continuous support of my Ph.D study and related research, for his patience, motivation, and immense knowledge. His guidance helped me in all the time of research and writing of this thesis. I could not have imagined having a better advisor and mentor for my Ph.D study.

Besides my advisor, I would like to thank Prof. Kazuo Tanishita for helpful discussions and suggestions and supporting me in many aspects including fluid analysis, which dramatically improved this thesis by CFD analysis. I would like to thank Prof. Tadahiro Yamashita for his insightful comments and encouragement, but also for the hard questions which incited me to widen my research from various perspectives.

I would also like to thank Prof. Yuko Kitagawa, Prof. Hiroshi Yagi, Prof. Kazuki Tajima, and Prof. Kohei Kuroda, who provided me an opportunity to conduct organ-scale tissue engineering. I would like to thank Dr. Takeshi Imamura, Dr. Ryosuke Kawakami, and Dr. Kazuaki Sawada for supporting deep-tissue imaging with advanced multiphoton confocal microscopes. Without their precious support, it would not be possible to accomplish this research.

I would like to thank my thesis committee members, Prof. Hiroaki Onoe, Prof. Yoshihiro Taguchi, and Prof. Kosuke Tsukada for their very valuable and helpful discussions which have significantly contributed to the improvement of this research.

I thank my fellow lab members in Keio University. I am especially grateful to Dr. Hiroyuki Uwamori for the stimulating discussions and interesting comments, Ryosuke Murai for helpful discussions and suggestions, Koki Yano, Koki Okawa, and Masayuki Shinohara for valuable discussions and supporting a lot of experiments.

Finally, I would like to thank my family throughout writing this thesis and my life.

February 2020

Masafumi Watanabe